INVESTIGATION OF HIGH FREQUENCY INSTABILITIES IN THE PLUME OF THE VX-200 MAGNETIC NOZZLE

A Dissertation Presented to

the Faculty of the Department of Physics

University of Houston

In Partial Fulfillment

of the Requirements for the Degree

Doctor of Philosophy

By

Matthew Giambusso

May 2018

INVESTIGATION OF HIGH FREQUENCY INSTABILITIES IN THE PLUME OF THE VX-200 MAGNETIC NOZZLE

Matthew Giambusso

APPROVED:

Dr. Edgar A. Bering III, Chairman

Dr. Gemunu H. Gunaratne

Dr. Lawrence S. Pinsky

Dr. George F. Reiter

Dr. Demetre J. Economou
Cullen College of Engineering

Dr. Mark D. Carter
Ad Astra Rocket Company

Dean, College of Natural Sciences and Mathematics

ACKNOWLEDGEMENTS

In May of 2009, I was trying to figure out how to transition from being a Navy submariner to a plasma rocket scientist. I am still working on this transition, but I wish to thank some of the people who have helped me so far. I sincerely thank Dr. Edgar A. Bering III for being my dissertation advisor, and particularly for his words of encouragement nine years ago; they have changed my life. I thank my dissertation committee, for their guidance and patience during my learning process. My gratitude goes to the physics and math instructors who have taught and challenged me at the University of Houston, particularly Drs. Kevin Bassler, Lowell Wood, George Reiter, Ed Hungerford, David Wagner, and the late Drs. Michael Gorman, Bambi Hu, and Kwong Lau. I also thank my classmates, particularly Mr. Luis Ackermann and Dr. Cameron Williams, who answered many naïve questions of mine and helped me through some difficult coursework.

I owe a great deal to the men and women of Ad Astra Rocket Company, who have employed me for most of my graduate career. I am honored and thrilled to be part of their team. I particularly thank Drs. Franklin Chang-Diaz, Jared Squire, and Mark Carter, and Messrs. Greg McCaskill and Lawrence Dean, for teaching me about VASIMR®, plasma, space propulsion, electronics, manufacturing and countless other subjects. I thank Mrs. Yamaris Lopez-Nieves and Ms. Miranda Chang for their expressions of confidence in the successful conclusion of this dissertation. I also thank the former employees of Ad Astra who have since moved elsewhere, including

Dr. Benjamin Longmier, Mr. Maxwell Ballenger, and particularly Dr. Christopher Olsen, whose Ph.D. thesis was a foundation for my own.

Lastly, I thank my family. To my parents and my sisters, I am grateful for all the ways they have helped grow into the person I am. To my daughters, Rosalie and Liliana, and to my unborn daughter, I am grateful for their inspiration; they make me want to be better in every way. I thank them also for their generous forfeiture of play time for the sake of this research. Being their father is more than I deserve. To my wife Angela, I owe such a debt of love and sacrifice as I don't yet know how to repay. I am working on this as well. I thank her, with all my heart, for steadfastly supporting me in this endeavor, and for being my partner in life.

INVESTIGATION OF HIGH FREQUENCY INSTABILITIES IN THE PLUME OF THE VX-200 MAGNETIC NOZZLE

An Abstract of a Dissertation

Presented to

the Faculty of the Department of Physics

University of Houston

In Partial Fulfillment

of the Requirements for the Degree

Doctor of Philosophy

By

Matthew Giambusso

May 2018

ABSTRACT

During testing of the Variable Specific Impulse Magnetoplasma Rocket (VASIMR®) VX-200 device, high frequency (HF) harmonics of the ion cyclotron heating (ICH) stage were measured in the radial component of the electric field along the upstream edge of the plasma exhaust. The oscillations were low amplitude and electrostatic, existing in a limited region of the plasma plume. The perpendicular electron density gradient in this portion of the plume could allow growth of the lower hybrid drift instability (LHDI) or the modified two-stream instability (MTSI), but the perpendicular DC electric field is generally not strong enough to support these drift waves. It is theorized that the ICH power excites the unstable drift waves; the amplified ICH harmonics are the ones whose frequencies are close to the theoretical frequency of the instability. In a separate but related approach, the stability of the exhaust jet is examined under the assumption of cold, homogenous, and uniformly magnetized plasma. A Clemmow Mullaly Allis (CMA) diagram for singly ionized Argon is drawn and annotated with scans through the plasma plume. Finally, a two-dimensional particle-in-cell model of the exhaust plume is developed, simulating a trans-Alfvénic plasma jet, the ion kinetic Beta transitioning from less than one to greater than one. In future works, beyond the scope of this dissertation, this simulation model will test theories about wave physics and detachment in the exhaust plume.

TABLE OF CONTENTS

I. INTRODUCTION

A magnetic nozzle is the region where magnetized plasma detaches from a diverging magnetic field. The plasma downstream of the nozzle is a ballistic jet. Magnetic nozzles are abundant in the universe, existing in the poles of stellar and planetary magnetospheres. The word 'nozzle' is appropriate for this work because the prevailing usage context is that of electric prolusion (EP) devices for spacecraft. EP systems, in general, heat a propellant to the state of plasma and accelerate it using electrical power. Some EP designs employ a magnetic nozzle, which allows ionized propellant to detach from an axial magnetic field and impart thrust on the spacecraft. Examples of such designs include helicon thrusters, electron cyclotron thrusters, applied-field magnetoplasmadynamic thrusters, and the Variable Specific Impulse Magnetoplasma Rocket (VASIMR®). The VX-200 was a prototype of the VASIMR® design; its exhaust plume will serve as an example of a magnetic nozzle plasma in this dissertation.

This work builds on the recently completed Ph.D. thesis of Christopher Olsen,[1] which included a thorough experimental investigation of the plasma detachment processes in VX- 200 magnetic nozzle. Olsen measured high-frequency (HF) oscillations in the radial electric field of the VX-200 plume. The oscillations were thought to be evidence of an instability that contributes to the diffusion of the electrons across the magnetic field lines. Cross-field diffusion is necessary for the plasma to remain quasineutral as it separates from the applied magnetic field. This

work investigates further the nature of the observed electric field oscillations, attempting to understand their origin.

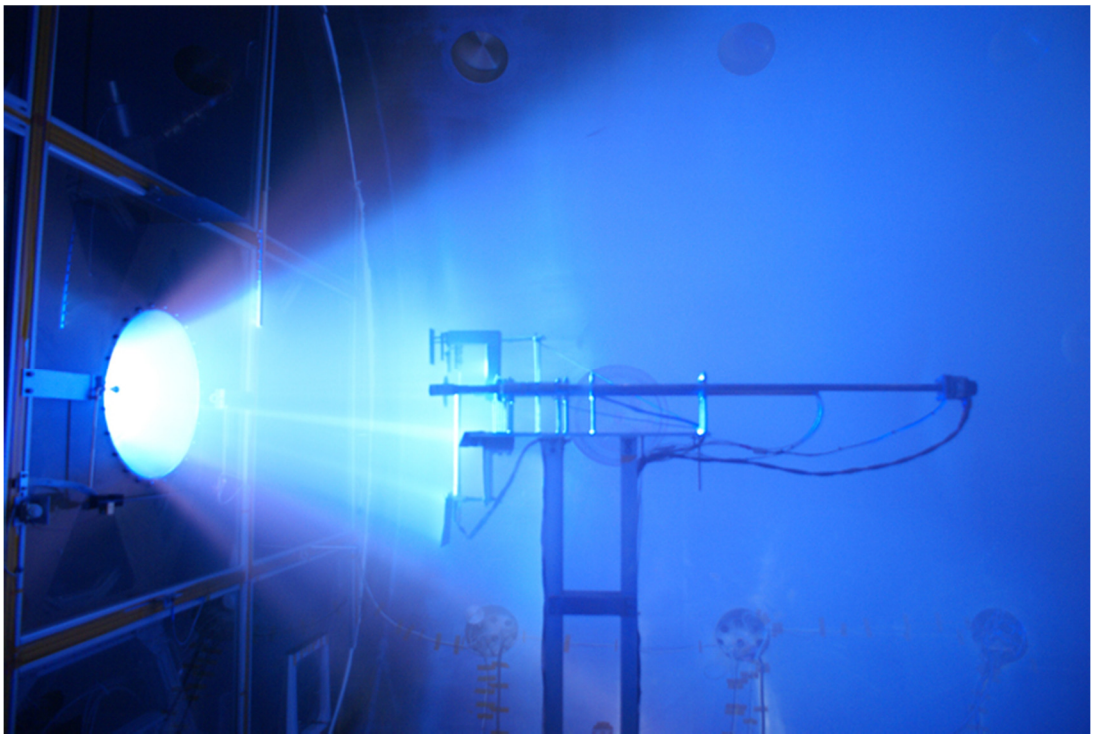

Figure 1 – Photograph of the VX-200 plasma plume and diagnostics translation stage. This photograph was taken through a viewport in the vacuum chamber. The plasma jet and the background magnetic field of the VX-200 experiment are the subject of this dissertation. The prominent shaft oriented along the flow of the plasma is the retarding potential anlayzer (RPA) probe. For scale, the length of the RPA is approximately one meter. This image is provided courtesy of the Ad Astra Rocket Company.

The recent undergraduate thesis of Corey Henderson[2] also serves as a foundation. Henderson began the process of modeling the VX-200 magnetic nozzle exhaust plume using a particle-in-cell (PIC) simulation code. The PIC model of the plume has been further developed here, with the goal of making the simulation more

applicable to a practical magnetic nozzle discharge. The goal of the PIC model development is the study of instabilities in magnetic nozzle plasma.

Figure 2 - Potograph of the interior of the VX-200 vacuum chamber. This image was taken looking upstream, counter to the plasma flow. The chamber is 10 m in length and 4.2 m in diameter. The two-dimensional diagnostics translation stage is visible in the middle ground. The VX-200 device is located behind the plastic wall in the background.

A. Organization of this Dissertation

This section lists the goals for each chapter of this document. The work is split into two main parts: the stability analysis of the VX-200 plasma plume, and the development of the magnetic nozzle PIC simulation.

Chapter II further introduces the VX-200 plasma diagnostics experiment and the prior detachment study, including the measurements of an electric field oscillation in a limited region of the plasma plume. Chapter II also introduces some theory of the lower-hybrid-drift instability (LHDI) and the modified two-stream instability (MTSI), which are suspected of being related to the observed electric field oscillations. Chapter III then analyzes the stability of the experimentally measured parameters of the VX-200 plasma exhaust, aiming to determine if the LHDI or the MTSI were likely to have been observed. Chapter III concludes with the VX-200 plume being treated as a cold plasma; its stability is analyzed by drawing a specialized Clemmow Mullaly Allis (CMA) diagram. The diagram is annotated with experimental data scans at the frequency of the observed instability.

Chapter IV introduces the PIC model of the magnetic nozzle plume and discusses some of the difficulties encountered during its development. Chapter V then discusses the final simulation campaign, which attempted to model a plasma discharge whose ions transition from sub-Alfvénic to super-Alfvénic as they transit the magnetic nozzle. Results of this campaign are presented.

Finally, Chapter 0 summarizes the conclusions of Chapters III and V, which contain most of the original work of this document. Future studies are also suggested.

Appendices contain plotting scripts used to visualize data and input files used by the PIC software. References are listed at the end of the document, in order of appearance.

II. BACKGROUND

This chapter discusses the prior experimental studies of the VX-200 and the theory of the LHDI, both of which motivated the work of this dissertation.

A. VX-200 Experiment

The VX-200 was a laboratory prototype VASIMR® engine, in operation from 2007 to 2012. It was fired more than ten thousand times and accumulated more than one hour of operations, achieving a maximum power level of over 200 kW at a thruster efficiency of 72%.[3] Thruster efficiency is defined as the ratio of the jet power produced by the engine to the input RF electrical power.[4]

$$\eta_T = \frac{P_{Jet}}{P_{RF}}$$

$$P_{jet} = \frac{F^2}{2\dot{m}}$$

F here is the total axial force produced by the thruster and $\dot{m}$ is the mass flow rate of the propellant.

The VASIMR® design combines a helicon plasma source with an ion cyclotron heating (ICH) booster stage. A surrounding superconducting magnet allows plasma power densities in excess of 10 MW/m^2 at the exit and specific impulses greater than 4000 seconds, using Argon propellant. VASIMR® flight systems will initially use solar electric power to operate at 100 kW or more, but the technology is intended to scale to MW class missions. Ad Astra Rocket Company is currently under a NASA

NextSTEP contract to mature the VASIMR® design to technology readiness level (TRL)-5.

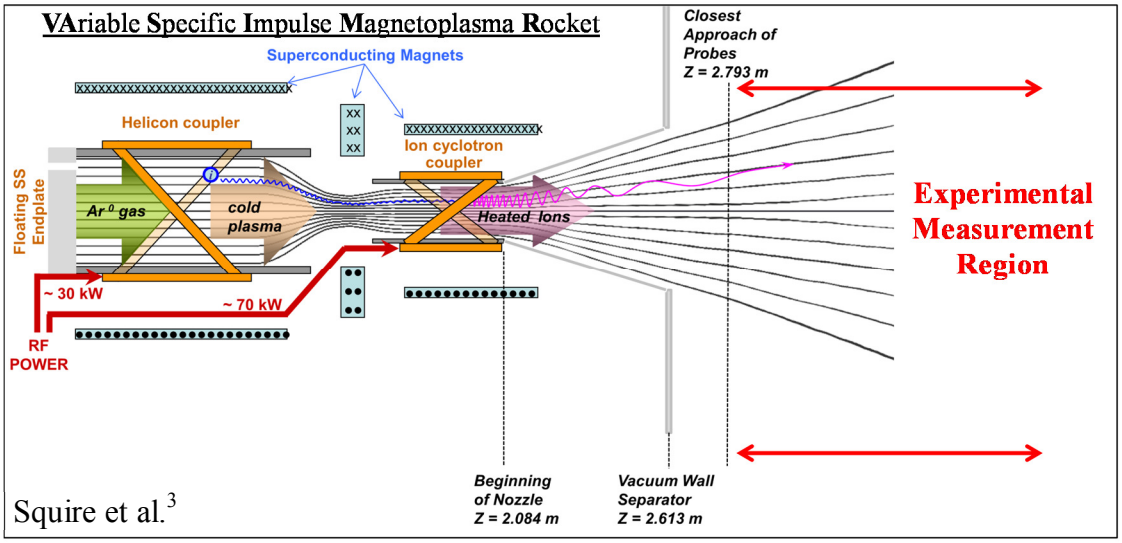

Figure 3 - Concept Diagram of the VASIMR® VX-200 Experiment. This figure was originally published in Squire et al.[3] It shows the major functional components of the rocket core and their effect on the argon propellant. The solid black lines depict the basic shape of the magnetic field. The red arrows depict the region that was accessible to the plasma probes and the two-dimensional translation stage. This work focuses on the plasma in the experimental measurement region.

B. Instabilities Observed During Detachment Study

During an exhaustive experimental study of the VX-200 exhaust plume, Olsen measured oscillations in the radial component of the electric field.[1, 5] The oscillating electric fields were measured using a probe consisting of a pair of electrodes 5mm long and separated by 11.9 mm. The time-varying field was detected in a localized region of the exhaust plume, mostly near the edge of the plasma, and only when the ions were heated by the ICH stage of the VX-200. The spatial extent, amplitude, and

major frequencies of the observations are shown in Figure 4. A sample of the acquired spectrum is shown in Figure 6.

The time-dependent electric field measurements were but one type of various probe measurements made by Olsen et al. during the plume experimental study. Other measurements included those of ion flux, magnetic flux, momentum flux, electron density, and ion velocity. The experimental campaign consisted of more than 1500 plasma firings, or shots; each reaching approximately 100 kW of input power and lasting approximately one second. Each shot was followed by a small translation of the diagnostics stage. In this way, measurements throughout the exhaust plume were gradually accumulated. Details of the experimental process have been published by Olsen.[1, 5]

One objective of the plume study was to answer an important question about the VASIMR® concept: Does the exhaust plasma detach from the magnetic nozzle? The answer to this question has implications for the indirect methods by which the thrust of a VASIMR® engine can be measured, and the general usefulness of propulsion systems designed around magnetic nozzles. As the publications show, several independent measurements indicate that the plasma does indeed detach.[1, 5] The observed radial electric field oscillations are thought to play a role in the detachment process. A main focus of this dissertation is to understand the formation of these waves.

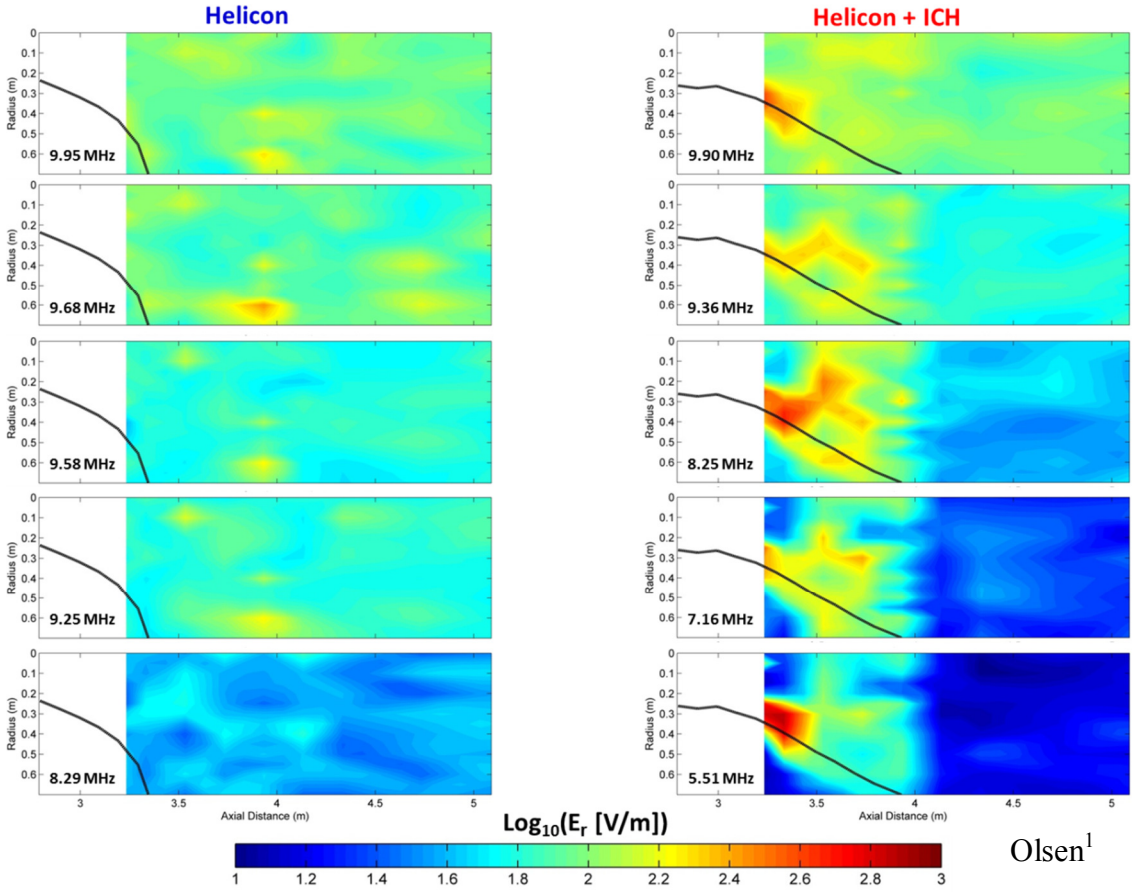

Figure 4 – Oscillating electric field amplitude maps. This figure is excerpted from Olsen.[1] The maps show the magnitude of a time-dependent radial electric field at the frequencies of greatest amplitude during Helicon only operation (left), and both Helicon and ICH operation (right). The black lines show the effective plume edge, which is based on radially integrating 90% of the reference axial ion flux. One objective of this dissertation is to test theories about the nature of this instability. Olsen measured the time-verying fields and analysed the effect they might have on cross-field diffusion of electrons, a phenomenon thought to be important for detachment of the plsma from the magnetic nozzle.

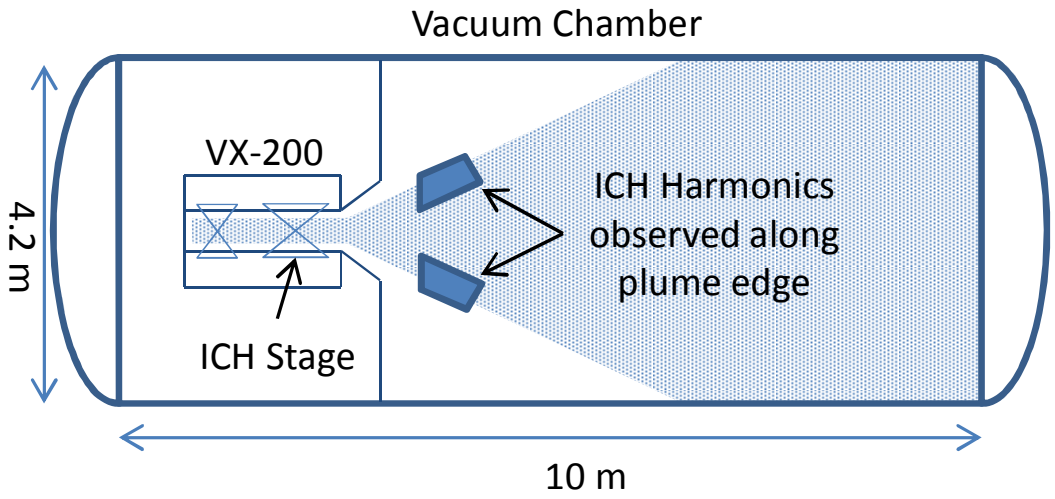

Figure 5 - Geometry of VX-200 experiment. This is a simplified sketch that shows the location of the ion cyclotron heating (ICH) stage and the general extent of the region where ICH harmonics were detected in the exhaust plume. The upstream boundary of the detection region is the furthest upstream point accessible to the radial electric field probe. The unstable region could well extend further upstream than what is shown.

Harmonics of the fundamental frequency of the ICH power are clearly visible in the acquired electric field spectra; Figure 6 contains an example. At frequencies above 5 MHz, the harmonics of the ICH drive frequency are significantly amplified; the amplitudes of these harmonics are greater than that of the lower frequency harmonics by factors up to five. It has been asserted that the measured oscillations could be evidence of the Lower Hybrid Drift Instability (LHDI) or the Modified Two-Stream Instability (MTSI); the oscillations were not previously recognized as being harmonics of the ICH.[1] It is now theorized that the ICH process may directly help to excite the LHDI or the MTSI at harmonic frequencies, and that these harmonics are in-turn amplified by the instability. This conjecture does not diminish the previously published analysis of Olsen et al., which evaluated the effect that the observed electric

field oscillations may have on the detachment of plume electrons from the magnetic nozzle.[5] On the contrary, this work attempts only to investigate how the instability comes about. Towards this end, an investigation of the stability of the VX-200 plasma plume to the LHDI and the MTSI is performed in Chapter III. In preparation, the next section reviews the theoretical background of these waves.

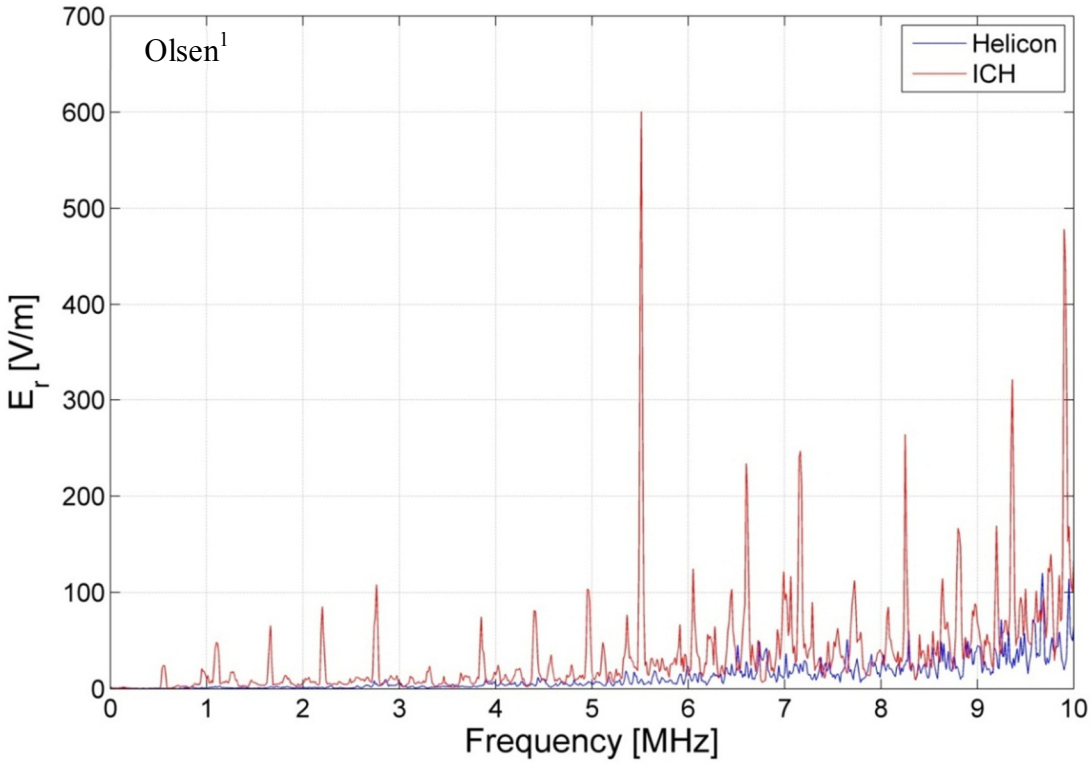

Figure 6 – Sample electric field spectrum. This figure is excerpted from Olsen.[1] This spectrum was observed at z=3.23m, y=0.2m. The ICH drive harmonics are clearly visible as the prominent peaks in red. The blue spectrum was acquired during Helicon-only operation. At higher frequencies, the harmonics of the ICH drive are significantly amplified. This frequency-dependent phenomenon coincides with the frequencies of the LHDI and the MTSI, in certain regions of the VX-200 plume. The stability of the plume to the LHDI and the MTSI is investigated in Chapter III.

C. Theory of the Lower Hybrid Drift Instability

One of the major early works on the theory of the LHDI was published by Krall and Liewer.[6] The instability occurs where there are radial gradients in the electron temperature, $T_e(r)$, the electron density, $n_e(r)$, and the axial magnetic field strength, $B_z(r)$; and where there is a radial electric field that drives an azimuthal electron drift. Krall and Liewer derived conditions for a strong and weak version the LHDI.

The LHDI was associated with electromagnetic plasma thrusters in publications by Choueiri et al. in 1985.[7] Professor Choueiri remarks in his Ph.D. thesis[8] that the 1985 paper "marked the beginning of a lasting association between the LFA (Lorentz Force Accelerator) plasma and the instability of the lower hybrid mode." LFA in this context stands for Lorentz Force Accelerator, which is a type of electric propulsion device. The LHDI has also been studied as a mechanism for cross-field electron diffusion by Hurtig, Brenning and Raadu.[9] This group has suggested the LHDI as being probable in the magnetic nozzle expansion of a VASIMR®.

The remainder of this section is a review of the LHDI and MTSI theory published by Krall and Liewer. When there are strong gradients, the plasma will be unstable to lower hybrid drift waves if the drift speed satisfies the following relation:

$$v_\Delta v_E \geq {c_s}^2$$

Here, v_E is the electric field-drift velocity, v_Δ is the sum of the gradient-drift velocities, and c_s is the ion sound speed. These parameters are defined by Krall and Liewer as follows:

$$v_E = \frac{cE_0}{B}$$

$$v_\Delta = -\frac{T_e}{m\omega_{ce}}\left(\frac{1}{n_e}\frac{dn_e}{dx} - \frac{1}{B}\frac{dB}{dx} - \frac{{k_\perp}^2 {a_e}^2}{2}\frac{1}{T_e}\frac{dT_{\perp e}}{dx}\right)$$

$${c_s}^2 = \frac{T_e}{m_i}$$

In the above expressions, a_e is the electron gyroradius. The frequency of the LHDI waves is given by Krall and Liewer as:

$$\omega_R \approx \frac{\omega_{pi}}{\sqrt{1 + \frac{4\pi nmc^2}{B^2}}}$$

Here, x is the direction of the electric field which is perpendicular to the magnetic field, B, and which is responsible for the electron drift v_E.

Further, Krall and Liewer found that the MTSI could exist in similar conditions but in the absence of strong gradients, as long as the ions and electron temperatures satisfied the following condition:

$$v_E > \sqrt{\frac{T_e + T_i}{m_i}}$$

For the MTSI, the waves would exhibit maximum growth at the following frequency:

$$\omega_R \approx \frac{\omega_{pi}}{\sqrt{1+\frac{4\pi nmc^2}{B^2}}}\left(\frac{v_E}{c_s}\right)^{1/5}$$

Krall and Liewer derived their instability theory in slab geometry, although the geometry of the experiments which motivated the study was cylindrical. They were investigating instabilities observed in theta pinches, which represent an experimental arrangement for controlled fusion. The slab geometry is shown in Figure 7.

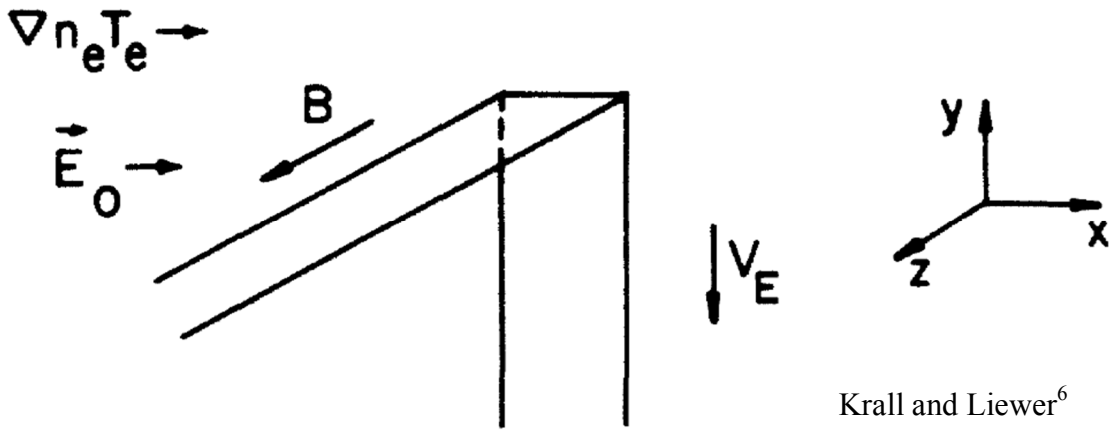

Krall and Liewer[6]

Figure 7 - Slab geometry of LHDI and MTSI theory. This figure is excerpted from the paper of Krall and Liewer,[6] in which they use the slab geometry to derive the theory of the LHDI and MTSI. In the paper and in this work, the experimental geometry was actually cylindrical. The use of the simplified slab geometry requires that the perpendicular electric field be relatively uniform compared to the wavelength of the unstable waves. Compare this geomertry to that shown in Figure 13.

III. STABILITY ANALYSIS OF EXPERIMENTAL DATA

The previous chapter reviewed some of the published theory of instabilities of interest in magnetic nozzles. The goal of this chapter is to compare the experimentally characterized plume of the VX-200 with instability theory for some specific types of plasma instability, i.e., a stability analysis. These particular instabilities have been suggested as being the cause of observed waves in the experiment.[1]

A. LHDI Stability Analysis

In this section, experimentally determined plasma parameters from the plume of the VX-200 experiment are examined to see if the theoretical conditions for the LHDI are satisfied. The quantities relevant to the LHDI are plotted as color maps covering the VX-200 measurement region. Finally, the analysis of the instability criterion is compared to maps of observed instabilities in the experimental plasma plume. The goal of this effort is to assess the likelihood that the radial electric field oscillations in the plume of the VX-200 were a manifestation of the LHDI.

1. Experimental Measurements of Plasma Properties

The following analysis has its basis in the discussion, in Section II.C, regarding the originally developed theory of the LHDI and the MTSI. Evaluation of the stability criterion for the LHDI amounts to an evaluation of the electric field strength necessary to create a drift speed, $v_E = cE_0/B$, such that the equation, $v_\Delta v_E \geq {c_s}^2$, is true.[6] The quantities which determine the net gradient drift speed,

$$v_\Delta = -\frac{T_e}{m\omega_{ce}}\left(\frac{1}{n_e}\frac{dn_e}{dx} - \frac{1}{B}\frac{dB}{dx} - \frac{{k_\perp}^2 {a_e}^2}{2}\frac{1}{T_e}\frac{dT_{\perp e}}{dx}\right)$$

were measured and tabulated by Olsen et al.[1] during several campaigns of experimental investigation of the VX-200 exhaust plume. The publications of Olsen[1] and Olsen et al[5] contain details of the experimental methods that produced the data that are analyzed here.

The color maps in Figure 8 through Figure 12 show the quantities which will be used to calculate the net gradient drift speed in the VX-200 plume.

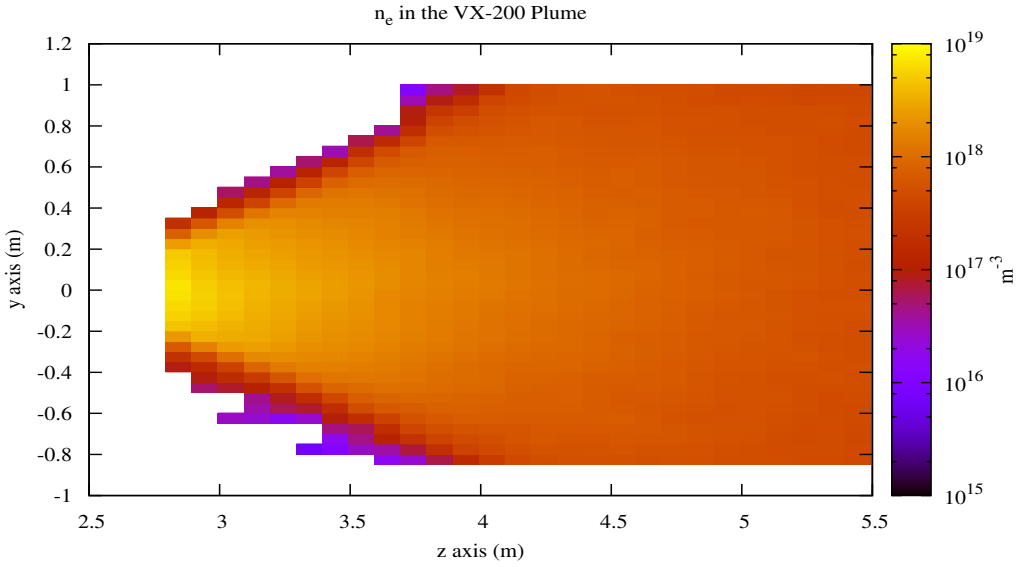

Figure 8 - Electron density in VX-200 plume. These data were measured by a swept Langmuir probe, and were first reported by Olsen.[1] The z-direction is along the magnetic nozzle axis. To gather these data, diagnostic probes were translated in 0.1 m steps along the z-axis, and 0.5 m steps along the y-axis.

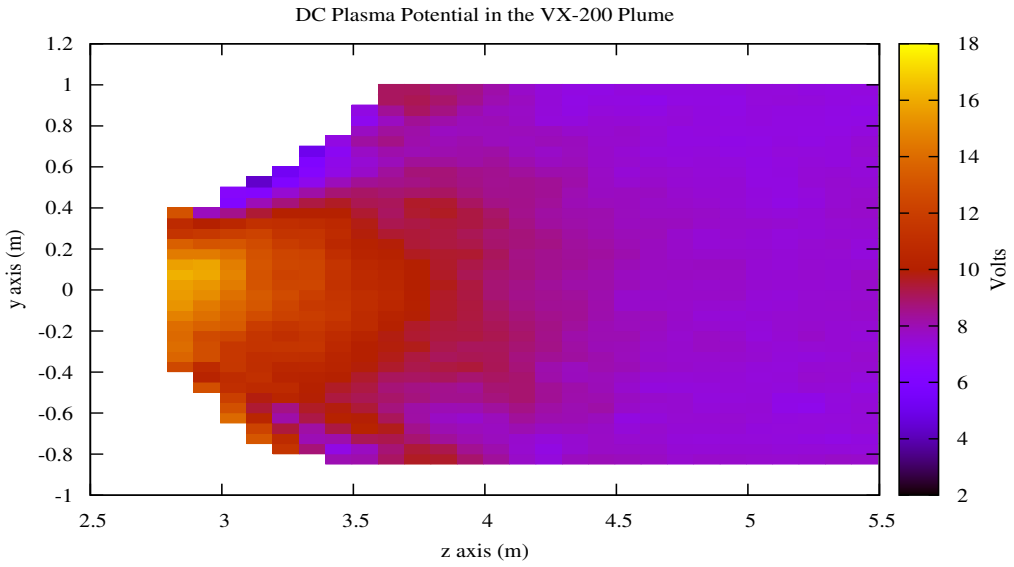

Figure 9 – Plasma potential in the VX-200 plume. These data were measured by the swept Langmuir probe, and were first reported by Olsen.[1] The z-direction is along the magnetic nozzle axis. To gather these data, diagnostic probes were translated in 0.1 m steps along the z-axis, and 0.5 m steps along the y-axis.

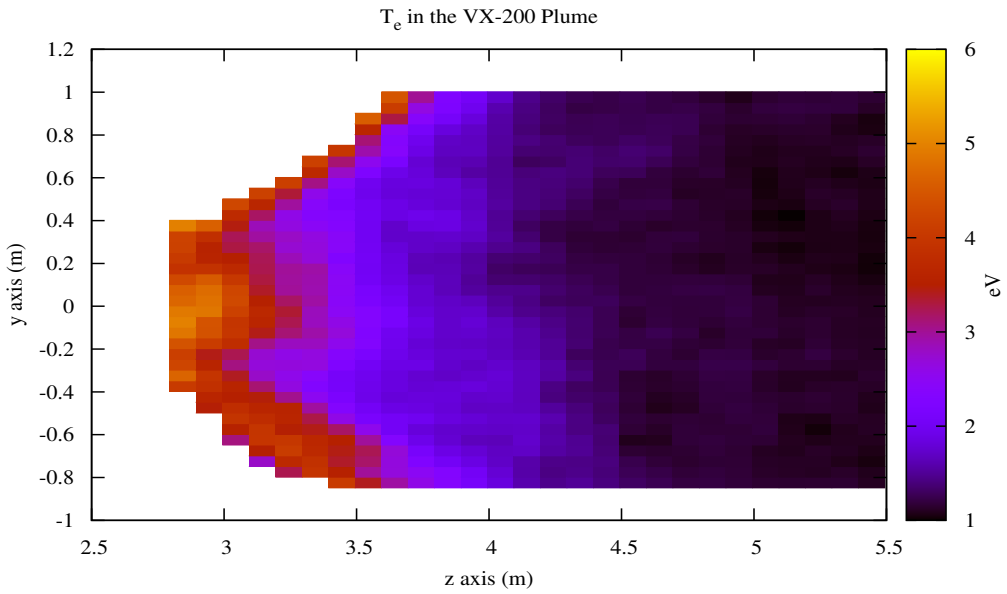

Figure 10 - Electron temperature in VX-200 plume. These data were measured by a swept Langmuir probe, and were first reported by Olsen.[1] The z-direction is along the magnetic nozzle axis. To gather these data, diagnostic probes were translated in 0.1 m steps along the z-axis, and 0.5 m steps along the y-axis.

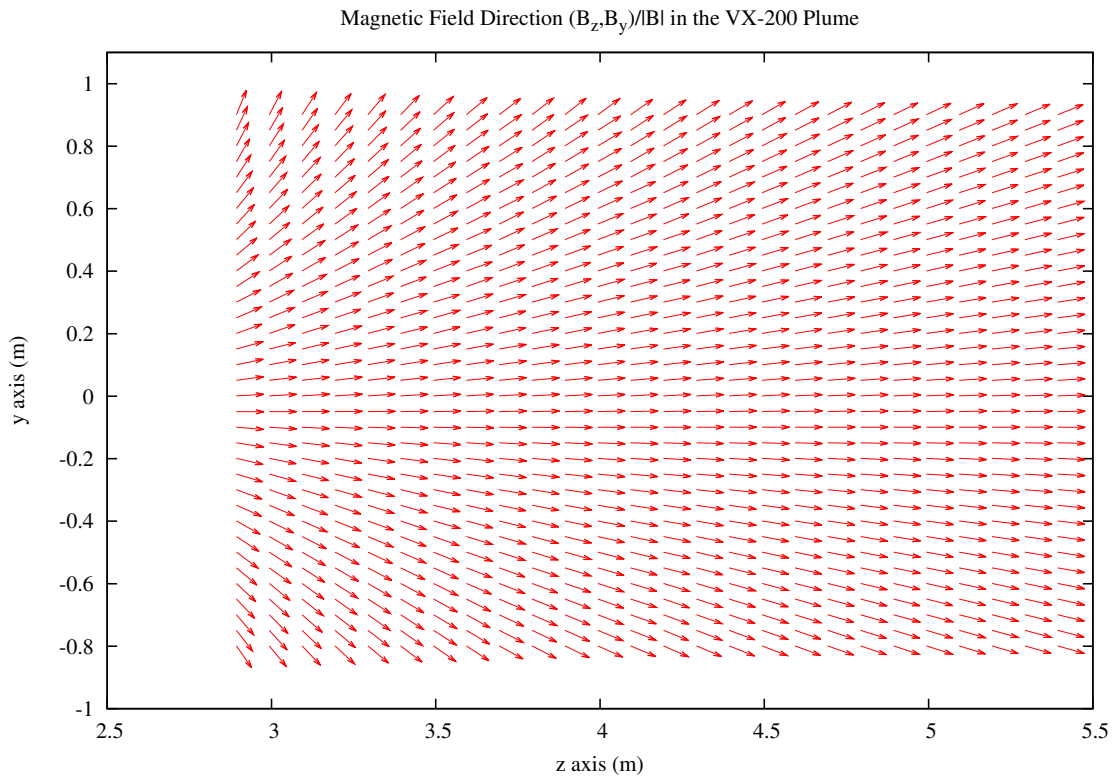

Figure 11 - Magnetic field direction in the VX-200 plume. These data were measured by a three-axis Hall probe magnetometer, and were first reported by Olsen.[1] The x-component of the field was also measured, but it is not shown. To gather these data, diagnostic probes were translated in 0.1 m steps along the z-axis, and 0.5 m steps along the y-axis.

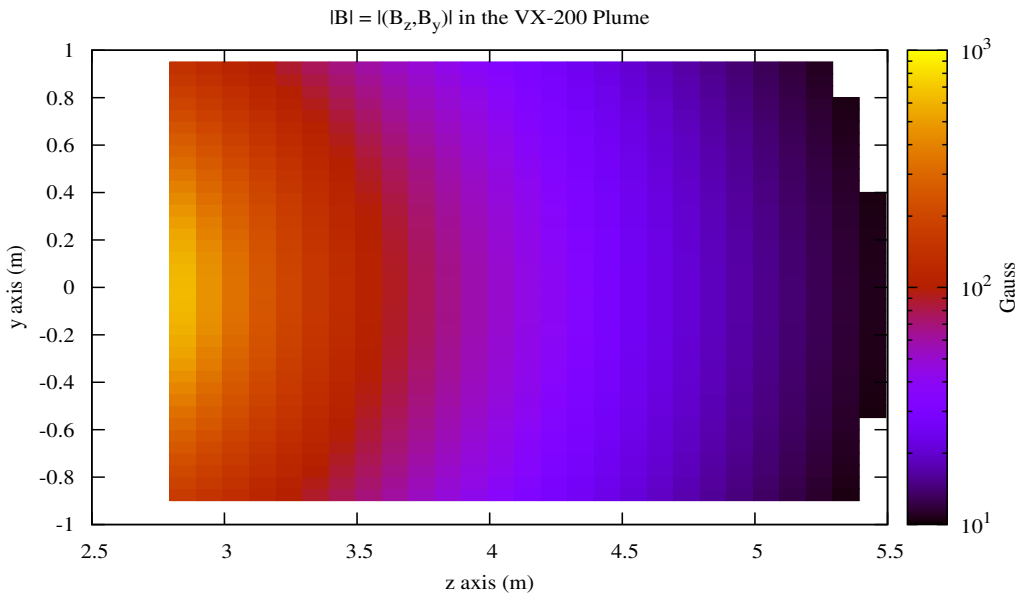

Figure 12 – Magnetic field strength in the VX-200 plume. These data were measured by a three-axis Hall probe magnetometer, and were first reported by Olsen.[1] In this calculation, the x-component of the magnetic field was ignored. To gather these data, diagnostic probes were translated in 0.1 m steps along the z-axis, and 0.5 m steps along the y-axis.

2. Finding Perpendicular Gradients

Recall, from Figure 7, that Krall and Liewer define their x-direction (in slab geometry) as being perpendicular to the background magnetic field and in the direction of the electric field (whatever its cause). To faithfully apply this theory to the diverging magnetic nozzle of the VX-200, the x-direction was reinterpreted to be perpendicular to the magnetic field and radially outward, as this is the direction one would expect for an electric field that results from the inwardly detaching, ballistic ions, and the still (temporarily) magnetized electrons. Figure 13 shows a simplified cartoon of the general behavior of the ions and electrons in the upstream part of the plume and the coordinate system used in the following analysis. Experimental evidence of the inwardly detaching ions is discussed in Olsen[1] and Olsen et al.[5]

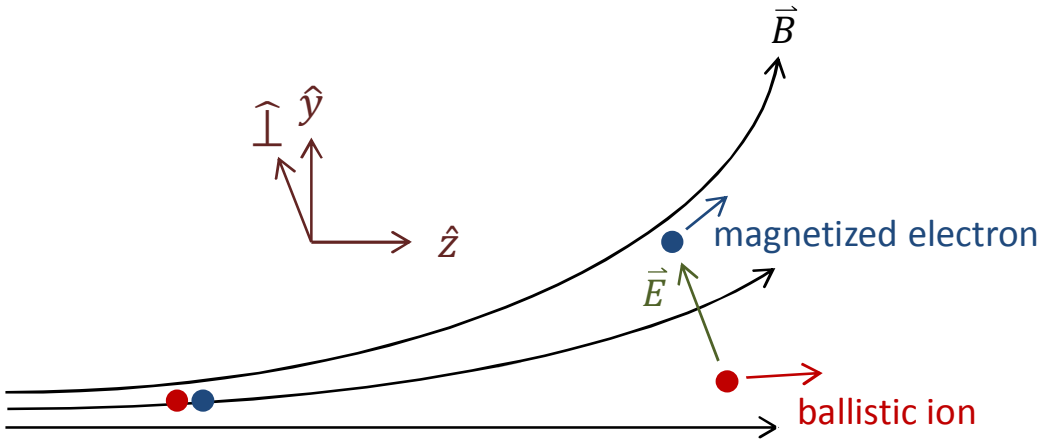

Figure 13 – Coordinate system used in VX-200 experimental data and in the application of the LHDI theory[6] to the magnetic nozzle geometry. Compare this figure to the slab geometry of Krall and Liewer shown in Figure 7 on page 14. This cartoon shows a simplified picture of the ions detaching radially inward during ICH operation, while the electrons remain magnetized. The blue arrow should be thought of as the velocity of the elctron's guiding center. See Figure 14 for an example of the experimental evidence of this phenomenon.

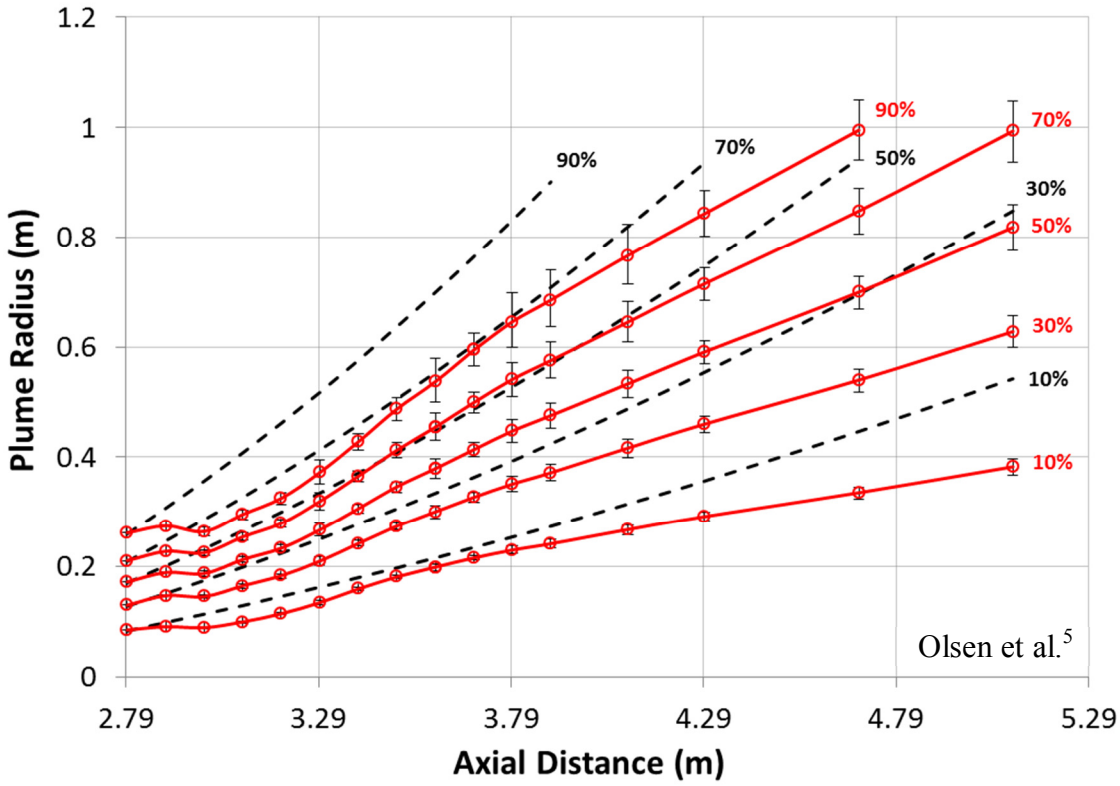

Figure 14 – Comparison of lines of constant integrated ion flux (solid red) to lines of constant integrated magnetic flux (dashed black), as published by Olsen et al.[5] This analysis supports the theory of the ions detaching radially inward during ICH operation, as depicted in Figure 13.

Using the new coordinates shown in Figure 13, the equation for the net drift speed can be rewritten:

$$v_{\Delta} = -\frac{T_e}{m\omega_{ce}}\left(\frac{1}{n_e}\frac{dn_e}{d\perp} - \frac{1}{B}\frac{dB}{d\perp} - \frac{{k_{\perp}}^2 {a_e}^2}{2}\frac{1}{T_e}\frac{dT_{\perp e}}{d\perp}\right)$$

where $\perp$ replaces the x-direction of Krall and Liewer.[6]

The perpendicular gradients were determined at each point of the grid on which the original experimental data was acquired. This process began with finding the gradients in the z-y plane on which the measurements were tabulated:

$$\frac{dn_e}{dz}(i,j) = \frac{n_e(i+1,j) - n_e(i-1,j)}{\Delta z}$$

$$\frac{dn_e}{dy}(i,j) = \frac{n_e(i,j+1) - n_e(i,j-1)}{\Delta y}$$

$$B(i,j) = \sqrt{{B_z}^2 + {B_y}^2}(i,j)$$

$$\frac{dB}{dz}(i,j) = \frac{B(i+1,j) - B(i-1,j)}{\Delta z}$$

$$\frac{dB}{dy}(i,j) = \frac{B(i,j+1) - B(i,j-1)}{\Delta y}$$

$$\frac{dT_e}{dz}(i,j) = \frac{T_e(i+1,j) - T_e(i-1,j)}{\Delta z}$$

$$\frac{dT_e}{dy}(i,j) = \frac{T_e(i,j+1) - T_e(i,j-1)}{\Delta y}$$

$$E_z(i,j) = \frac{\varphi_p(i-1,j) - \varphi_p(i+1,j)}{\Delta z}$$

$$E_y(i,j) = \frac{\varphi_p(i,j-1) - \varphi_p(i,j+1)}{\Delta y},$$

where i and j, respectively, refer to the z and y positions of the experimental measurement grid. The finite differencing scheme detailed above is one in which the calculated changes in the measurements are collocated with the measurements themselves. This quality is necessary since the terms in the net drift speed equation are inverse scale lengths, i.e., spatial decay rates, e.g., $\frac{1}{n_e}\frac{dn_e}{d\perp}$. The finite differencing

scheme used here is similar to that used in particle-in-cell simulation to solve Poisson's equation for the electric field on a simulation grid.[10]

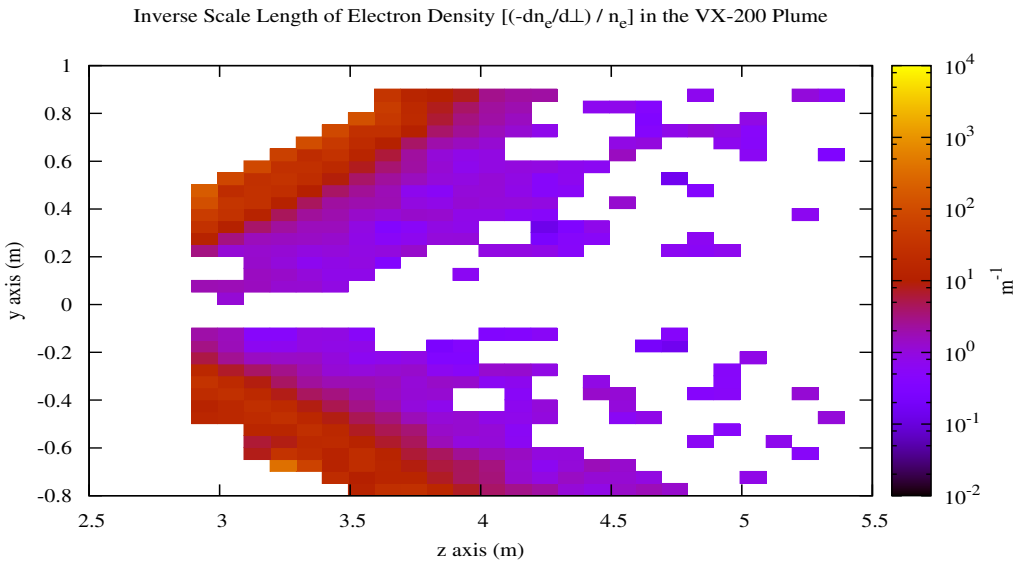

Figure 15 – Inverse scale length of the measured electron density. This calculation is performed on the data shown in Figure 8. The gradient is calculated in the direction perpendicular to, and radially outward from, the local magnetic field line, as depicted in Figure 13. This quantity is one of the gradients which can contribute to the drifts necessary for the 'strong drift mode' of the lower hybrid drift instability.[6] The density gradient shown here is the dominant contribution to the electron drift speed. Values are plotted only where the sign of the gradient contributes to a drift that would support the growth of the LHDI.

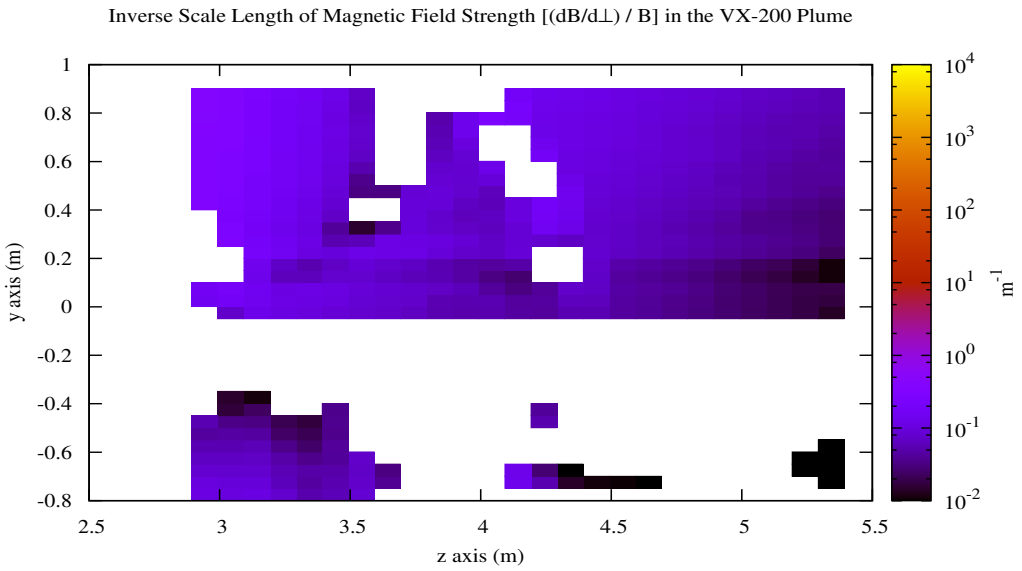

Figure 16 - Inverse scale length of the measured magnetic field strength. This calculaiton is performed on the data shown in Figure 12. The gradient is calculated in the direction perpendicular to, and radially outward from, the local magnetic field line, as depicted in Figure 13. This quantity is one of the gradients which can contribute to the drifts necessary for the 'strong drift mode' of the lower hybrid drift instability.[6] Values are plotted only where the sign of the gradient contributes to a drift that would support growth of the LHDI. The magnitudes shown here are relatively small because the field strength gradient points mostly in a direction parallel to the field.

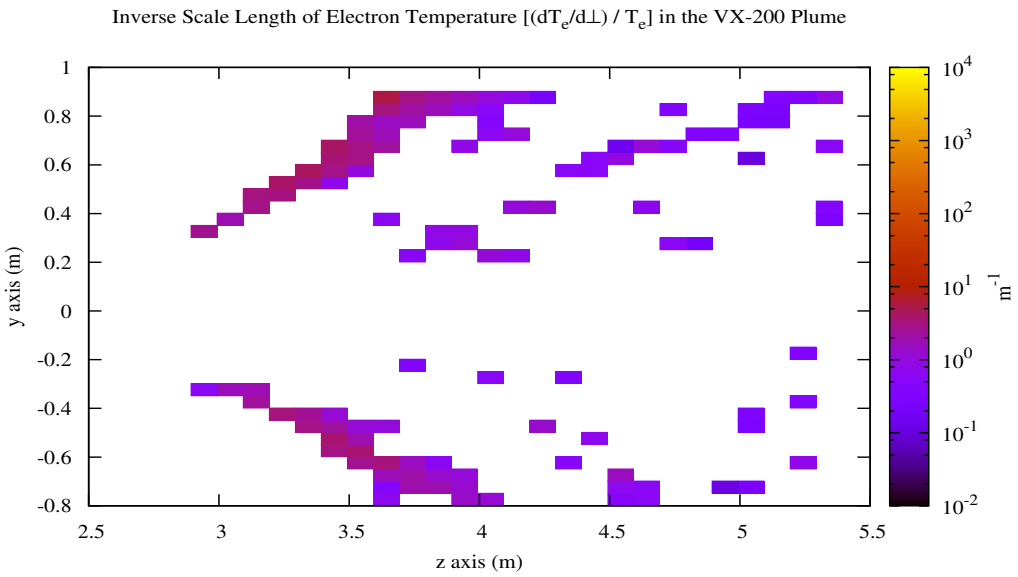

Figure 17 - Inverse scale length of the measured electron temperature. This calculation is performed on the data shown in Figure 10. The gradient is calculated in the direction perpendicular to, and radially outward from, the local magnetic field line, as depicted in Figure 13. This quantity is one of the gradients which can contribute to the drifts necessary for the 'strong drift mode' of the lower hybrid drift instability.[6] Values are plotted only where the sign of the gradient contributes to a drift that would support growth of the LHDI. The temperature gradients shown here were excluded from the calculation of the net drift speed, because there is some uncertainty about the accuracy of the temperature measurments in the presence of electromagnetic interference; the swept Langmuir probe used for these measurements was not RF compensated. If the drift due to this gradient were to be included, it would make it more likely that observed conditions support the existence of the LHDI.

To find the perpendicular component of the calculated gradients, the coordinate system was rotated to the local magnetic field axis:

$$\theta_B = \tan^{-1}\frac{B_y}{B_z}$$

$$\frac{1}{n_e}\frac{dn_e}{d\perp} = \frac{1}{n_e}\left(\frac{dn_e}{dz}\sin\theta_B + \frac{dn_e}{dy}\cos\theta_B\right)\frac{B_y}{|B_y|}$$

The operation above finds the y-component of the inverse scale length of density in the rotated coordinate frame. The factor $\frac{B_y}{|B_y|}$ is necessary to orient the gradient radially outward from the magnetic axis, as shown in Figure 13.

3. Calculating the Minimum Electric Field for the LHDI

The perpendicular scale lengths of the electron density, temperature, and magnetic field were calculated using the magnetometer and guarded flux probe data from VX-200 plume. These three gradients can contribute to the net gradient drift speed according to the modified equation of Krall and Liewer. In this analysis, however, only the density gradient drift was used. This drift is known as the Diamagnetic drift in Chen.[11] The resulting electron drift speed is plotted in Figure 18. A justification for the exclusion of the non-uniform field drift and the temperature gradient drifts follows.

The density gradient is by far the dominant contribution to the electron drift speed. As one can see in Figure 8, the electron density changes rapidly at the well-defined plume edge. The perpendicular gradient in the magnetic field, shown in Figure 16, is comparatively small because the region of interest is removed from the magnet coils by several coil radii. As such, the gradient in magnetic field strength is mostly parallel to the field, not perpendicular to it. Figure 11 and Figure 12 illustrate this point. Finally, Figure 10 and Figure 17 show a distinct warming of the electron

temperature near the plume edge, leading one to consider the effect of the temperature on the net drift speed. However, the warming corresponds to regions of lower electron density and lower signal-to-noise ratio at the guarded flux probe. There is some uncertainty about the accuracy of the temperature data in these regions; therefore, the temperature gradient was not included in the final calculation of the drift speed. Because the direction of the observed temperature gradient is such that it would have added to the already substantial density drift, the exclusion of the temperature drift leads to a more conservative estimate of the electric field necessary for the LHDI.

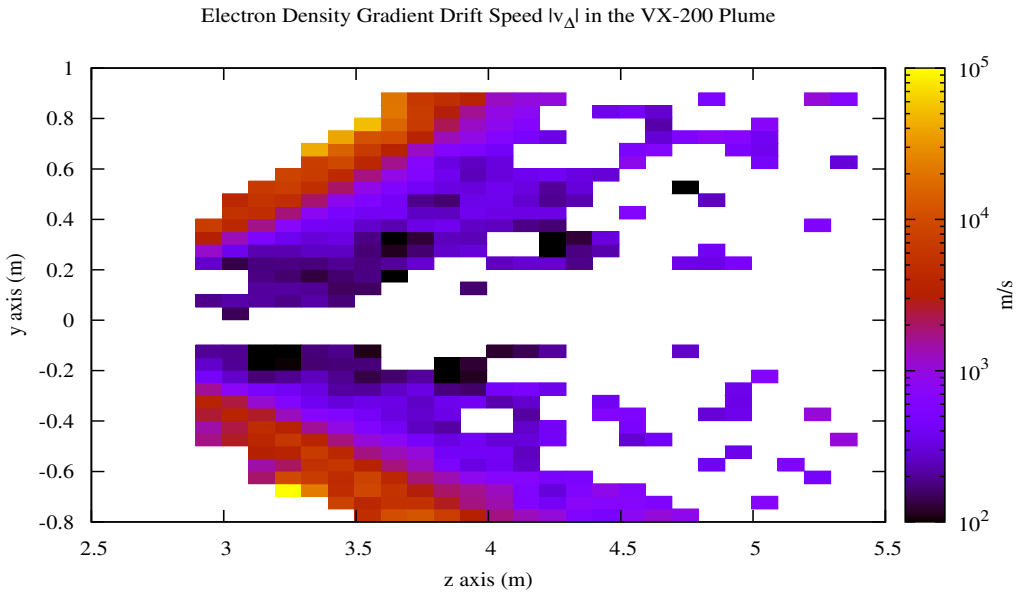

Figure 18 –Density gradient drift speed in the azimuthal direction. This figure shows the drift speed due to the electron density gradient shown in Figure 15. To produce the 'strong drift mode' of the lower hybrid drift instability, this drift must be in the same direction as a drift produced by a radially outward pointing electric field.[6] Also, the product of these drift velocities must be greater than the square of the ion acoustic speed.

Combining the equations from Section II.C for the LHDI criterion, electric field drift speed, and the gradient drift speed yields an expression for the minimum electric field:

$$E_{LHDI} = \frac{eB^2}{\frac{m_i}{n_e}\frac{dn_e}{d\perp}}$$

Note that the units have been changed from Gaussian to MKS. This quantity, shown in Figure 19, is the magnitude of a perpendicular and radially outward pointing electric field which would be sufficient to excite the strong drift mode of the LHDI.

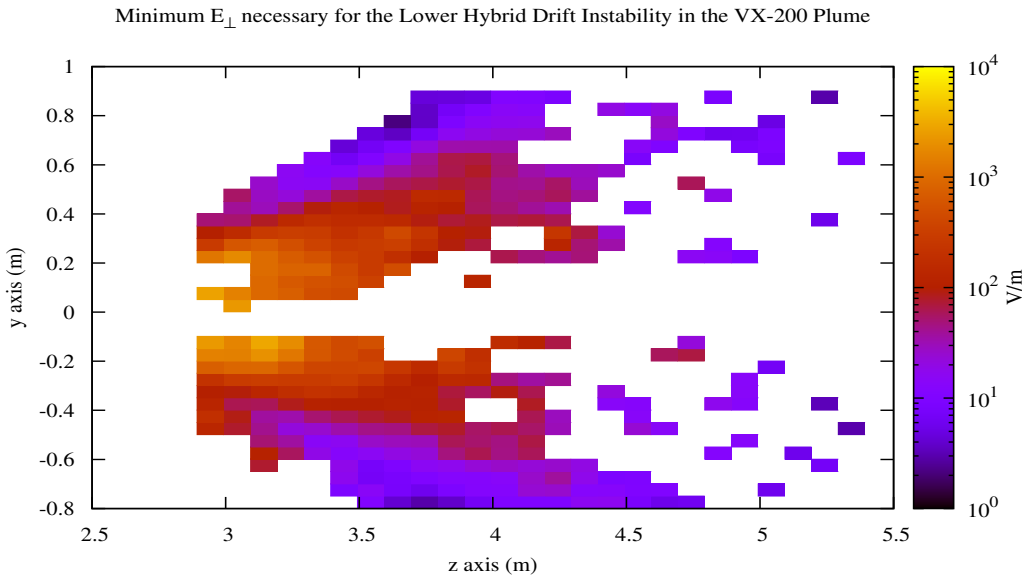

Figure 19 - Electric field necessary for the 'strong drift mode' of the LHDI.[6] This figure shows the strength of an electric field that would produce a drift velocity that would be large enough, in combination with the density gradient drift velocity shown in Figure 18, to allow growth of the LHDI in the VX-200 plume. The blank regions are ones where the sum of the gradient drifts would point in the wrong direction to support the LHDI. Compare the magnitudes of this figure with those of the measured oscillating electric fields shown in Figure 4, and with the calculated DC fields shown in Figure 20.

4. Comparing the Minimum Field to the Measured DC Field

Having now calculated the electric field necessary for the LHDI, one can analyze the plume measurements to determine if this field was present. Using the measurements of the plasma potential, shown in Figure 9, one can calculate the DC electric field in the plasma according to Poisson's equation. The perpendicular electric field can be found in a manner similar to that used to find the perpendicular density gradient.

$$\overrightarrow{E_{DC}} = -\nabla\varphi_p$$

$$E_{\perp} = \left(E_z \sin\theta_B + E_y \cos\theta_B\right)\frac{B_y}{|B_y|}$$

$$where\ \ \theta_B = \tan^{-1}\frac{B_y}{B_z}$$

Figure 20 shows the DC perpendicular electric field as calculated in the method shown above.

Upon comparing Figure 20 to Figure 19, it is evident that the DC electric field in the VX-200 plume was likely too weak to excite the strong drift mode of the LHDI; therefore, if the observed electric field oscillations were a form of the LHDI, some other energy source (besides the density gradient and DC electric field) must have contributed to their excitation.

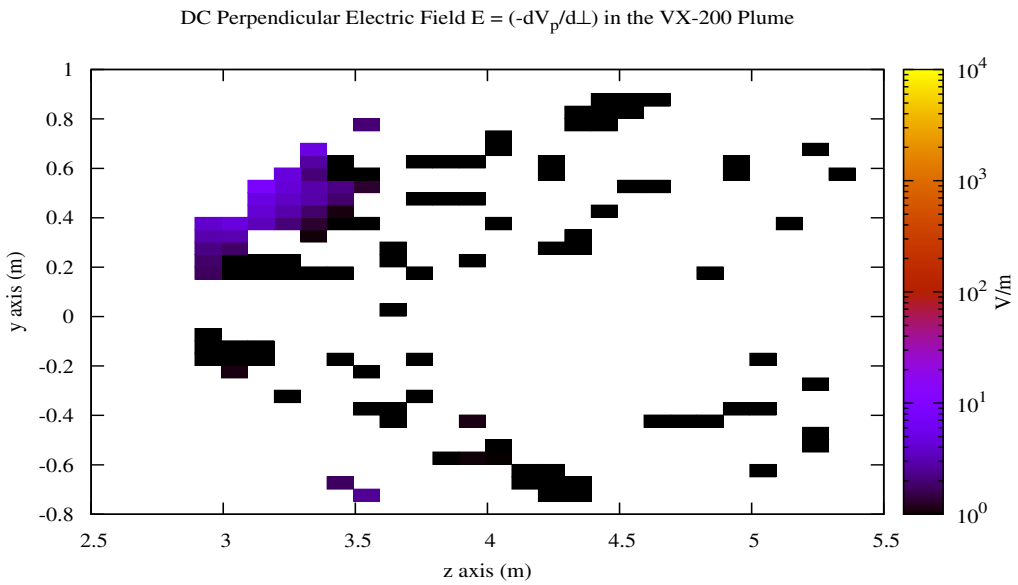

Figure 20 – Perpendicular DC electric field in the VX-200 plume as calculated from the measurements of plasma potential shown in Figure 9. Values are plotted only where the calculated electric field points radially outward. The magnitude scale is the same used in Figure 19. Comparing these electric field values to those in Figure 19, it is clear that the DC field is probably insufficient to excite the LHDI on its own.

5. Connecting Observed Oscillations to the Drive Frequency

A closer examination of the spectrum in Figure 6 reveals an energy source which could have made the LHDI possible. The measured electric field oscillations are actually high harmonics (10f and higher) of the drive frequency of the ICH stage of the VX-200. In fact, harmonics of the ICH are seen throughout the spectrum. The harmonics at frequencies greater than 5 MHz, however, are significantly amplified in magnitude. This frequency happens to be the minimum of the range of the possible

frequencies of the LHDI, if it were to exist in the VX-200 plume. The calculation of the LHDI frequency is detailed in the following paragraph.

The frequency of LHDI oscillations, if they exist, would be determined by the local electron density and magnetic field strength. The angular frequency and growth rate are given by Krall and Liewer[6] as

$$\omega_R \approx \omega_{pi}(1 + 4\pi n_e m_e c^2/B^2)^{-1/2}$$

$$\gamma \approx \sqrt{2}\omega_R$$

The frequency can be rewritten in MKS units as

$$f_{LHDI} \approx \frac{1}{2\pi}\sqrt{\frac{\frac{n_e e^2}{m_i \varepsilon_0}}{1 + \frac{n_e m_e}{B\varepsilon_0}}}$$

This quantity was calculated from the densities and fields shown in Figure 8 and Figure 12, respectively.

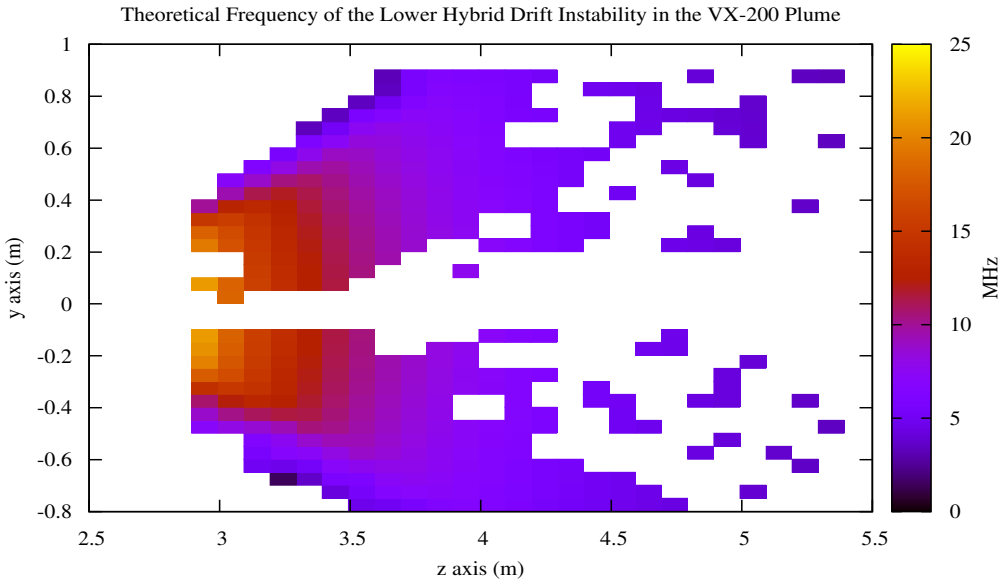

Figure 21 – Predicted frequency of lower hybrid drift oscillations.[6] This figure shows what the frequency of the LHDI would be, if it were to exist, in various parts of the VX-200 plasma plume. These frequencies may be compared to those of the observed oscillations shown in Figure 4 and Figure 6, which were generally in the HF range of 5-10 MHz. The frequency range of the instability may explain why higher harmonics of the ICH fundamental frequency are amplified in Figure 6.

The spectral and spatial coincidence of the ICH harmonic amplification with the LHDI is telling. The unamplified ICH harmonics (at frequencies < 5 MHz) shown in Figure 6 had amplitudes in the range of 50-100 V/m. According to Figure 19, these amplitudes would have been sufficient to excite the LHDI, but only along the edge of the VX-200 plume. Something causes the higher frequency (> 5 MHz) ICH harmonics to have much larger amplitudes, again, only along the plume edge. It stands to reason that the observed amplification of the ICH harmonics was a coupling of the harmonics to the LHDI.

B. MTSI Stability Analysis

In the previous section, it was shown that the criteria for the LHDI were not quite met in the VX-200 plume. The product of the theoretical drift speed produced by the measured density gradient, and the DC electric field found by interpolating the plasma potential, was not large enough to satisfy the necessary condition:

$$v_\Delta v_E \geq {c_s}^2$$

This does not mean that the LHDI was not playing a role in the observed electric field oscillations of Figure 6. It means only that the LHDI was not solely responsible. It was conjectured that the LHDI could have been excited by harmonics of the ICH stage of the VX-200 rocket core.

In this section, a similar analysis is performed using the criteria of the MTSI. The MTSI is closely related to the LHDI; the differences being that the MTSI does not require a strong gradient drift, and that the MTSI has a small component of its wave vector parallel to the magnetic field (the LHDI is purely perpendicular). The necessary condition for the MTSI is, again:

$$v_E > [(T_e + T_i)/m_i]^{1/2}$$

The measured ion and electron temperatures are used to determine the minimum electric field to satisfy this condition.

At the end of this section, there is a brief discussion concerning which of the two modes is more likely to have contributed to the observed electric field oscillations.

1. Experimental Measurement of Ion Temperature

Ion temperatures in the VX-200 plume were determined by a retarding potential analyzer (RPA).[12] The RPA was a planar trap consisting of four grids: entrance attenuator, electron suppressor, ion analyzer, and secondary suppressor. The ion analyzer was swept in voltage while collecting ion current. The resulting current-voltage (I-V) characteristic revealed the ion energy distribution. Using the method of least squares, drifting Maxwellian distributions were fit to the I-V traces to determine the ion temperature and drift speed. The I-V traces were translated so that the zero of the retarding potential matched the plasma potential as determined by the swept Langmuir probe. An example of the result of the RPA analysis routine is shown in Figure 22. Olsen[1] compiled a map of the ion temperatures measured in the manner described above; this is shown in Figure 23. The ion temperature during the ICH operation typically ranged from 5 eV along the plume edge to near 40 eV in the interior.

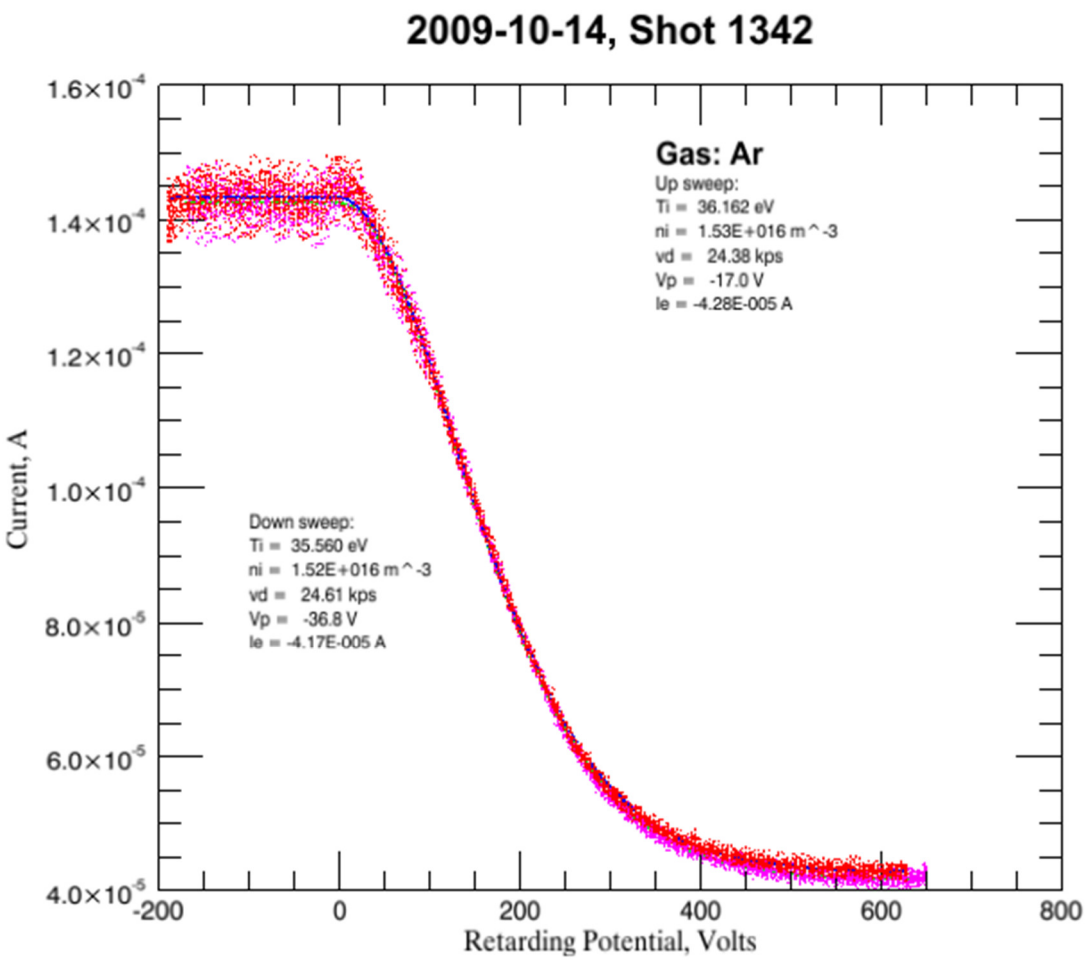

Figure 22 – Sample RPA trace. This figure shows a particularly quiet I-V trace from the RPA, taken during the ICH time-window of a VX-200 pulse. Several up- and down-sweeps of the bias voltage are superimposed in this figure. Red dots correspond to the ion collector current while the bias is being swept up, while pink dots correspond to that of the down-sweep. Also shown is the drifting Maxwellian fit to the data, which is how the ion temperature was determined. The blue line is the fit to the up-sweep data, while the light green line (barely visible) is that for the down-sweep data. This figure is an example of the output of an analysis routine for the RPA data. The routine is written in the Interactive Data Language. More details can be found in Bering et al.[12]

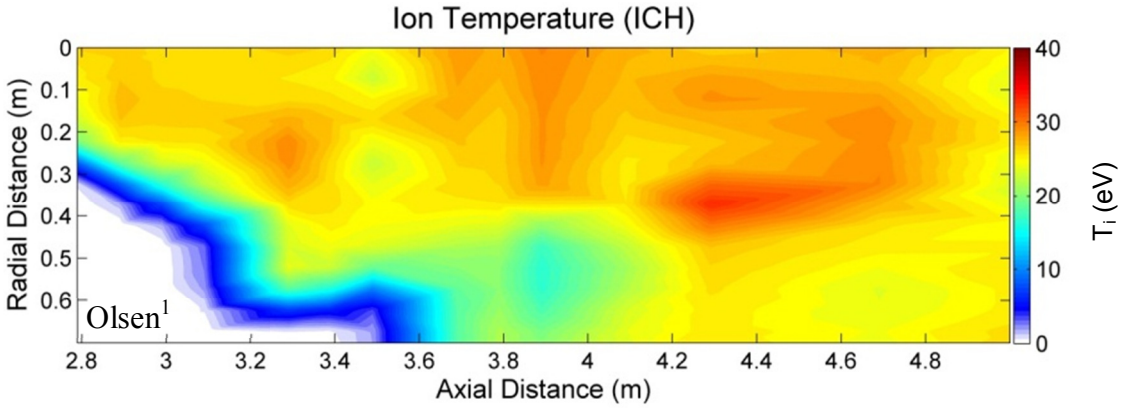

Figure 23 – Ion temperature map in the VX-200 plume. This figure is excerpted from Olsen.[1] The color map shows the ion temperature as measured by the RPA in the manner described above and exemplified in Figure 22. These temperatures correspond to the time window of ICH operation. Ion temperatues during helicon-only operation are approximately four times lower.

2. Minimum Electric Field for the MTSI

In this subsection, the measured ion and electron temperatures will be used to determine the minimum electric field necessary to produce the MTSI. Like the LHDI, the MTSI requires an electric field pointing perpendicular to the magnetic field; however, there is no need for a gradient in electron density, electron temperature, or magnetic field. For the MTSI mode to be unstable, the drift speed due to the electric field need only satisfy the following condition:[6]

$$v_e > \sqrt{\frac{T_e + T_i}{m_i}}$$

$$where:\ v_e = \frac{cE_0}{B}$$

These expressions can be solved for the minimum electric field and rewritten in MKS units as follows:

$$E_{MTSI} > B\sqrt{\frac{T_e + T_i}{m_i}}$$

The above expression for the minimum electric field can be evaluated at a point of interest in the VX-200 plume, using the measured parameters from a region where instabilities were observed. Using the magnetic field from z=3.3 m and y=0.3 m, B=160 G, and representative temperatures for the ions and electrons, T_i = 25 eV and T_e = 3 eV, the minimum electric field is found to be $E_{MTSI} \approx 131$ V/m. This result is similar to the minimum electric field for the LHDI shown in Figure 19.

C. Distinguishing Between LHDI and MTSI

The presence of the string gradient in electron density might lead one to suspect the LHDI as being more likely to contribute the observed instabilities. As shown in the previous subsection, however, the MTSI is equally likely to exist, based on the measured temperatures and magnetic field strength. One way to distinguish between the two wave modes is to determine the relative angle between the oscillating wave vector and the local magnetic field vector; the LHDI should be purely perpendicular, while the MTSI has a small component along the magnetic field. The wave vector could be determined by measuring all three spatial components of the oscillating electric field.

The LHDI and MTSI also differ slightly in the frequency of maximum growth rate, which might offer another means of distinguishing between the two wave modes. The frequencies of maximum growth are given by[6]:

$$\omega_{LHDI} \approx \omega_{pi}(1 + 4\pi n_e m_e c^2/B^2)^{-1/2}$$

$$\omega_{MTSI} \approx \omega_{pi}(1 + 4\pi n_e m_e c^2/B^2)^{-1/2}(v_E/c_S)^{1/5}$$

In the spectrum shown in Figure 6, however, the instability appears to exist at several distinct frequencies. One approach at distinguishing between wave modes might be to compare the frequency of greatest electric field magnitude with the theoretical frequencies above. This could lead to a conclusion about which of the two waves was the dominant contributor to the oscillations. Calculation of the MTSI frequency requires a precise measurement of the background electric field, which is not available for the VX-200 data.

D. Cold, Uniform Plasma Dispersion Analysis

In addition to the analysis of specific instability modes detailed in the previous sections, the cold, homogenous plasma stability of the VX-200 plume was also investigated. This section presents the results of efforts to show the plasma parameters on a Clemmow Mullaly Allis (CMA) diagram, which is a representation of the possible wave modes for uniformly magnetized plasma with T_i=T_e=0.[11, 13]

Before examining the cold plasma wave modes, it is important to quantitatively discuss the validity of this approach. One might argue that the CMA

diagram is of limited use in the study of VX-200 plume edge instabilities because the ion and electron temperatures do not meet this condition ($T_i > T_e$), and because there is a significant density gradient along the plume edge. Figure 8 and Figure 15, on pages 16 and 25, respectively, show the magnitude of the density gradient. In the following paragraphs, the assumption of cold, uniform plasma is tested against the measured conditions.

The fundamental assumption in the derivation of the cold plasma dispersion relation is that the gradient of the fluid stress tensor is small compared to the electromagnetic forces on the plasma particles.[13] This can be seen in the equation of motion for a fluid of charged particles:

$$nm\frac{d\mathbf{v}}{dt} = nq(\mathbf{E} + \mathbf{v} \times \mathbf{B}) - \nabla \cdot \mathbf{\Phi}$$

where n is the number density and $\mathbf{\Phi}$ is the fluid stress tensor. Neglecting the electric field, the required relationship can be rewritten for the ions:

$$n_i e|\mathbf{v_i}||\mathbf{B}| \sin\theta \gg \frac{dn_i}{d\perp} k_B T_i$$

Dividing through by $n_i e$ gives:

$$|\mathbf{v_i}||\mathbf{B}| \sin\theta \gg \frac{1}{n_i}\frac{dn_i}{d\perp}\frac{k_B T_i}{e}$$

To test this inequality with measured values, some assumptions must be made. Quasineutrality is assumed, so $n_i \approx n_e$. The inverse scale length is therefore taken from the calculations shown in Figure 15, on page 25. The geometry in the region of interest is assumed to be the same as that shown in Figure 13, on page 22. The angle θ

is between the ion velocity and the magnetic field. The ion velocity and temperature are taken from representative RPA measurements, similar to those shown in Figure 22 and Figure 23, on pages 38 and 39, respectively. Substituting the measured values gives the following result:

$$\left(\sim 3 \times 10^4 \ \frac{m}{s}\right)(\sim 0.03\ T)(\sin \sim 10°) < (\sim 10^2\ m^{-1}) \frac{\left(1.6 \times 10^{-19}\ \frac{J}{eV}\right)}{(1.6 \times 10^{-19}\ C)} (\sim 20\ eV)$$

The required relationship is therefore not satisfied for the ions, at least in the region of interest. In fact, the stress tensor seems to outweigh the magnetic force in this case. The same test for the electrons would have a larger left-hand side, since the electron thermal velocity is roughly two orders of magnitude greater than that of the ions.

The conclusion of this test is that the density gradient and temperature of the ions add more complexity to the wave physics than what is captured by the cold plasma theory. To some extent, this result is consistent with the efforts to study the LHDI in the earlier parts of this chapter; the LHDI requires a drift velocity driven by gradients in the plasma. Nonetheless, the presentation of the cold, uniform wave modes may help to place the observed instabilities in context and may aid in the investigation of wave propagation from the VX-200 source region to the region of observed instability.

1. Recreation of the Stix CMA to validate the method

In the preceding introductory text, it was shown that the cold plasma theory does not fully capture the wave situation in the plasma on the edge of the VX-200

plume. A presentation of the cold plasma waves will be made, however, because doing so is the most fundamental approach to stability analysis. It is hoped that this exercise will aid in the understanding of the oscillations observed in the plasma plume. The author is encouraged by Stix's own introduction; "The cold-plasma model gives, in fact, a remarkably accurate description of the small amplitude perturbations that are possible for a hot plasma."[13] This subsection further introduces the CMA diagram and the methods by which it is generated.

The CMA diagram displays the propagating wave modes for a given species of plasma under varying conditions of density and magnetic field strength. As stated in the previous paragraph, it is assumed that the plasma is uniform and cold, and the magnetic field is uniform. The CMA diagram is split into sections by dashed lines which represent cutoffs and resonances of the various wave modes. Crossing a resonance or a cutoff usually results in a change to the shape of the wave normal surface (WNS). Each section of the diagram contains a plot of the WNS, which shows the phase velocity of each possible wave mode as a function of the angle between the wave vector and the magnetic field. The wave-normal surfaces are drawn with the magnetic field in the vertical direction. Although the WNS may change slightly within each section, Stix proves that "inside each bounded volume in parameter space the topological genera of the WNS are unchanged."

To validate the code used to generate CMA diagrams, the well-known example from Stix[13] was recreated. This diagram uses a fictional ion-to-electron mass ratio of

2.5, which allows each region of the CMA to be shown clearly on a plot with linearly scaled axes. A copy of the original is shown in Figure 24.

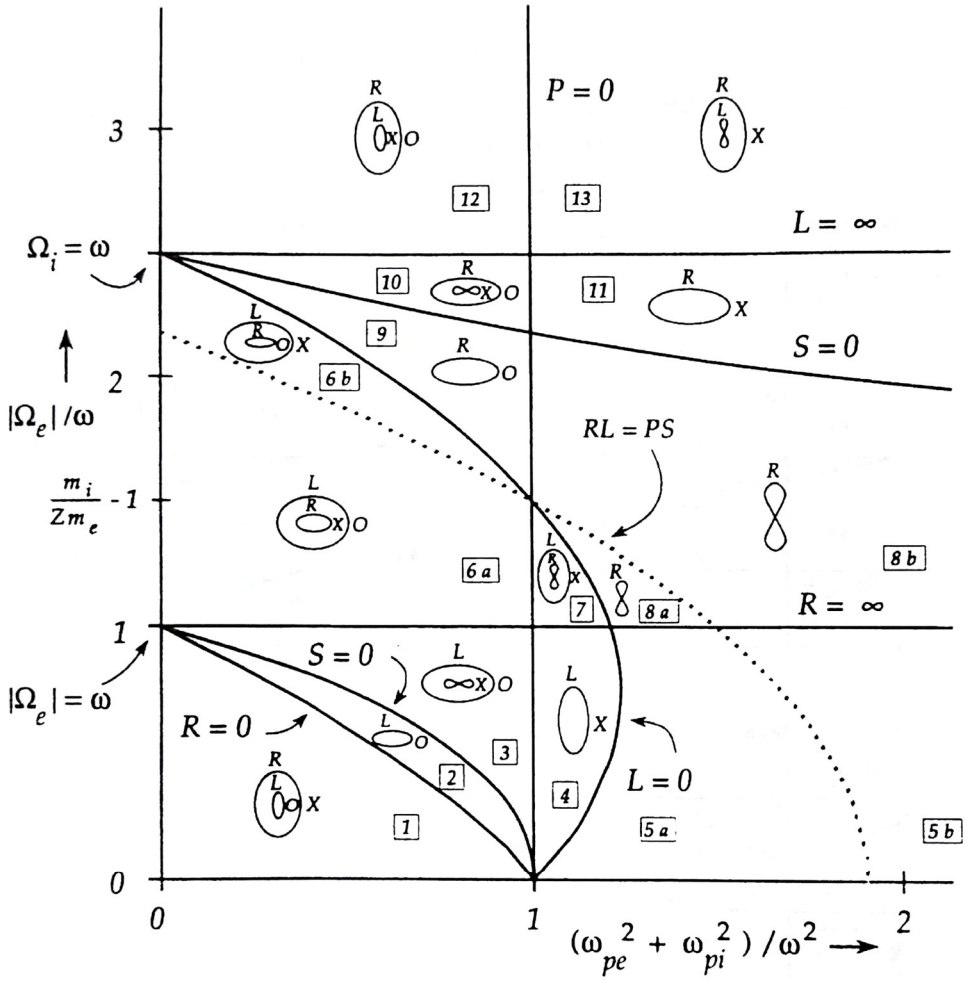

Fig. 2-1. CMA diagram for a two-component plasma. The ion-to-electron mass ratio is chosen to be 2.5. Bounding surfaces appear as lines in this two-dimensional parameter space. Cross sections of wave-normal surfaces are sketched and labeled for each region. For these sketches the direction of the magnetic field is vertical. The small mass ratio can be misleading here: the L=0 line intersects P=0 at $\Omega_i/\omega_i = 1-(Zm_e/m_i)$.

Figure 24 - CMA diagram excerpted from Stix.[13] This figure is recreated below to validate the general method of producing such a diagram. The original is shown here as a reference. For the WNS plots in each region, the magnetic field points up. 'L' and 'R' labels in the parallel direction refer, respectively, to left- and right-handed polarization of the wave. 'O' and 'X' labels in the perpendicular direction refer to the ordinary and extraordinary wave modes.[13]

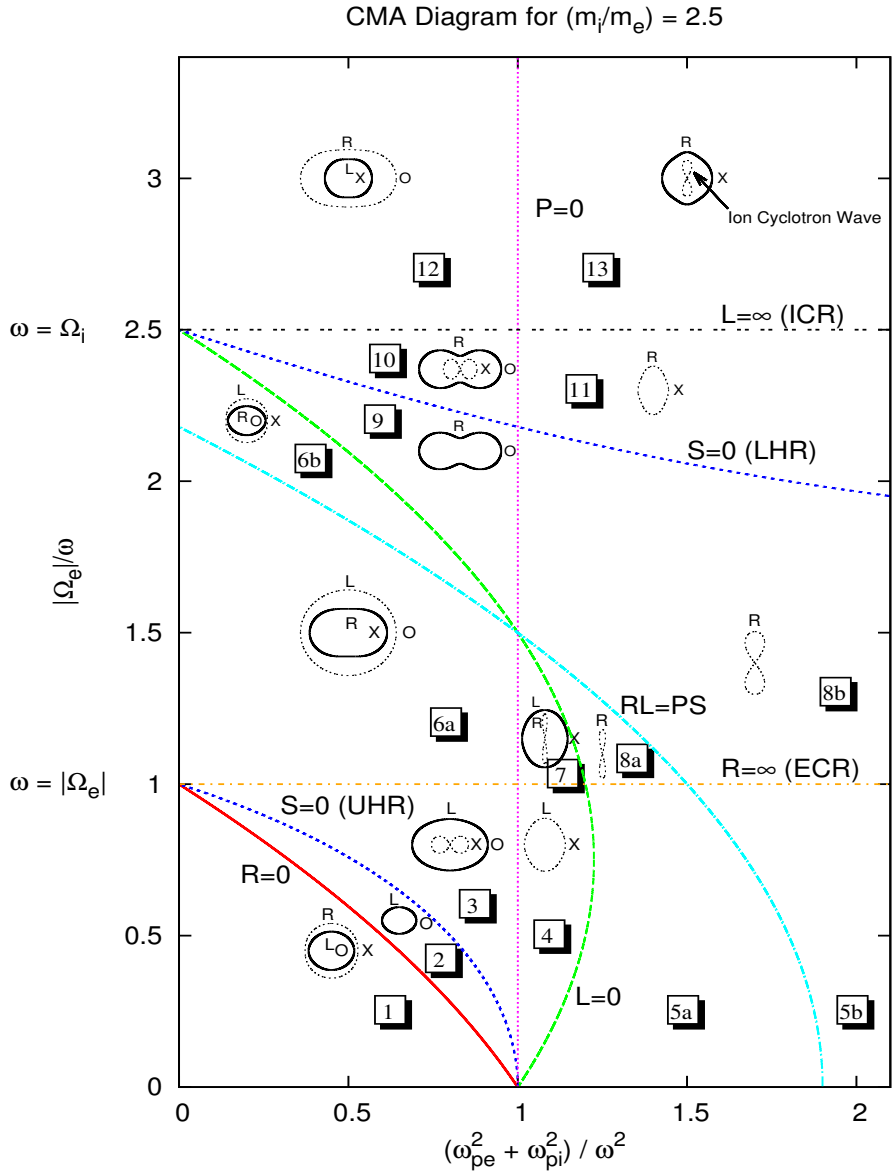

Figure 25 – CMA diagram for a plasma with ion-to-electron mass ratio of 2.5. This is a reproduction of the original diagram published in Stix.[13] The region boundaries and wave normal surfaces (WNS) have been generated by parametric plotting scripts, which are also used to create the other CMA diagrams shown subsequently in this work. Each WNS corresponds to the physical parameters at its geometric center. The ion cyclotron wave (in Region 13) is labeled because it will be discussed in a subsequent section. ICR = ion cyclotron resonance, ECR = electron cyclotron resonance, LHR = lower hybrid resonance, and UHR = upper hybrid resonance.

The bounding surfaces of the CMA diagram were taken from Stix's treatment of the dielectric tensor of a cold plasma with a single ion species:

$$\nabla \times \boldsymbol{B} = \frac{1}{c}\frac{\partial \boldsymbol{D}}{\partial t}$$

$$\boldsymbol{D}(\omega, \boldsymbol{k}) = \boldsymbol{\epsilon}(\omega, \boldsymbol{k}) \cdot \boldsymbol{E}(\omega, \boldsymbol{k}) = \begin{pmatrix} S & -iD & 0 \\ iD & S & 0 \\ 0 & 0 & P \end{pmatrix} \begin{pmatrix} E_x \\ E_y \\ E_z \end{pmatrix}$$

$$R = 1 - \frac{{\omega_{pe}}^2 + {\omega_{pi}}^2}{(\omega + \Omega_i)(\omega + \Omega_e)}$$

$$L = 1 - \frac{{\omega_{pe}}^2 + {\omega_{pi}}^2}{(\omega - \Omega_i)(\omega - \Omega_e)}$$

$$S = \frac{(R + L)}{2}$$

$$D = \frac{(R - L)}{2}$$

$$P = 1 - \frac{{\omega_{pe}}^2 + {\omega_{pi}}^2}{\omega^2}$$

The R, L and S terms above correspond to the region boundary labels in the Figure 25. To generate the bounding surfaces, the above equations were re-expressed in terms of the ion-to-electron mass ratio:

$$\mu = \left|\frac{\Omega_e}{\Omega_i}\right| = \frac{{\omega_{pe}}^2}{{\omega_{pi}}^2} = \frac{m_i}{m_e}$$

The bounding surface equations were then plotted parametrically in Gnuplot©.

The wave normal surfaces in each section of the diagram were generated by following Stix[13] from the homogenous plasma wave equation:

$$\begin{pmatrix} S - n^2\cos^2\theta & -iD & n^2\cos\theta\sin\theta \\ iD & S - n^2 & 0 \\ n^2\cos\theta\sin\theta & 0 & P - n^2\sin^2\theta \end{pmatrix}\begin{pmatrix} E_x \\ E_y \\ E_z \end{pmatrix} = 0$$

where n is the index of refraction and theta is the angle between the wave propagation vector and the magnetic field. This form of the plasma wave equation assumes that the wave vector is in the x, z plane. The presence of a nontrivial solution to this equation leads to the dispersion relation for cold plasma waves:

$$An^4 - Bn^2 + C = 0, \qquad where$$

$$A(\theta) = S\sin^2\theta + P\cos^2\theta$$

$$B(\theta) = RL\sin^2\theta + PS(1 + \cos^2\theta)$$

$$C = PRL$$

The dispersion relation was then rewritten in terms of the wave phase velocity, *u*:

$$Cu^2 - Bu + A = 0, \qquad where$$

$$u = \frac{\omega}{kc} = \frac{1}{n}$$

Two functions were defined, representing the solutions to the quadratic dispersion relation above:

$$u_{\pm}(\theta) = \sqrt{\frac{B \pm \sqrt{B^2 - 4AC}}{2C}}$$

The wave normal surfaces are then generated by parametrically plotting $u_{\pm}(\theta)\sin(\theta)$ versus $u_{\pm}(\theta)\cos(\theta)$. An example of a wave normal surface is shown in Figure 26.

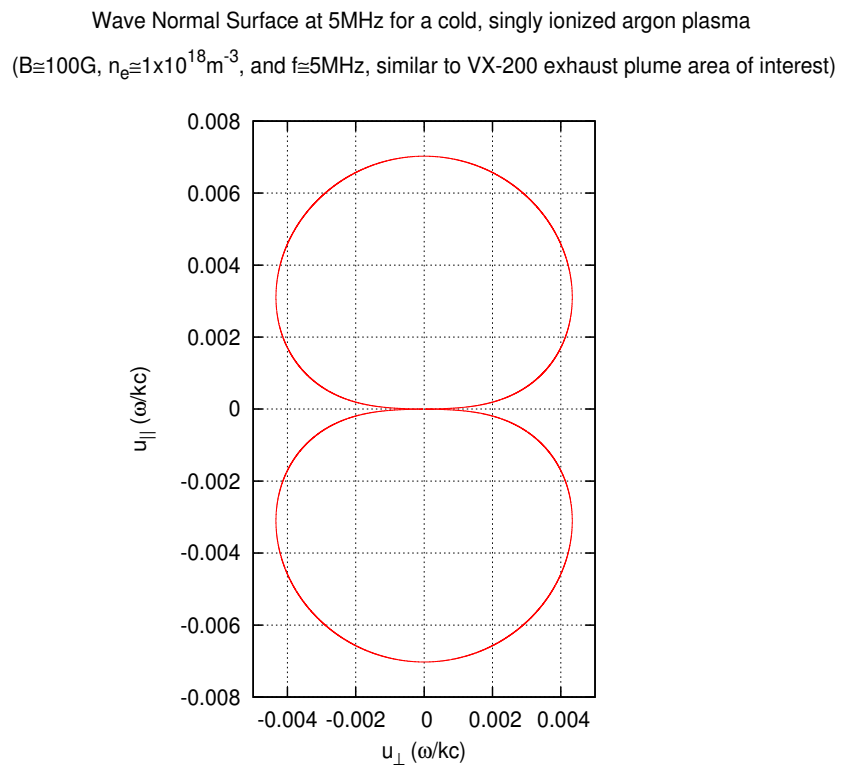

Figure 26 – Example of a wave normal surface plot. The wave normal surface shows the phase velocity of a cold-plasma wave mode in the direction parallel to the magnetic field (vertical on the plot), and perpendicular to the magnetic field (horizontal on the plot) These surfaces are generated for each region and then overlaid on the CMA diagram. The particular surface shown above corresponds to an Argon plasma in region 8b, using the Stix[13] numbering. This region corresponds to the spatial location of the VX-200 plume which has been discussed earlier in this chapter. Further discussion is provided in the following subsection.

An example of the plotting script used to generate the wave-normal-surfaces is provided in the appendices.

2. CMA diagram for Singly Ionized Argon

The previous subsection validated the cold plasma dispersion scripts by producing the well-known CMA diagram for a fictional plasma having an ion-to-electron mass ratio of 2.5. In this subsection, the validated techniques have been used to generate a CMA diagram for a singly-ionized Argon plasma.

Following the methods discussed in the previous subsection, the CMA diagram for Argon was easily generated by altering the mass ratio of the plasma. See Figure 27. The ion-to-electron mass ratio changes from 2.5 to $7x10^4$. Both axis scales have been changed to logarithmic so that all of the bounding surfaces can be displayed.

The region numbering of Stix[13] has been preserved in the Argon CMA. The WNS in each region of Figure 27 is reassuringly similar to that of Figure 24 and Figure 25. The scales of this figure were set to include Regions 8b, 11, and 13, which are more important for the analysis to follow. The wave modes and labels of Regions 2, 3, and 4 are not displayed, due to lack of space. The cyclotron and hybrid resonances are labeled, as before, so that one may reorient themselves in the new diagram.

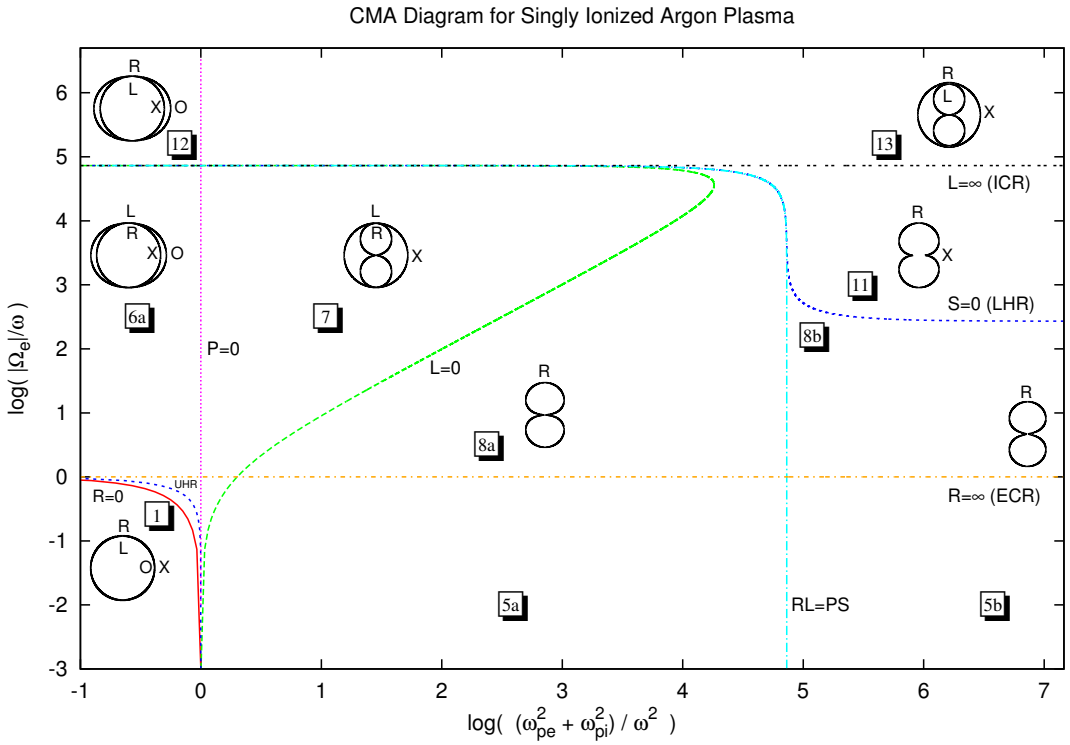

Figure 27 - CMA diagram for singly ionized Argon plasma. This figure is a re-calculated version of the diagram shown in Figure 24 and Figure 25. Note that both axes now have a logarithmic scale. Representative wave-normal-surfaces (WNS) are shown in each region. Comparing with Figure 24 and Figure 25, it is clear that each WNS has the same general shape. The WNS in regions 2, 3, and 4 have been omitted for clarity.

3. CMA with VX-200 Plume Scans

In the previous subsection, the CMA diagram for Argon plasma was presented and compared to the original. In this subsection, the Argon CMA diagram will be annotated with experimental data from the VX-200 plume (see Figure 28). The purpose of this exercise is to understand the fundamental wave modes that are possible in the plume, at various frequencies. Analysis will focus on the regions of the diagram which are applicable to the VX-200 plume conditions, at frequencies of interest.

To define a point on the CMA diagram, one must know the magnetic field strength, the plasma density, and the wave frequency. If an arbitrary frequency is chosen, the CMA diagram can be annotated with scans made by varying the density and field. Using the electron density and magnetic field measurements discussed in Subsection A.1, radial and axial scans of the plasma plume have been plotted on a CMA diagram in Figure 28. The scans are a hypothetical construct. They show the regions of the diagram in which certain frequencies of oscillation would reside, if such oscillations existed in the VX-200 plume. In other words, Figure 28 shows what the WNS would be for cold plasma waves at several frequencies of interest. These waves have not necessarily been observed. In fact, only the series for 5 MHz has been observed. The higher frequencies were studied in another work because they are important for communications with the International Space Station.[14] Nevertheless, the range of frequencies in Figure 28 gives some insight into where other, unshown oscillations would be on the diagram.

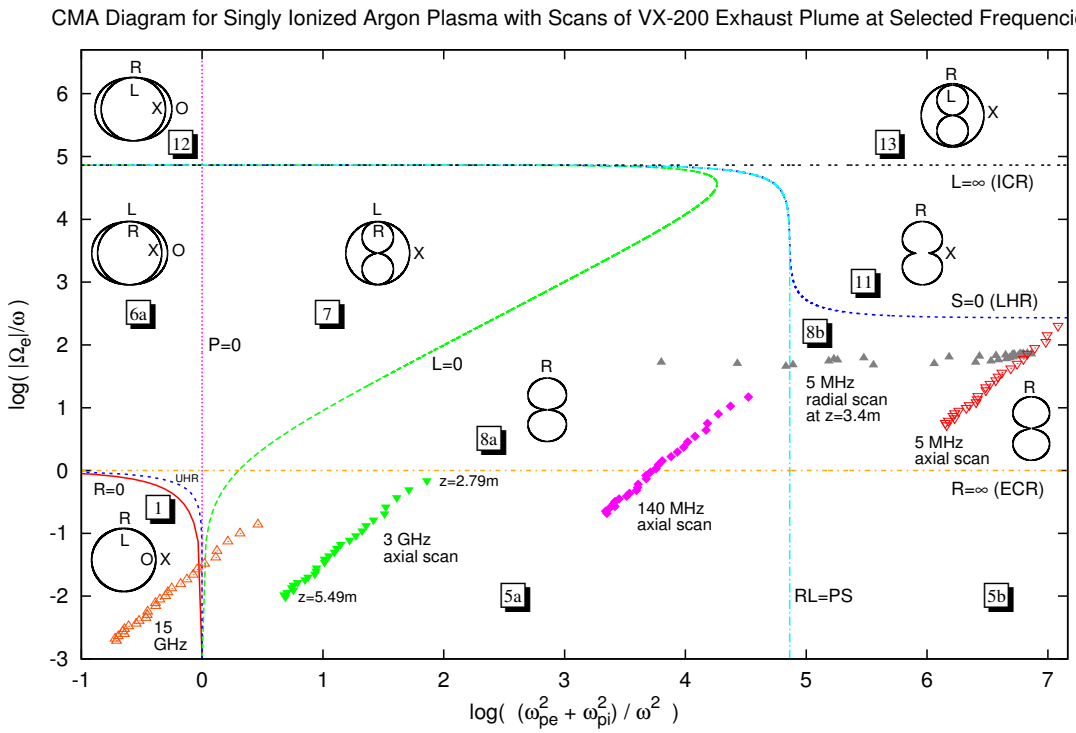

Figure 28 - CMA diagram showing axial and radial scans through the VX-200 plasma at several frequencies. Together with the WNS in the region, each data series shows the types of cold plasma waves which are possible, along a scan of the plume, at the selected frequency. The gray filled triangles, for example, represent a radial scan through the plume, at the axial location, and for one frequency, at which electric field oscillations were experimentally detected. This data series does not assert that the detected oscillations were purely a cold plasma wave. It merely states that, if a cold plasma wave did exist at this location and frequency, it would necessarily have the WNS of Region 8b: namely, that of the whistler wave. The higher frequency scans in red, green, and purple refer to frequencies which are important for communications on the International Space Station.[14] They are shown here to see the effect of varying frequency while keeping the density and magnetic field constant.

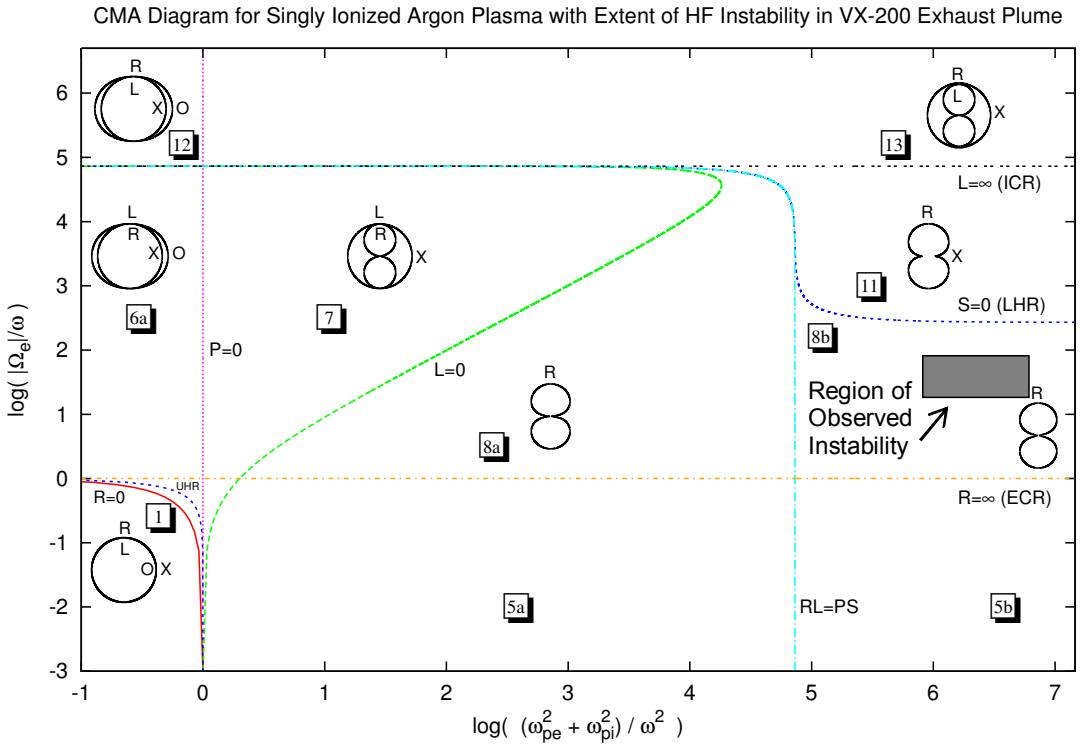

Figure 29 - CMA diagram with extent of observed HF instability in the VX-200 exhaust plume. The gray filled rectangle in region 8b shows the extent of the observed electric field oscillations, in the context of cold plasma dispersion. The corners of this rectangle are based on range of the observed frequencies and on the measured plasma densities and magnetic flux densities in the unstable area. Alternatively put, this figure shows the cold plasma wave mode corresponding to the unstable areas depicted in Figure 4. It is not asserted that the observed oscillations are purely of a cold plasma type. As previously discussed, the assumptions of cold plasma dispersion are not entirely valid in the area in question.

4. Tracking ICH Harmonics through the Plume

The previous subsection introduced Figure 28, which annotates the CMA diagram with some explicit combinations of frequency, density and magnetic field that are applicable to the VX-200 plasma exhaust. This subsection focuses on the 5 MHz oscillations in Region 8b (the rightmost axial and radial scans of Figure 28) which are

approximately the frequency of some of the observed oscillations in the VX-200 plume.

Oscillations were observed at several frequencies, all being high harmonics of the drive frequency of the ICH stage of the VX-200 rocket core. The first three sections of this chapter investigated the possibility that drift instabilities could amplify the ICH harmonics in this region of the plume. This subsection attempts to use the information in Figure 28 to investigate how the power from the ICH stage of the engine reaches the downstream plume where the instability is detected. Figure 5 on page 10 shows the location of the unstable region relative to the power source in the rocket core.

The ICH stage of the engine uses the ion cyclotron wave to add perpendicular energy to the ions in the rocket core.[12] The ion cyclotron wave mode can be seen as the inner WNS in region 13 of the CMA diagram. This mode may also be referred to as the slow wave, or the shear Alfvén wave. The outer surface in region 13 is the 'fast wave,' or the compressional Alfvén wave.[13] The ICH drive frequency, as well as its observed harmonics, presumably reside in Region 13 when they are excited in the rocket core. The observations of instability take place several meters downstream, where the density and magnetic field strength are smaller by several orders of magnitude. As one moves axially down the VX-200 plume, starting from the far right of Region 13, Figure 28 shows that the ion cyclotron wave will disappear at the ion cyclotron resonance. If ICH harmonics are to propagate as a cold plasma waves,

moving downstream from the source, from Region 13 eventually to Region 8b, they must convert to the fast wave at the ion cyclotron resonance, or be excited as fast waves from the onset. The latter case might partially explain why only the higher harmonics of the drive frequency propagate downstream form the core; the wavelength of the lower harmonics may be sufficiently large to prevent them from being excited within the diameter of the source region.

This subsection marks the conclusion of the section on cold, uniform, plasma dispersion analysis. An attempt has been made to use the information from the CMA diagram to understand how harmonics of the drive frequency propagate through the plume. Another possibility is that the detected waves are not purely cold plasma oscillations, but exist only as drift waves, depending on the strong density gradient that exists along the plume edge. The wave vector of the LHDI and the MTSI (discussed earlier in this chapter) is mostly parallel to the magnetic field, which would be consistent with propagation downstream through the plasma plume.

IV. DEVELOPMENT OF MAGENETIC NOZZLE PIC SIMULATION

Chapter II reviewed prior studies of VASIMR® exhaust plumes, some focusing on the detachment of the plasma from the magnetic field. Chapter III studied the stability of the VX-200 exhaust plasma in the context of an experimentally observed oscillation. This chapter introduces efforts to develop a simulation model that can augment such studies. Specifically, the following sections describe chronologically the development of a PIC simulation of a VASIMR®-like plasma plume in a magnetic nozzle. The next chapter will detail the culmination of this effort, which was the ability to simulate trans-Alfvénic plasma plumes and compare them to the laboratory measurements.

A. Review of PIC Method in Plasma Physics

This section lists some of the areas of plasma physics in which the PIC simulation technique has been utilized. The range of application of the PIC technique is broad, so, only some of the most cited publications will be described here. Emphasis is placed on the areas of research in magnetic nozzles and electric propulsion. In some instances, the general class (for example, 2d3v, electrostatic, axisymmetric, etc.) of the published PIC scheme is mentioned so that the work in this thesis may be seen in context.

In the field of electric propulsion research, some of the most sophisticated works of PIC simulation are those of Hall effect thruster (HET) plasmas. This

concentration is likely due to relatively widespread use of the HET in both the government and commercial space industries.[15] Adam, Heron, and Laval were the first to use a 2D PIC code to model the Hall Thruster ionization region, effectively simulating a turbulence-induced, cross-field electron transport.[16] Later, Heron and Adam used a similar code to study plasma-wall interactions.[17] Taccogna used the PIC method to simulate plasma flow in a Hall thruster acceleration region using geometrical scaling with a realistic ion mass and ε_0 in 2d3v,[18] and later studied azimuthal perturbations in 3d3v.[19] Azimuthal instabilities were also simulated in PIC by Hirakawa and Arakawa.[20] Szabo simulated the breathing mode in Hall thruster discharges using a 2d3v, r-z code with an artificial mass ratio and vacuum permittivity.[21] The breathing mode was also simulated in a θ, z code by Coche and Garrigues.[22] The numerous efforts using PIC in this field have reproduced experimentally observed phenomena and deepened the understanding of the plasma dynamics in Hall-effect thrusters.

PIC simulations of plasmas in magnetic nozzles are comparatively limited. A challenge in simulating a magnetic nozzle plasma is that, depending on the desired axial length of the domain, the plasma density may change by several orders of magnitude as it expands with the diverging magnetic field. The requirement that the grid size, Δ, be smaller than the Debye length, λ_D,[10] demands that a fine grid be used. On the other hand, modeling the downstream region requires a large number of simulation particles to ensure that each grid cell is sufficiently populated. The

simultaneous requirements of a fine grid with many simulation particles can quickly become computationally intractable.

One method of improving the computational cost of magnetic nozzle simulations is the variation of the grid size throughout the domain. Ebersohn has developed a quasi-one-dimensional (Q1D) magnetic nozzle simulation in which the cross-sectional area of the domain was varied with the size of an expanding magnetic flux tube.[23] The Q1D code was tested against XOOPIC in several verification tests. In the Q1D approach, however, it is necessary to assume that the plasma expands at the same rate as the magnetic field, eliminating the possibility of studying phenomena related to cross-field drifts. In an alternate approach, Luskow et al. have studied the use of non-equidistant grid cells in two dimensions for the simulation of thruster plumes.[24] In this approach, the grid size itself was allowed to vary across the domain; however, the use of a varying grid size presents problems with energy conservation in single particle test cases,[24] so care must be taken to ensure that such artificialities do not affect the validity of the simulation results.

B. Review of Previous Local Simulation Efforts

1. Summary of Corey Henderson's Work

This subsection describes efforts at the University of Houston that were preliminary to the work reported in this thesis. Corey Henderson began the development of a PIC simulation of a VASIMR® exhaust.[2] As reported in his

undergraduate thesis, Henderson used OOPIC Pro, which has the same physics algorithms as XOOPIC[25] (XOOPIC was used in this thesis).

At first, Henderson successfully created simulations of a plasma plume in a magnetic nozzle, but the simulations had an impractically low kinetic β, i.e., the simulated magnetic field was stronger than that of the experiment. Henderson used realistic masses of Hydrogen ions and electrons, as opposed to an artificial mass ratio. He also used realistic values for the other parameters of the simulation, e.g., plasma size and particle energies. When the field strength was weakened to achieve a $\beta \approx 1$, the simulation failed to achieve a stable particle population. The likely cause of this difficulty was that, by decreasing the magnetic field strength, the electron density at the simulation entrance increased. This caused the simulated Debye length to be too small compared to the grid size, which caused the more charge to build up at the entrance. The incoming particles were thus prevented from entering the simulation space. To avoid this charge-blocking, the ratio of the Debye Area to the simulation grid area needs to be kept larger than unity.[10]

$$\frac{{\lambda_D}^2}{\Delta z \Delta r} = \frac{\epsilon_0 m_e {v_{te}}^2}{2 n_e e^2 \Delta z \Delta r} > 1$$

The author encountered similar difficulties when initially trying to achieve a practical β in simulation. The solution was to scale the simulation parameters away from realistic values while holding constraints like the above ratio. This strategy is

discussed more in the section covering the author's simulation assumptions and constraints.

C. Development of Simulation Technique

The previous section described some work by Corey Henderson, another researcher who used PIC simulation to study magnetic nozzle plasmas. This section will describe the development of the author's own PIC simulation technique. The points in this section are made mostly in the context of the software that was used in this work, namely, XOOPIC. An effort has been made, however, to relate things to PIC simulation in general. The reference text primarily used during the development of the PIC simulation is the well-known book of Birdsall and Langdon.[10]

There were many challenges to creating a PIC simulation that could be useful for studying VASIMR® like exhaust plumes. Some of the mistakes made by Henderson were repeated, despite having read Henderson's thesis[2], because the mistakes had to be repeated to be understood. Early tests of simple simulations were encouraging. As the simulations were made more detailed, to more closely mimic the experimental plasma, the run-times became longer, and the wall-time cost of each trial-and-error grew. The situation was foretold by Birdsall and Langdon: "…one can do considerable simulation without understanding all or even part of simulation theory. But, we think (and come close to guaranteeing) that you will find need for the theory and its implications sooner than you may realize at first."[10] While the author's

quest to further understand PIC theory continues, the remainder of this thesis chronicles what modest accomplishments have been made thus far.

1. Simulation Boundary Conditions

This subsection describes efforts to find the boundary conditions that allowed for a PIC simulation which best approximated trans-Alfvénic plasma flow in a diverging magnetic nozzle. Because the geometry of the simulation was two-dimensional and cylindrical (r-z), the bottom of edge of the simulation space was the cylindrical axis. The remaining boundaries are classified as the particle entrance (on the bottom left), and the three boundaries of possible particle exit (left, up, right). See Figure 30 for a summary of the simulation geometry.

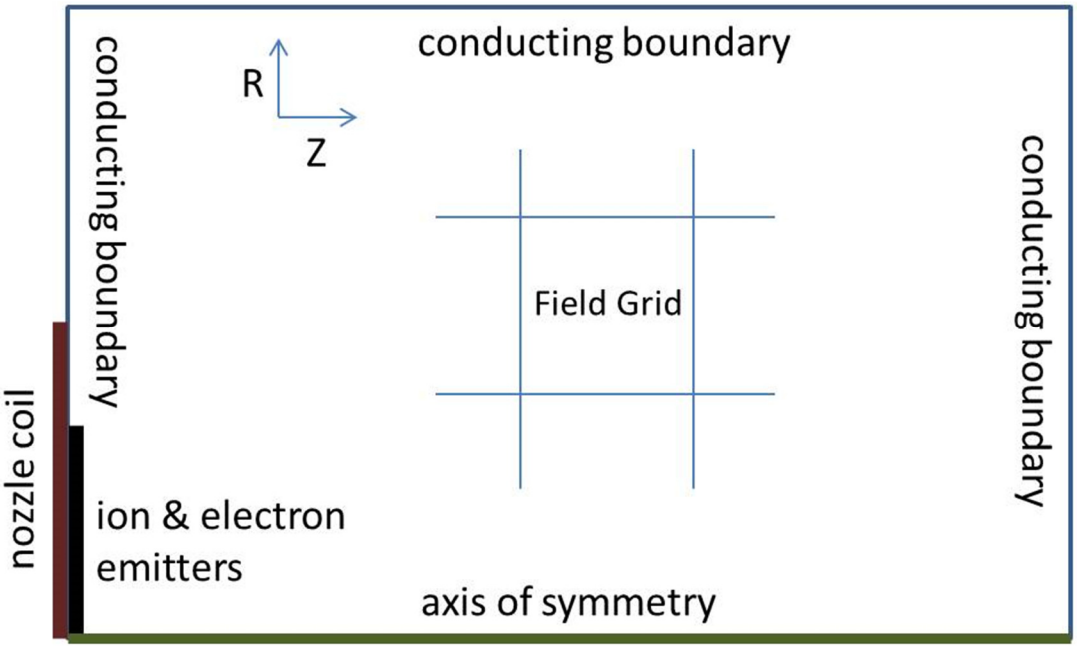

Figure 30 - PIC simulation geometry. Simulations were two-dimensional (r-z) and axisymmetric. The particles are axisymmetric rings of charge with two components of position, and three components of velocity (2d3v). Electric fields are solved at the grid points by solving Poisson's equation based on the charge in each grid cell. The particle velocities are updated by solving Newton's Second Law with the Lorentz Force, including the background magnetic field. Particle positions are updated using a leapfrog mover.

The simulation was designed to examine the behavior of the plasma in the magnetic nozzle, somewhat independently of the plasma source region. For the particle entrance, a separate beam emitter was used for ions and electrons. The class of emitters used is one which produces a uniform particle density in cylindrical geometry. These emitters also exhibit dielectric boundary conditions at the particle entrance plane.

XOOPIC also makes a provision for a plasma source region, instead of a particle entrance plane. These should be explored in a future work, as they allow for

user-defined spatial distributions of particle creation.[25] The work described here used only uniform distributions of ions and electrons in both position and velocity.

For the remaining simulation boundaries, conductors were used. Some attempts have been made to use dielectric boundaries, instead, following the suggestion of Birdsall and Langdon[10] for simulation of a plasma expanding to infinity. The dielectrics allow the charges that have left the domain to continue to affect the simulation, via the fields on the boundary; however, the dielectric boundaries led to artificial instabilities during some of the developmental simulations. Dielectrics were therefore abandoned, for the meantime. A future objective, beyond the scope if this dissertation, could be to reattempt the use of dielectrics.

An obvious question that arises from the use of conductors is whether this makes the simulations more faithful to a plasma jet in a conducting vacuum chamber, as opposed to the vacuum of space. This question has not yet been fully addressed. The use of conductors would seem to make the simulation more applicable the laboratory setup of a magnetic nozzle experiment; the vacuum chamber is normally made of a conducting metal; however, this strategy might require the entire chamber volume to be included in the simulation domain.

2. Background Magnetic Field

To simulate plasma in a magnetic nozzle, one must calculate the background magnetic field throughout the simulation region. To be as faithful to laboratory experiments as possible, the field due to simulated current loops of finite radii were calculated. The simulation space included grid points whose distance from the center of the current loop was several times less than the loop radius, as well as points which were many loop radii away. Because of this range of distances, integral approximations for the off-axis magnetic field, such as those from Chapter 5 of Jackson,[26] were not used. Instead the elliptic integrals,[27] which are expressions of the Biot-Savart Law and which fully describe the magnetic fields of a current loop, were evaluated numerically:

$$B_r = \frac{\mu_0 I R z}{4\pi} \int_0^{2\pi} \frac{\sin\theta \, d\theta}{(R^2 + r^2 + z^2 - 2Rr\sin\theta)^{3/2}}$$

$$B_z = \frac{\mu_0 I R}{4\pi} \int_0^{2\pi} \frac{(R - r\sin\theta) \, d\theta}{(R^2 + r^2 + z^2 - 2Rr\sin\theta)^{3/2}}$$

where R is the radius of the current loop, and r,z are the cylindrical coordinates of a position relative to the center of the current loop. The numerical approximation to these integrals was accomplished by a ten thousand-point Riemann sum evaluated at each grid point of the simulation space. The appendices include, on page 121, an example of the FORTAN program used for this purpose.

In early simulations, two simulated current loops were used to generate the background magnetic field. The loop radii and axial positions were arbitrarily set, very roughly approximating the dimensions of the VX-200 magnet coils. The current of each loop then had to be found, so that they would produce a simulated background magnetic field whose axial profile matched that of the laboratory VX-200 experiment. The currents of the two loops were found by solving the Jacobian of the axial field strength expressions. The currents were set so that the total axial field matched the experiment at the closest and furthest axial positions of the plasma diagnostics region, i.e., the extremes of the x-axis scale in Figure 31.

$$B_{z\,(total)} = B_{z\,(loop\ 1)} + B_{z\,(loop\ 2)}$$

$$B_{z\,(on-axis)} = \left(\frac{\mu_0 R^2}{2(z^2 + R^2)^{3/2}}\right) I = C(z)I$$

$$\begin{bmatrix} B_z(z_1) \\ B_z(z_2) \end{bmatrix} = \begin{bmatrix} C(z_1)_{loop\ 1} & C(z_1)_{loop\ 2} \\ C(z_2)_{loop\ 1} & C(z_2)_{loop\ 2} \end{bmatrix} \begin{bmatrix} I_{loop\ 1} \\ I_{loop\ 2} \end{bmatrix}$$

Given two values of z and their corresponding B_z from Figure 31, the above Jacobian was solved for $I_{loop\ 1}$ and $I_{loop\ 2}$. The resulting axial field profile is shown in Figure 32. The shape of the profile, between the endpoints, was compared qualitatively, similarity having been achieved by the rough approximation of the distance between the coils and the coil radii.

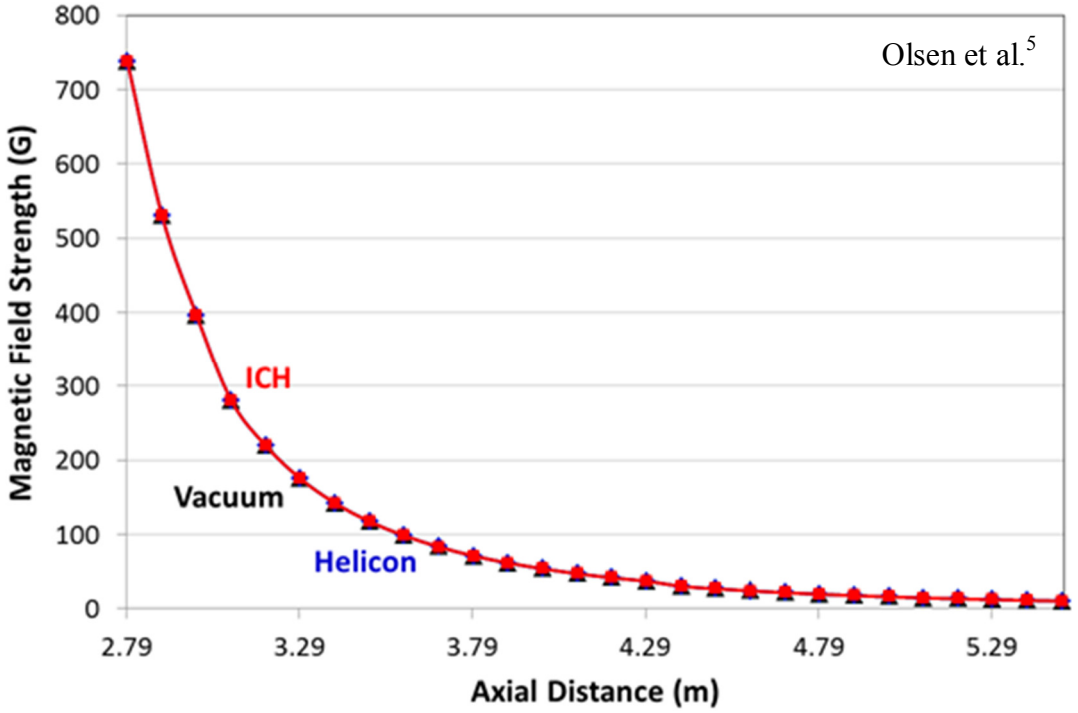

Figure 31 – On-Axis magnetic field versus axial distance of the VX-200 experiment, as reported by Olsen et al.[5] The axial profile of the experimental field was initially used as a model for a two-current loop simulation, whose field is shown in Figure 32. The zero of the x-axis is referenced to the upstream edge of the VX-200 support structure.

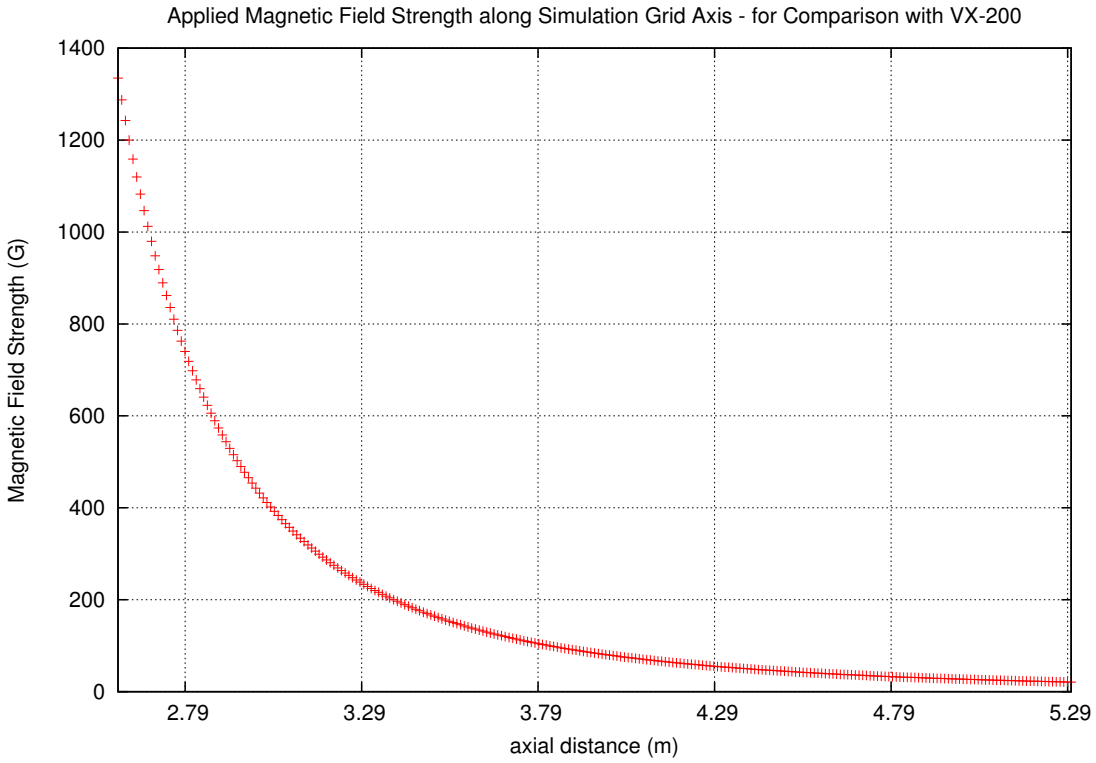

Figure 32 - Magnetic field versus axial distance from early PIC simulations. The field shown here is meant to mimic the experimentally measured field shown in Figure 31. Two simulated loops of current were used to generate this field profile. The distance between the loops, and the radius of the loops, were arbitrarily set; then, the current in each loop was found by solving a Jacobian matrix, forcing the field at the axial extremes to match that of the experiment.

The above method for mimicking the experimental magnetic field was successful and could be used in future simulations where fidelity to the measured field is important. During the final and most important simulation campaign of this work, however, a single current loop at the simulation boundary was used. This was done in hopes of making the simulation more generic and relatable to other magnetic nozzle studies.[28]

XOOPIC accepts background magnetic field configuration from a text file. Many initial simulations were done with an unintentionally weak magnetic field because the units were incorrect; XOOPIC expects the field in Gauss, but the field solver code provided Tesla. This error was discovered and corrected before the final simulation campaigns were embarked upon. At the time of its discovery, however, this error meant that the ratio of plasma pressure to magnetic pressure was even further from being simulating experiment than previously realized. This ratio and the difficulty in achieving it are further discussed in the next subsection.

3. Initial Simulations – Good Plume, Bad Beta

This subsection discusses some early simulation efforts and important lessons learned. Three simulation parameters were limited by the type of computer that was used to perform the simulation: the number of grid points, the number of simulation particles, and the time step. The combination of these settings determined the feasibility of a particular simulation run, i.e., whether it would complete in a reasonable amount of time.

Initially, simulations attempted to mimic the experimentally characterized plume of the VASIMR® VX-200 device. A realistic ratio of ion-to-electron mass was used. Ion and electron velocities in the simulations were based on experimental measurements made with Langmuir probes and retarding potential analyzers.[5, 12] The background magnetic field was tailored to match the field in the diagnostics region of the experimental device, as shown in the previous subsection. Regarding the ion

current and electron current, however, it was found that simulations were unstable unless the particle currents at the emitters were several orders of magnitude less than that of the experiment. An explanation of this restriction follows.

The particle currents and velocities were the parameters that determined the densities in the simulation. When attempting to simulate a plasma density like that of the VX-200, the simulation failed to develop a stable plasma flow. This difficulty is similar to one experience by Henderson.[2] The problem was that the simulation grid, which was just coarse enough to allow for run times on the order of 24 hours, was many times too coarse for the desired plasma density. Note that the simulation wall-time referred to here was typically achieved using a single core of an Intel Core2Duo U7300 processor paired with 4 GB of DDR3 memory. When the particle currents were sufficiently reduced to make the grid spacing several times smaller than the smallest Debye length, the simulations produced stable flows. The limit on grid size compared to density is clearly explained in Birdsall[10], and is discussed further in the section on final simulation constraints (see page 85).

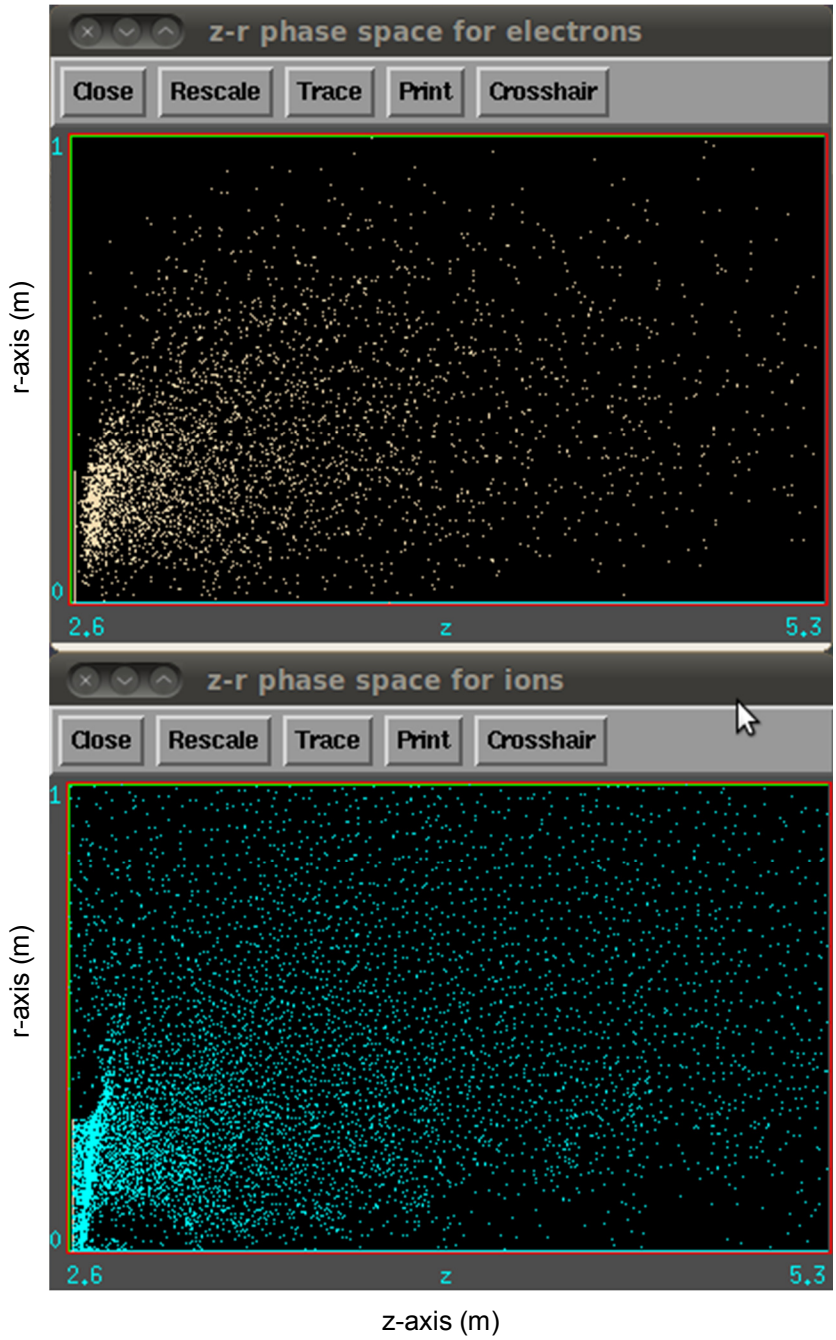

Figure 33 – Screenshot of output graphics of an early simulation showing instantaneous positions of ion and electron pseudo-particles. These plots show the difficulty encountered when the particle currents were increased in an attempt to mimic the actual VX-200 discharge currents. The grid spacing was too coarse for the attempted particle density, resulting in the bunching seen at the emitters in the lower left of each plot. In the next chapter, the naïve goal of simulating the experimental density is abandoned in favor of simulating the ion kinetic beta (β_{ki}), which is the ratio of the plasma kinetic pressure to the magnetic pressure.

The simulations of VX-200 at low density were helpful for learning how to operate the XOOPIC code, but they were of limited use from a research perspective. The plasma pressure was very low compared to the magnetic pressure, making for a very impractical experimental analog. Chapter V will discuss the process of implicitly scaling the density and the field to create plasmas which have an ion kinetic beta like that of the VX-200 experiment.

D. Campaign to Validate Code against other Simulations

The previous sections of this chapter discussed the beginnings of efforts to develop PIC simulations of magnetic nozzles using the XOOPIC code. Difficulties were encountered when attempting to simulate the density of the VX-200 exhaust plume, albeit with varying numbers of simulation particles. This section discusses a special simulation campaign which was undertaken to test the XOOPIC simulation model against the published results of another code, in a magnetic nozzle arrangement. The purpose of this exercise was to gain confidence in the XOOPIC functions used in the magnetic nozzle model. So, the XOOPIC code was configured to mimic the setup of two-fluid simulations by Merino et al.[28] The results of the XOOPIC simulation were then qualitatively compared to those of the two-fluid.

1. An Alternate Simulation Technique – Two Fluid

Ahedo and Merino developed a two-dimensional model of the expansion of a collisionless, electron-magnetized, low-beta, current-free plasma in a divergent

magnetic nozzle (DIMAGNO).[28, 29] In one study, this code was used to model the response of the ion population of a quasineutral plasma to varying degrees of magnetization at the plasma entrance plane, represented by the local ion gyrofrequency parameter:[28]

$$\widehat{\Omega}_{\mathrm{i0}}(z,r) = \frac{eRB(z,r)}{\sqrt{T_e m_i}}$$

This simulation used separate fluid equations for massless electrons with a uniform temperature and heavy, cold ions. A single nozzle coil at the entrance boundary created the magnetic field, with the coil radius set at 3.5 times the plasma radius. The ions and electrons were injected at the nozzle throat at the ion acoustic speed for cold ions:

$$v_{drift} = v_s = \sqrt{\frac{T_e}{m_i}}$$

Results were published for two separate field strengths, for gyrofrequency parameters: $\widehat{\Omega}_{\mathrm{i0}} = 1$ and $\widehat{\Omega}_{\mathrm{i0}} = 200$. Figure 34 is excerpted from the published work, and it shows the response of the ions to the field with $\widehat{\Omega}_{\mathrm{i0}} = 200$.

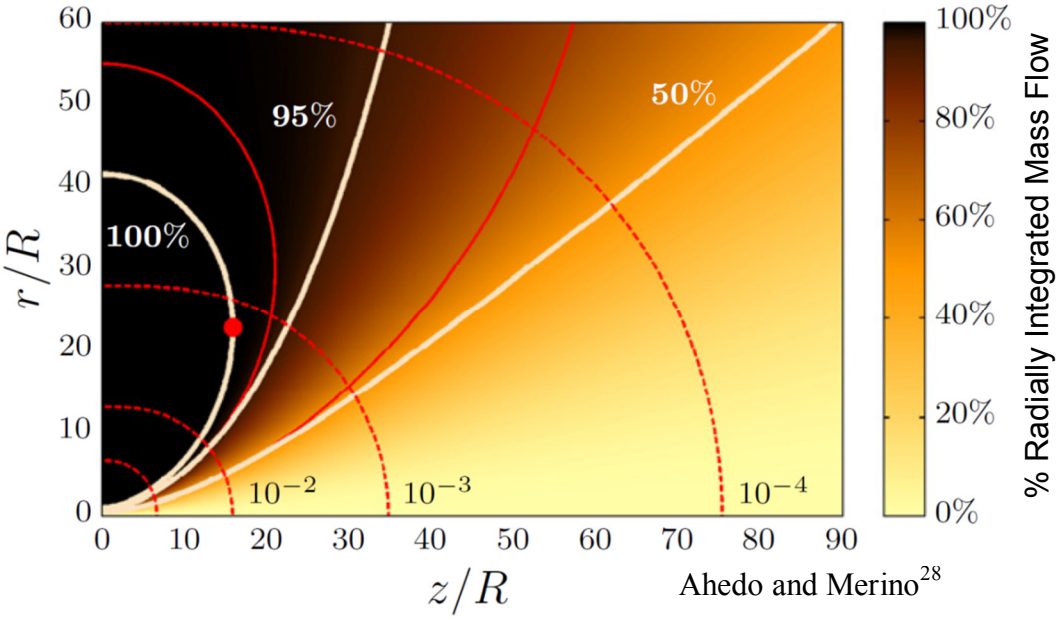

Figure 34 – Two-fluid magnetic nozzle simulation model. This figure is excerpted from a publication by Ahedo and Merino[28], which used a two-fluid simulation of plasma flow in a diverging magnetic nozzle. It is included for comparison with Figure 35, which was produced by XOOPIC with similar plasma conditions at the entrance plane. The thick, white lines show ion streamtubes referenced to the plasma entrance, while the solid, thin, red lines show corresponding magnetic stream tubes. The color bar shows the percentage of the radially integrated mass flow. The red dot show the magnetic nozzle turning point. Dashed red lines are logarithmic contours of B/B_0. This particular figure shows the ion flow relative to the magnetic field for an initial ion gyrofrequency parameter of $\widehat{\Omega}_i(z,r) = eRB(z,r)/\sqrt{T_e m_i} = 200$. In the publication, a similar figure was also displayed for $\widehat{\Omega}_i(z,r) = 1$.

2. Compare Ion Streamlines of Two-fluid to PIC

The previous subsection briefly summarized the results of a two-fluid simulation of a magnetic nozzle discharge by Ahedo and Merino. This subsection describes efforts to mimic the initial conditions of the fluid simulation, using XOOPIC, and to compare the results.

The main problem in designing an XOOPIC run to compare with Figure 34 lies in the extent of the simulation space. The fluid equations easily allow the simulation to cover many times the entrance diameter, while the particle code requires the user to obey limits in the number of particles per cell in the rarefied plume simultaneous with limits on the relationship between the Debye Length and the grid spacing. These two competing limits often necessitate the use of a non-uniform grid. This technique was not used here, however. The grid remained uniform, and the particle emitters were set to only two cells tall at the entrance. To ensure that the plasma entered the simulation space without impediment, the electron density at the emitter (n_{e0}) was limited to ensure that the Debye was at least ten grid cells. This was accomplished with the following relations, defined in the XOOPIC input file (in MKS units with temperatures in eV):

$$v_{drift} = \sqrt{\frac{T_e}{|e|m_i}}$$

$$n_{e0} = \frac{\varepsilon_0 T_e}{|e|\Delta r \Delta z}$$

$$I_e = \frac{|e| n_e v_{drift} \pi {R_{plasma}}^2}{10}$$

The electron temperature was set for a local ion gyrofrequency parameter of $\widehat{\Omega}_{i0} = 200$, which is within the range of values explored by Merino.[28] The ion current was limited to a fraction of the electron current so as to keep the simulation space globally neutral. This was necessary because the electrons remained magnetized, leaking out much faster than the ballistic ions.

The ions expanded into the vacuum and behaved similarly to the ions in the model two-fluid simulations. Figure 35 shows the z,r velocity vector of every tenth ion macroparticle in the XOOPIC simulation space, plotted at the particle position. This figure is meant to be compared to Figure 34. The comparison appeared to be good enough, so this application of XOOPIC was put on hold. Work on the final simulation campaign began thereafter. Future work should be devoted to comparing other aspects of the XOOPIC model to that of two-fluid and hybrid particle-fluid codes.

The process of recreating the two-fluid simulation forced the author to parameterize the XOOPIC input file, thereby allowing the simulation to be specified with fewer inputs. This programming technique was important for developing the trans-Alfvénic simulations discussed in the next chapter.

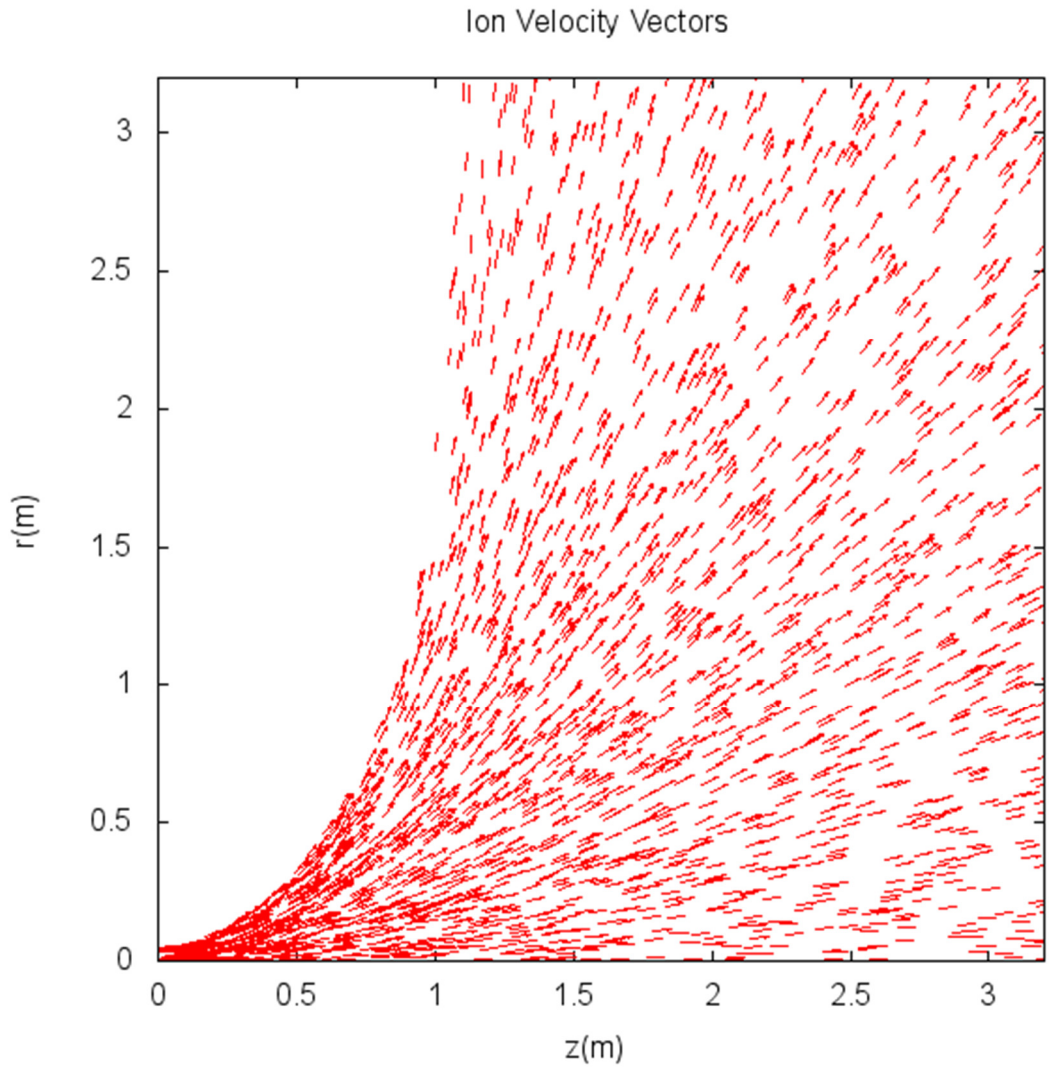

Figure 35 – Quiver plot of simulated ion axial and radial velocities. These data were generated during a campaign to compare XOOPIC behavior against the published results of a two-fluid model of a magnetic nozzle discharge. Azimuthal velocities are not shown. This XOOPIC plot is meant to be compared qualitatively with Figure 34. The normalized extent of the x- and y-axes is roughly the same for each figure. The initial plasma radius here is two grid cells tall at 0.05 m. The grid size is 128 by 128. For clarity, this figure shows only every 10th ion particle. The initial magnetization of the plasma in the XOOPIC simulation is slightly less than that of Figure 34, with $\widehat{\Omega}_i(z,r) = eRB(z,r)/\sqrt{T_e m_i} \cong 70$ instead of 200. However, the results of Merino show that the ion streamtubes should be relatively insensitive to this difference.[28] The general conclusion of this comparison is that the XOOPIC discharge is macroscopically consistent with that of this particular two-fluid scheme.

V. SIMULATION OF TRANS-ALFVÉNIC PLASMA

The previous chapter discussed some of the initial difficulties encountered during the development of a magnetic nozzle plasma simulation using the particle-in-cell code XOOPIC. This chapter describes a simulation campaign which overcame the previous challenges and produced a more satisfying result. The goal of this campaign was the simulation of a magnetic nozzle plasma which exhibits a super-Alfvénic transition, i.e., a plasma for which the β_{ki} transitions from less than one to greater than one. This work is the culmination of simulation efforts reported in this thesis.

The ratio of the plasma pressure to the magnetic pressure, β_k, is a fundamental property of plasma confinement devices, like fusion reactors, and of magnetoplasma propulsion devices, like VASIMR®, which creates jet of plasma that detaches from its magnetic confinement. To meaningfully simulate the dynamics of an accelerated plasma evolving through a magnetic nozzle, the β_k of the simulation was assumed to be of primary importance. The simulation was therefore designed to model the behavior of this parameter,

$$\beta_k = \frac{n_i m_i {v_i}^2}{\frac{B^2}{\mu_0}}$$

at the expense other parameters, such as the ratio of ion mass to electron mass, the ratio of the plasma frequency to the cyclotron frequency, or the ratio of the magnetic energy to the ion rest energy.

Using the constraints listed in this chapter, the simulation inputs were chosen to mimic the magnetization and kinetic beta of the VASIMR® VX-200 device. The ion kinetic beta of the simulation was then plotted to verify that the ions transition from being sub-Alfvénic to super-Alfvénic. The simulation beta was also compared to the experimental beta. Other properties of the simulated plasma are also discussed.

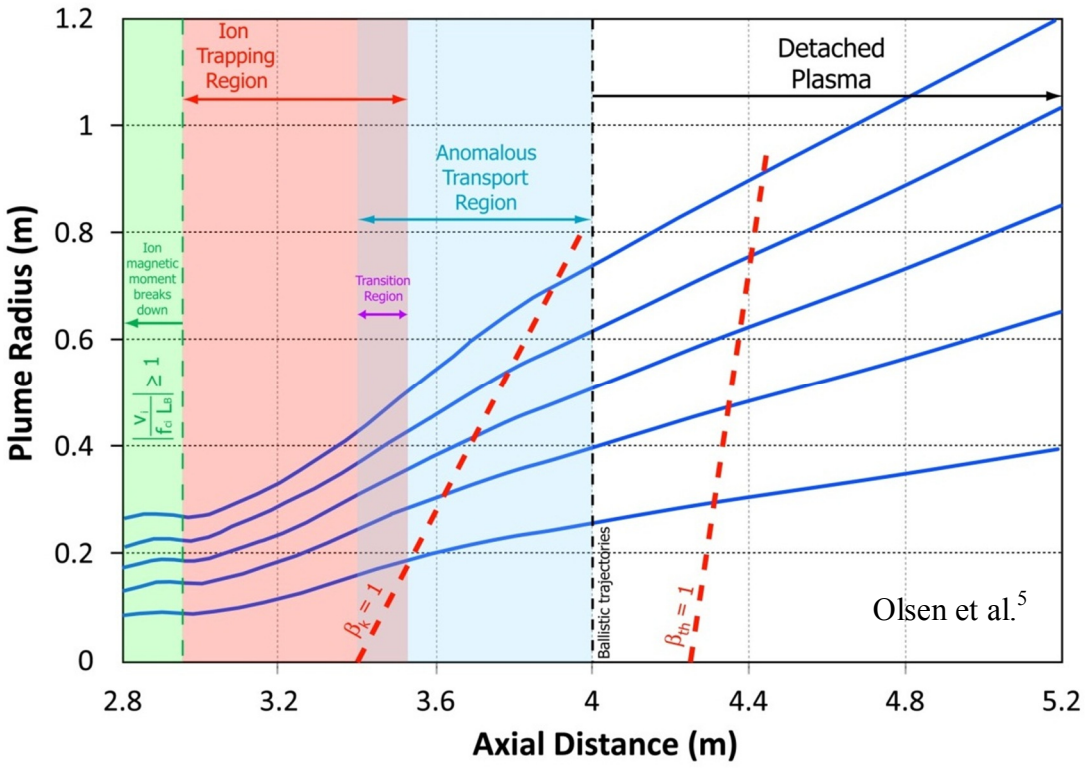

Figure 36 – Compiled application of detachment theory to the VX-200 plume. This graph is excerpted from Olsen et al.,[5] and shows an interpretation of the observations made during the plume detachment study reported therein. Dashed red lines show the super-Alfvénic transitions of the VX-200 plasma, as determined by measurements with a magnetometer, Langmuir probe, and RPA. The PIC simulations discussed in this chapter attempt to recreate the kinetic transition (β_k=1). β_k refers to the plasma beta associated with the drift velocity of the ions. β_{th} refers to the plasma beta due to the thermal velocity of the ions, i.e., the beta experienced in the rest frame of the ion jet. As Olsen points out, the kinetic transition appears to be roughly correlated in space with the detachment of the plasma from the magnetic field.

A. Simulation Assumptions and Constraints

Following the introductory discussion of the goal of the trans-Alfvénic simulation, this first section lists the assumptions and constraints used to set the parameters of the XOOPIC input file that dictated the simulation parameters. The constraints outlined here allowed the simulation inputs to be parameterized in such a way as to achieve the desired goals of the simulation while minimizing the number of trials and errors. The assumptions and artificialities of the simulation determine its applicability to the physical world. Note that the plasma properties in the next two sections refer to the values at the entrance of simulation grid, i.e., where the emitters inject the ions and electrons into the simulation.

1. Cylindrical Axisymmetry

The XOOPIC software used to perform the PIC simulations allows two-dimensional Cartesian or cylindrical (z-r) geometry. Cylindrical geometry was used, so the simulation space shown in Figure 37 is a cross-section of one half of the plasma plume expanding through the magnetic nozzle. The particles therefore represent axisymmetric rings of electrical charge, each with three components of velocity:

$$\overrightarrow{v_i} = \left(v_z\hat{z} + v_r\hat{r} + v_\varphi\hat{\varphi}\right)_i$$

where the subscript i refers to the ith particle of the simulation.

This assumption of course removes the possibility that the model will actually experience the LHDI or the MTSI, which are discussed in Chapter III. These

instabilities are flute-like in their geometry, as introduced by Krall and Liewer.[6] The main component of the wave vector is perpendicular to the magnetic field and the electric field. Since the fields are assumed to exist in the z-r plane, as shown in Figure 13 on page 22, the wave vector must therefore be mostly azimuthal. The XOOPIC models described in this work were not designed to capture azimuthal variations, and so cannot create an azimuthal wave. However, the z-r model can still be useful for simulating the conditions necessary for an azimuthal instability to develop.

2. Artificial Ion-to-Electron Mass Ratio

The XOOPIC software uses an explicit (i.e., time-resolved) particle mover, meaning that it must resolve both the plasma and cyclotron oscillations of the simulated ions and electrons. The time step of the simulation must therefore be chosen such that $\omega_{pe}\Delta t$ and $\omega_{ce}\Delta t$ are small. Otherwise, the particle dynamics would be subject to an artificial instability.[10] A competing interest on the time step is related to the number of computational steps necessary for the ion population (the heavier particles) to reach a steady state. The longer the time step, the shorter the wall time until the ion inputs and outputs reach equilibrium. For a given β_k, the velocity of the ions can be increased if the ion mass is simultaneously decreased; therefore, an artificially low ion-to-electron mass ratio of 100 was used for these simulations:

$$\frac{m_i}{m_e} = 100$$

For reference, the actual mass ratio for an Argon plasma is 7×10^4.

3. Single Nozzle Coil at Plasma Entrance

The background magnetic field for these simulations was calculated based on the field due to a single current loop at the particle entrance plane on the left side of the simulation space, similar to the geometry of Figure 30 on page 64. The radius of the current loop was chosen to be 1.5 times the radius of the particle emitters. Meanwhile, the radius of the simulation space was set to 3 times the emitter radius. The method of calculating the magnetic field due to the magnetic nozzle coil is described in subsection IV.C.0 above. This campaign, however, did not use multiple coils, so no attempt was made to mimic the axial field profile of the VX-200.

4. Model a Super-Alfvénic Transition

The kinetic beta at the simulation entrance was set to 0.1. Recall that β_k is the ratio of plasma energy to magnetic field energy.

$$\beta_{ki} = \frac{n_i m_i {v_i}^2}{\frac{B^2}{\mu_0}} = 0.1$$

This value was chosen to match the on-axis β_{ki} of the VX-200 plasma at the upstream limit of the plasma probes.

The desire to create XOOPIC inputs that model a specific value of β_{ki} necessitated a method by which the XOOPIC input file and the background magnetic field file could be generated programmatically. For this purpose, an additional FORTRAN program was created. FORTRAN had already been used to calculate the

magnetic fields and generate the background field files for previous XOOPIC campaigns. The new capability developed for this campaign was one by which various simulation parameters that are dependent on the magnetic field (e.g., the kinetic beta, β_{ki}) could be specified in a single input file. The XOOPIC input file and magnetic field file were then generated accordingly. The appendices of this work contain a sample of the FORTRAN code used to generate the XOOPIC inputs and the background field file.

5. Model a Realistic Magnetization

The ratio of the ion gyroradius to the plume radius at the entrance was set:

$$\delta = \frac{r_{gi}}{R} = \frac{m_i v_\perp^2}{eBR} \approx 0.1$$

Here, the plume radius, R, is just the physical extent of the simulated plasma plume at the entrance of the simulation grid. This ratio is thought to be important for keeping the simulation model somewhat connected to reality. For a given perpendicular energy, a δ much smaller than the laboratory experiment would imply an excessively strong magnetic field. This would be an impractical design because the magnet has a significant mass and requires significant electrical power to operate.

For this campaign, the ratio δ was planned to be set to 0.1, meaning that the average ion gyroradius would be one tenth of the plasma radius at the entrance plane of the simulation, which was also the magnetic nozzle throat. As will be discussed in the next section, the actual running of a simulation with the realistic magnetization has

yet to be accomplished. This should be an immediate objective of research following the completion of this dissertation.

6. Ensure Several Grid Cells in any Debye Area

The ratio of the square of the Debye length to the area of a simulation grid cell was fixed:

$$f = \frac{{\lambda_D}^2}{\Delta z \Delta r} = \frac{\epsilon_0 m_e {v_{te}}^2}{2 n_e e^2 \Delta z \Delta r} \approx 10$$

This ratio is required to be several times greater than unity; otherwise the simulated electrons will exhibit an artificial instability at the particle entrance, which is the region of highest density. This instability was a fundamental problem of earlier simulation attempts, which have been discussed in the previous chapter. For this campaign, the ratio f was set to 10, meaning that there were approximately 10 grid cells within the smallest Debye circle in the simulation. As Figure 37 and Figure 39 show, the ions and electrons were able to enter the simulation space without bunching at the entrance, which, in previous campaigns, had resulted from the density being too high.

B. Implicit Determination of Simulation Inputs

In the preceding section, several dimensionless ratios were defined with the intent of simplifying the creation of the XOOPIC input file. This section steps through the process by which free parameters were set, and the constraints applied to

arrive at numerical values for the various XOOPIC inputs. The calculations described below took place in the FORTRAN code described in subsection 4, above.

1. Emitter Parameters

The simultaneous constraints of β_{ki}, δ, and f were combined, yielding the following equation:

$$\frac{m_i {v_\perp}^2}{m_e {v_{te}}^2} = \frac{v_\parallel^2}{c^2}\frac{R^2}{\Delta z \Delta r}\frac{\delta^2}{2f\beta}$$

This equation was used to determine implicitly the velocities and currents of the ion and electron emitters in the simulation input file. Each particle species was injected by an emitter which requires three dimensions of drift velocity, three dimensions of thermal velocity, and the particle current.

The process of determining the emitter parameters can be summarized as follows. First, the thermal velocity of the electrons was calculated:

$$v_{te} = \frac{c}{\delta}\frac{\Delta z}{R}\frac{v_{i\varphi}}{v_{iz}}\sqrt{2f\beta_{ki}\frac{m_i}{m_e}}$$

$$\Delta z = \frac{L_z}{N_z} = \frac{2L_r}{256} = \frac{2(3R)}{256}$$

where β_{ki}, δ, f, and R are defined above. The v_{te} calculated above was used for the thermal velocity in all 3 dimensions. The ratio of the axial grid spacing to the initial plasma radius was determined by the number of grid cells and the ratio of the overall simulation axis to the radius. This campaign typically used a simulation space that

was twice as long in the z-direction as in the radius, with a grid size of 256 by 128 (N_z by N_r). The radial length of the simulation space, L_r, was set to three times the initial plasma radius, R. The radius of the single current loop producing the background magnetic field was set to 1.5 times the plasma radius.

The ratio of the ion azimuthal drift velocity to the axial drift velocity is related to the average pitch angle and the magnetization of the ions at the entrance. It is planned to set this velocity ratio at approximately 0.1 in future work. The simulations performed thus far have not injected ions with any azimuthal drift velocity.

With the electron thermal velocity determined, the axial ion drift speed was calculated as follows:

$$T_e(eV) = \frac{m_e}{|e|} {v_{te}}^2$$

$$v_{diz}\left(\frac{m}{s}\right) = \sqrt{\frac{T_e|e|}{m_i}\frac{E_{diz}}{T_e}} = v_{dez}$$

$$\frac{E_{diz}}{T_e} \approx 45$$

The ratio of the axial ion energy to the electron thermal energy is used in this calculation because it is a ratio which can be set using experimental measurements made in the VX-200 exhaust plume. The swept Langmuir probe measurements of electron temperature and retarding potential analyzer measurements of axial ion drift energy were used to find the above ratio. This setting makes the simulation more related to magnetic nozzle discharges whose ions have been heated significantly above

the electron temperature, e.g., the VX-200 exhaust plume. A future work might investigate the observable effects of varying this energy ratio in the simulation input.

The maximum allowable electron density at the plasma entrance was set by the ratio of the Debye area to the grid size, f:

$$n_e = n_i = \frac{\varepsilon_0 T_e}{|e|\Delta r \Delta z f}$$

Note that quasineutrality has been assumed at the entrance plane of the simulation. With the electron density in hand, the necessary magnetic field strength could be calculated from the expression for the kinetic beta:

$$B = v_{diz}\sqrt{\frac{\mu_0 m_i n_e}{\beta_{ki}}}$$

The value of the field strength at the nozzle throat, along with the chosen value of the magnetic coil radius, were passed from the main FORTRAN program to a separate FORTRAN module. The integral expressions for the magnetic field, described in IV.C.0 on page 62, were then computed and the corresponding text file generated.

The use of the z-component of the ion velocity in the preceding expression is inconsistent with the constraints placed on the initial ion pitch angle and magnetization of the plume. In practice, the simulations of this campaign only used an ion drift velocity in the z-direction. This inconsistency effectively lessened the total ion energy that was prescribed by the specified magnetization, δ (see subsection V.A.5). In future works, after this dissertation, it is intended that the azimuthal ion drift velocity will be calculated by the following:

$$v_{di\varphi} = \frac{eRB}{\mu_0 \delta}$$

Finally, the emitter currents were calculated such that the electron density at the plasma entrance was limited to the maximum density as specified above. The emitter currents were calculated as follows:

$$|I_e| = |I_i| = \pi R^2 |e| v_{diz} n_e$$

2. Simulation Time Step

XOOPIC can be configured to use an electrostatic or electromagnetic field solver. In electromagnetic mode, the full set of Maxwell's equations is solved on the grid, and the magnetic field changes, via Ampere's Law, in response to currents in the plasma. An electromagnetic field solve would conflict with the constraints of this simulation campaign because the implicitly determined azimuthal ion velocity was superluminal. This problem was partially a result of the choice of L_z , which is a free parameter and in terms of which the simulation velocities could be normalized. The ion velocities had to be high enough to achieve the desired β_{ki}, given the relatively coarse grid acheivable with the available computer resources. With a sufficiently high velocity, the density at the particle entrance can be limited to necessary fraction of the grid size while simultaneously achieving a high plasma kinetic pressure.

Because of the required ion velocities, an electrostatic field solve was used. In this mode, XOOPIC uses the charge density of the simulation particles to solve Gauss's Law for the electric field on the grid points:

$$\nabla \cdot \boldsymbol{E} = \frac{\rho}{\varepsilon_0}$$

Because the simulations were electrostatic, there was no need to restrict the simulation time step to satisfy the Courant condition with regards to the speed of light. The time step was, however, required to be a small fraction of the electron plasma oscillation period, as prescribed by Birdsall and Langdon.[10] For this campaign, the time step was set to one hundredth of the electron plasma period in the region of highest density:

$$\Delta t = \frac{2\pi}{100\omega_p} = \frac{2\pi}{100}\sqrt{\frac{\epsilon_0 m_e}{n_e e^2}}$$

where $n_e$is the expected electron density at the emitter, as implicitly determined in the previous section.

3. Number of Simulation Particles

Given the emitter currents and drift velocities determined above, the desired number of simulation particles, N_p, was set by adjusting the ratio of physical charged particles to computer particles. A successful method was to assume that the axial drift speed of the ions would be fairly constant over the axis, yielding the following equation for the necessary ratio of physical to computer particles:

$$N_{p2c} = \frac{I_i L_z}{|e| v_{diz} N_p}$$

Figure 38 shows the number of ion and electron simulation particles in the grid versus time for a typical simulation of this campaign. The target number of particles

was 10^5. The population record shows smooth growth, with the number of particles stabilizing within 10% of the target value, or both species.

4. Summary of Simulation Inputs

Table 1 - Summary of typical constraints and inputs used during the trans-Alfvénic simulation campaign.

Ratio of Ion Mass to Electron Mass	$\frac{m_i}{m_e}$	100
Kinetic Ion Beta (ratio of kinetic plasma pressure to magnetic pressure)	$\beta_{ki} = \frac{\mu_0 n_i m_i {v_{diz}}^2}{B^2}$	0.1
Ratio of Debye Area to Grid Cell Area	$f = \frac{{\lambda_D}^2}{\Delta z \Delta r} = \frac{\epsilon_0 m_e {v_{te}}^2}{2 n_e e^2 \Delta z \Delta r}$	10
Ratio of Axial Ion Drift Energy to Electron Thermal Energy	$\frac{E_{diz}}{T_e}$	45
Number of Grid Cells	$N_z \times N_r$	256 ×128
Ratio of Simulation Axis to Simulation Radius	$\frac{L_z}{L_r}$	2
Ratio of Simulation Radius to Plasma Radius	$\frac{L_r}{R}$	3
Ratio of Magnet Coil Radius to Plasma Radius	$\frac{R_{coil}}{R}$	1.5
Ratio of Time Step to Electron Plasma Period	$\frac{2\pi}{\omega_p}\Delta t$	0.01
Total Steps of Simulation	$N_{\Delta t}$	30,000
Number of simulation particles in each species	N_{ci}, N_{ce}	10^5
Number Ratio of Physical to Computer Particles	N_{p2c}	10^{10}
XOOPIC field solve setting	$ElectrostaticFlag$	4 – electrostatic /multigrid
Simulation Boundary Conditions		conducting boundaries

C. Assessment of Simulation Goals

The previous sections of this chapter discussed the methods by which XOOPIC simulation inputs were determined. This section presents some of the results obtained from the final simulation campaign and discusses their implications.

In general, the trans-Alfvénic simulations of the final campaign were more successful than previous efforts described in this work. Without any pre-loading, the particles proceed through the simulation space and develop a diverging exhaust plume with a steady population, as shown in Figure 37 and Figure 38. Figure 40 compares the β_{ki} of the simulation to that of that VX-200 experiment, as reported by Olsen.[1] Figure 41 examines a perpendicular electric field which naturally develops along the edge of the plasma, which is interesting because of its similarity to the notional field geometry drawn in Figure 13 on page 22, in the context of the LHDI stability analysis.

1. Stability of Plasma Flow and Particle Populations

The simulations performed during this campaign benefitted from the lessons learned during previous efforts. The method to programmatically generate a complete set of input files (see subsection V.A.4 above), once established, allowed for the simulation parameters to be adjusted more easily. The resulting simulations were generally free from the artificial instabilities encountered earlier. Compare Figure 37, below, to Figure 33, on page 72. Starting from an empty grid, the particles were able to enter the simulation space, each jet expanding through the magnetic nozzle.

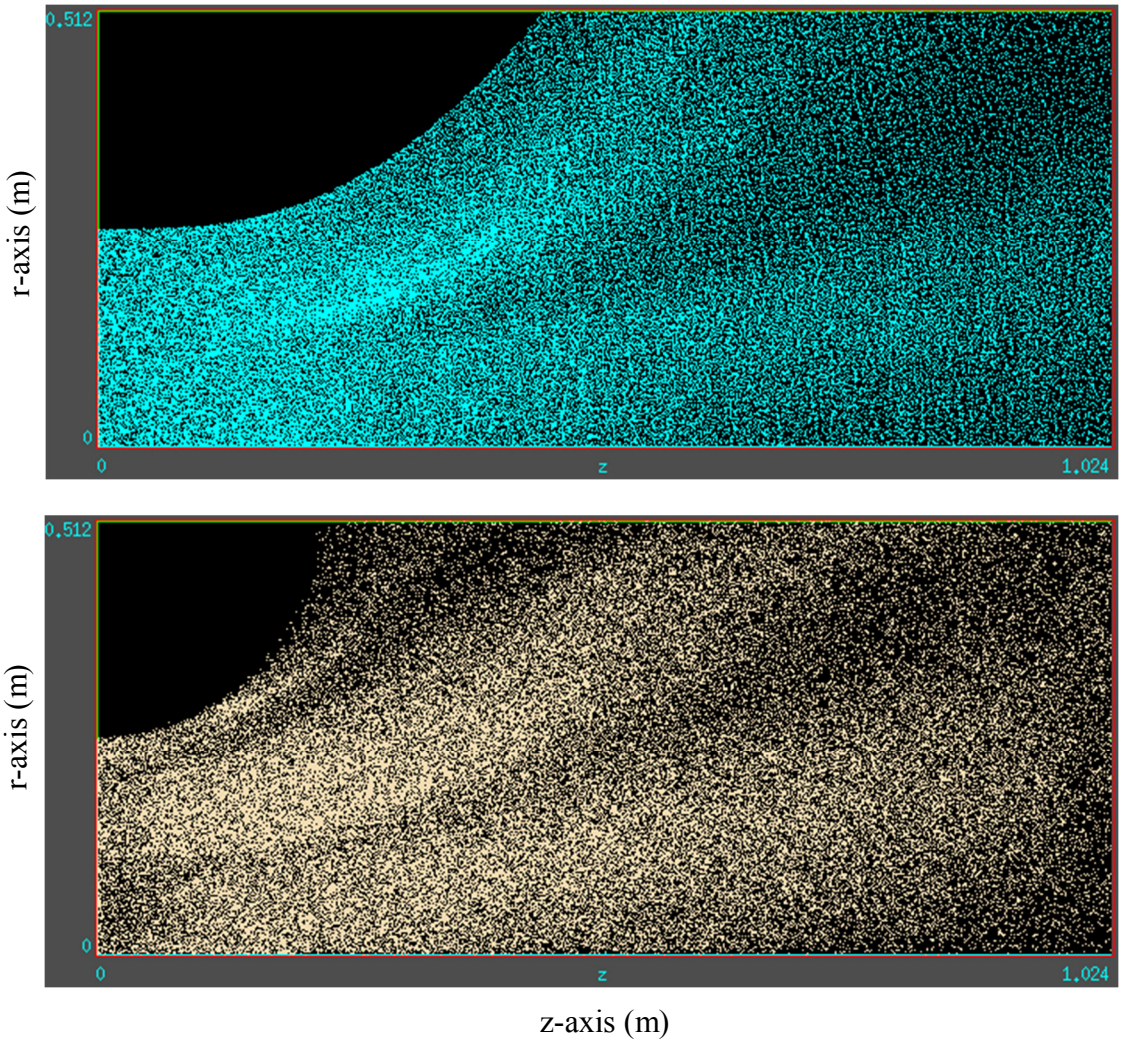

Figure 37 - Snapshots of ion (top) and electron (bottom) simulation particle positions during a typical run of the trans-Alfvénic campaign. The magnetic nozzle axis is horizontal and on the bottom edge of each plot. The z- and r-axis scales are in meters, but the particle velocities are normalized to the magnetic field strength. The normalization process is discussed further in subsections V.A.4 and 5. These plots were produced by the graphical user interface of the XOOPIC suite. Each point represents the z and r position of a simulation particle, which represents 10^{10} physical particles. For each particle, XOOPIC tracks two dimensions of position and three dimensions of velocity; therefore, each particle is an axisymmetric ring of charge and mass. There are approximately 10^5 simulation particles in each population shown above. Note that some of the electrons in the bottom plot appear to remain magnetized and are following the curve of the magnetic field, while the ions appear to be ballistic.

There is some interior structure in the ion and electron discharges, visible in Figure 37, but more so in Figure 39 and Figure 40. Some of the ions concentrate into a narrow jet, denser than the remainder of the discharge. The electrons seem to organize into 3 regions of higher density, with rarefaction in between. The reason for this organization is not clear. The particle velocities should be inspected to look for correlations with the density. Electrons have been shown, in a two-dimensional analytical model of Ahedo,[30] to stream backwards and cross magnetic field lines in regions of higher density. The electrons in preliminary XOOPIC simulations have been seen counterstreaming, but a rigorous study of this phenomenon has not yet been performed. It is conjectured that such motions could contribute to the regions of electron rarefaction seen in Figure 37.

As shown in Figure 38, the simulations were generally run until the populations of both species converged and reached a steady state. This was accomplished in approximately 30,000 computational steps with the inputs as summarized in Table 1.

Unlike some previous campaigns, there was no need to use a higher electron current to maintain the overall charge neutrality of the simulation. In fact, one can see in Figure 38 that the electron population (in white) is naturally pulled up by some slowly evolving process which seems to diminish as the two populations equalize. A slight instability in the number of electrons also grows and then diminishes. A conjecture is that slow growth of the population may be related to a physical process

by which magnetic nozzle discharges remain free of net current. The light electrons, which would otherwise remain mostly magnetized, must be forced to diffuse across, and detach from, the magnetic field lines. Presumably, the electron population in Figure 38 is slowly increased by something which moves the electron trajectories radially inward, thereby causing the electrons to remain in the simulation space longer and increasing the total number. Recall that the simulation space is twice as long, in the magnetic axis direction, as it is in the radial direction.

The cause of this slow trend in the number of model electrons should be investigated further to see if it is related to the inward detachment of electrons in physical systems, or if it is merely an artificiality of the simulation. A related suspicion is that the electron number growth could be related to the formation of the structure seen in the position phase space (Figure 37) and likewise in the density (Figure 39).

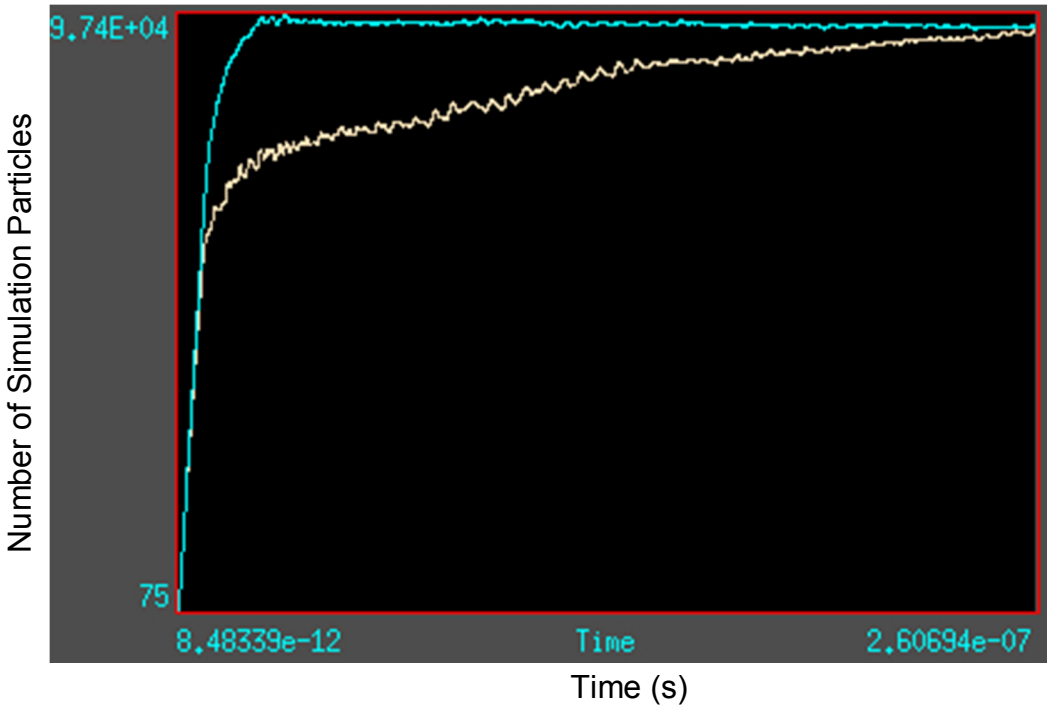

Figure 38 - Simulation particle populations (ions-blue, electrons-white) versus time (seconds) during a typical run of the trans-Alfvénic campaign. This figure shows that the plasma flow reaches a steady state and is globally quasineutral. The time axis shows the time step size, in seconds, on the left. The final time of the simulation, on the right, implies approximately $3x10^4$ time computational steps to reach this point of the simulation. The emitter currents were constant in time and equal among species for this simulation, i.e., the rate of particle generation was the same for ions and electrons. Note the gradual growth of the electron number to converge with that of the ions, and the slight ripple during the growth phase.

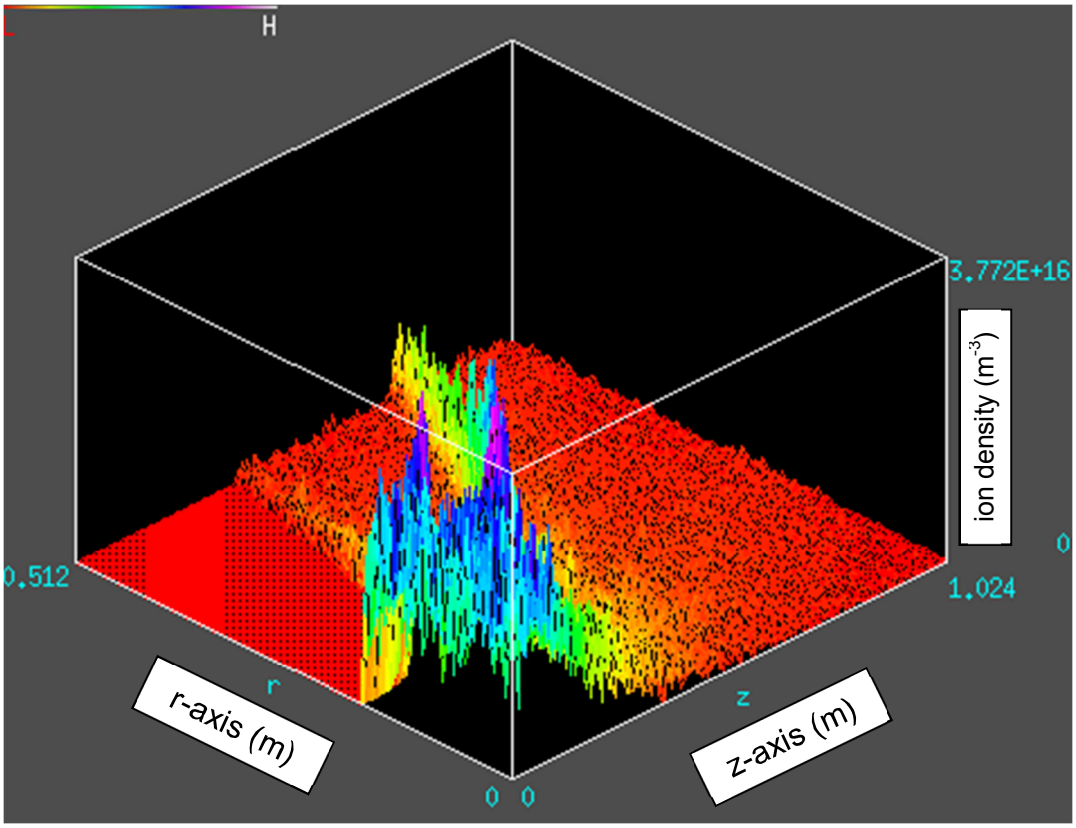

Figure 39 - Ion density map of a trans-Alfvénic simulation run. This plot shows the ion density variation in the z nd r dimensions after the ion and electron poulaitons have reached a steady state. The vertical axis units are m^{-3}, while the z- and r-axes are in meters. The density varies smoothly from the emitter port into the simulation space. Note also the partial concentration of the ions into a narrow jet extending roughly through the center of the plume.

2. Comparison of Kinetic Ion Beta of Simulation to Experiment

In the previous subsection, it was shown that the simulations of this campaign produced relatively stable plasma discharges which reached equal number populations of ions and electrons. Spatial and temporal features were seen in the development of the plasma flow, which warrant further investigation. This subsection assesses whether the simulation was successful in producing a trans-Alfvénic plasma jet.

Creating a magnetic nozzle plasma flow that transitions from $\beta_{ki} < 1$, to $\beta_{ki} > 1$, was a primary goal of this campaign. The motivation for this was a desire to reproduce the transition experienced by the experimental plasma of the VX-200, as depicted by Olsen in Figure 36.

The simulation was successful in creating a sub- to super-Alfvénic transition, albeit with significantly simplified settings for the input ion velocities. The ions have thus far been injected with only a z-direction velocity component, that which would make $\beta_{ki} = 0.1$ at the entrance. The magnetic field input file guaranteed that the magnetic field strength would decrease proportionally to z^{-2}, approximately. To achieve the transition, the simulation had only to produce an ion jet which was stable enough to maintain its velocity and not so divergent that the density spread too fast. The purely z-component velocity ions accomplished this much. Future simulations should include azimuthal velocities to better mimic the demagnetization of the ions as they transit the magnetic nozzle.

A comparison of the β_{ki} of the VX-200 plume to that of the XOOPIC simulation is shown in Figure 40 below. The experimental plot was made using ion velocities as measured by retarding potential analyzer, and electron density as measured by swept Langmuir probe, and magnetic field as measured by magnetometer.[1] The plot of the simulation used the densities and magnetic fields from the spatial grid and the average particle velocity within each grid cell. The two plots show that the simulation succeeded in recreating the extremes of the β_{ki} measurement.

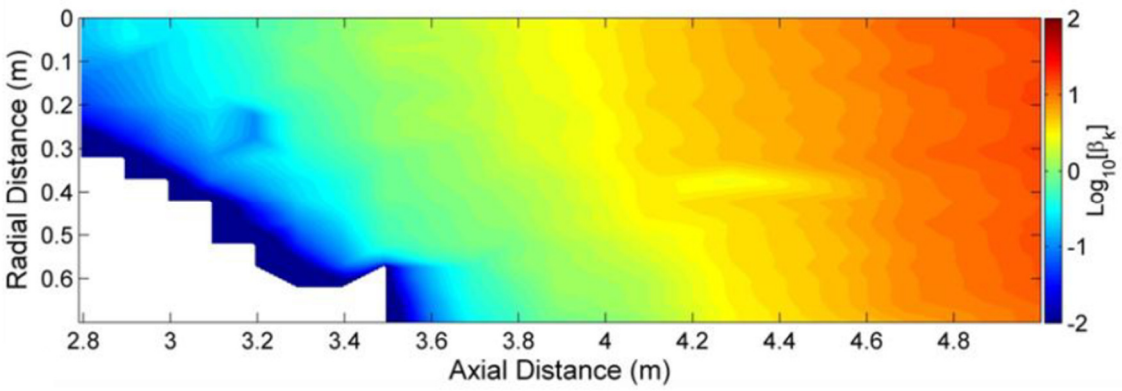

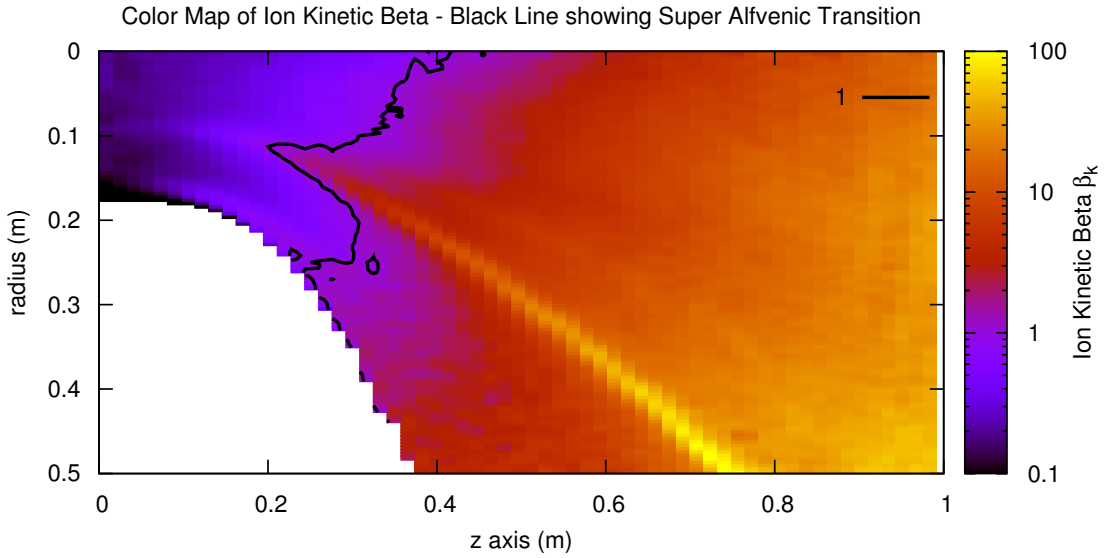

Figure 40 – Comparison of β_k of VX-200 experiment (top figure) to that of a XOOPIC trans-Alfvénic simulation (bottom figure). The top figure is excerpted from Olsen.[1] The black line in the bottom figure shows the super-Alfvénic transition, where $\beta_k = 1$. Recreation of the transition was a primary goal of the final simulation campaign. This result shows that the simulation model can accurately mimic the range of the ratio of plasma pressure to magnetic pressure that occurs in the VX-200 experiment; therfore, the model can be used to study particle-based phenomena that occur during the detachment process. A narrow region of higher ion density can be seen in the simulation. This phenomenon requires further study. The pixelation of the bottom figure reveals the spacing of the simulation grid cells. To calculate β_k, the particle velocities in each cell were averaged to make coherent data sets of velocity, density and magnetic field.

Distinctly visible in the bottom plot of Figure 40 is the narrow jet of higher ion density which occurred in the simulation, and which was discussed in the previous subsection. Further study of this jet is warranted. It should be noted that the ions are injected into the simulation with a flat radial density profile. The type of emitter used is one which attempts to make a uniform particle flux in the cylindrical geometry. The organization into the dense jet appears to happen gradually as the simulation develops. Future simulations could test whether the jet is affected by a change in the grid spacing, time step, or the number of simulation particles used. More interesting would be any affects due to the pitch angle of the injected ion velocity or inclusions of ion temperature.

3. Perpendicular Electric Field

Figure 41 shows a quiver plot of the electric field vector in a focused region of the plasma. An electric field develops perpendicular to the magnetic field along the edge of plasma in the simulation. This observation is interesting because of its potential applicability to the study of drift wave instabilities in the VX-200 plume. Recall the result from Chapter III, that the DC electric field, as calculated by spatially differencing the plasma potential, was probably insufficient to allow growth of the LHDI. The axisymmetric simulations performed in XOOPIC are not capable of modeling an azimuthal drift wave, like the LHDI, but they could model the axial and radial conditions necessary for such a wave. Future work should apply a stability

analysis to the simulation plasma to determine if the conditions are correct for the growth of the LHDI or the MTSI.

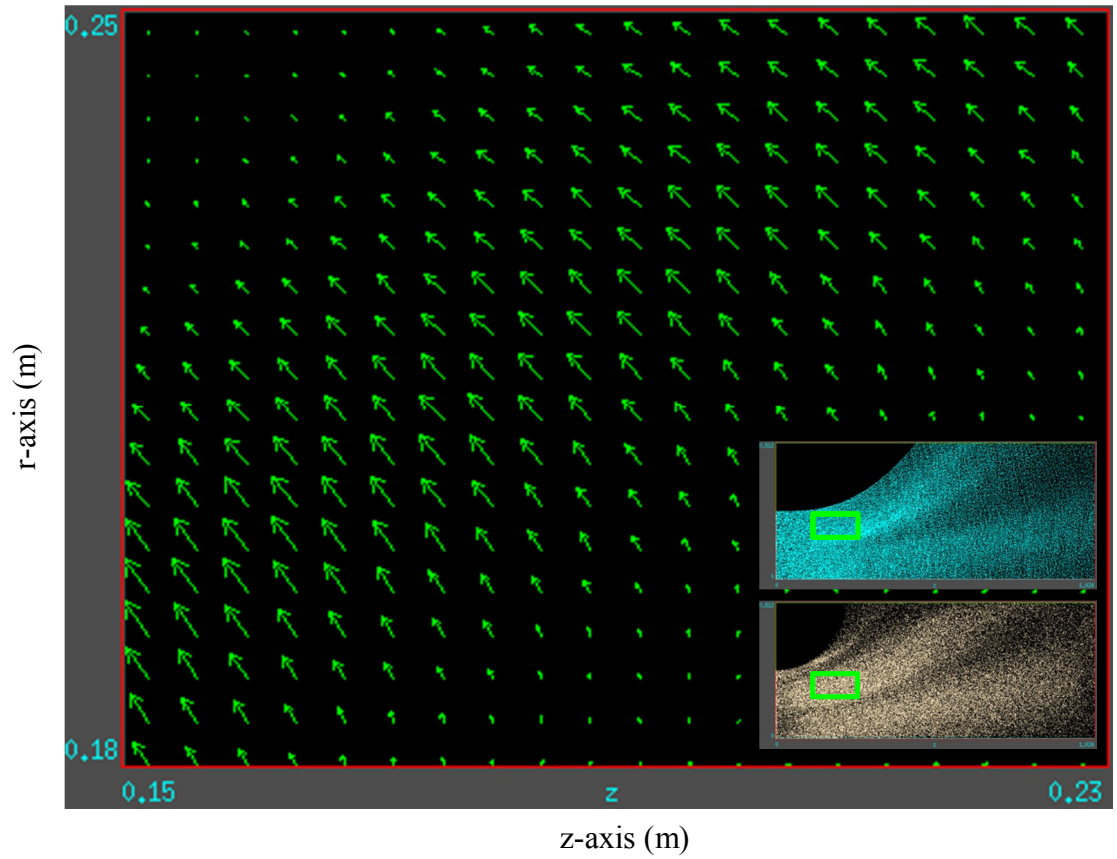

Figure 41 - Electric field vectors in a portion of the plasma plume during the trans-Alfvénic simulation campaign. The green squares in the insets show the portion of the plasma plume that is examined in this figure. The backgrounds of the insets are the screenshots of the ion and electron positions from Figure 37. The background magnetic field points approximately to the right and up. The large electric field vectors in the figure above are, therefore, perpendicular to the magnetic field. The physical applicability of this field requires further study. One possibility is that the electric field shown here is a manifestation of the concept introduced in Figure 13, i.e. an electric field caused by the charge separation that occurs as ions detach and electrons remain tied to the magnetic field. This would support the theory of azimuthal drift waves like the LHDI and the MTSI, which may be important for electron detachment in magnetic nozzles. Another explanaion could be that the perpendicular electric field is related to the filamentation of the ions shown in Figure 39.

VI. CONCLUSIONS AND OUTLOOK

The previous chapters presented the details of the work supporting this dissertation. This chapter will summarize the main conclusions of the dissertation and suggest objectives for future projects.

A. Drift Wave Instabilities and ICH Harmonics

Olsen observed oscillating electric fields in the VX-200 exhaust plume and investigated the effects they might have on the cross-field diffusion and detachment of electrons.[1, 5] The oscillation frequencies were close to the lower hybrid frequency and were therefore assumed to be a manifestation of the LHDI or the MTSI. Nils Brenning of the Alfvén Lab had suggested that these instabilities might be present in the magnetic nozzle. In fact, the electric field probe used for the HF measurements was built by Brenning's team. One objective of this dissertation was to further investigate the nature of the observed instability.

By interpolating the meticulous measurements made by Olsen et al. during an experimental investigation of the plasma plume, it was found that the conditions for the LHDI and the MTSI are not evident in the data; the DC electric field is not strong enough. This conclusion is based on the calculation of the electric field from shot-to shot measurements of the plasma potential. The conditions for instability growth were taken from the published work of Krall and Liewer, which is believed to be the original theory.[6]

Examination of the peaks in the electric field spectra, however, revealed that the oscillations were harmonics of the ICH drive frequency. Additionally, certain higher harmonics were significantly amplified. The most amplified harmonic was that which most closely matched the predicted frequency of the LHDI. It is conjectured that this coincidence supports the general theory that LHDI or the MTSI are present in the plasma, excited in part by the ICH power. This theory might be applied to an analytical model of the plasma plume, treating the ICH harmonics as perturbations.

B. Treatment of the VX-200 Plume as a Cold Plasma

The recognition of the ICH harmonics in the electric field spectra does not detract from the arguments made by Olsen that the oscillations could be contributing to the cross-field transport and detachment of the electrons. It merely adds to the understanding of the nature of the observed oscillations. New questions have been posed, however. What are the wave interactions, for instance, which enable certain high harmonics of the ICH frequency to be transmitted downstream and amplified along the edge of the plasma? The cold plasma dispersion analysis performed in section III.D was intended to be a first step toward an answer.

In Figure 28, an argon-plasma CMA diagram was generated, allowing the experimental conditions and observed frequencies to be compared to the basic cold plasma modes. This figure shows that the observed oscillations take place in region 8b, the domain of the whistler wave. In contrast, the ICH power is mostly delivered via the ion cyclotron wave in region 13. The argon CMA could be useful in

understanding this connection. It was, however, pointed out that the density gradient along the edge of the plume means that the CMA does not show the complete wave picture. Corrections must be made to the cold plasma dispersion to fully predict the stability.

C. Additional Laboratory Experiments

The VX-200 is no longer a functioning experiment. If a reasonable facsimile were available, however, further measurements could enhance the general picture of instabilities in propulsive magnetic nozzle plumes. To better understand the observed instabilities, the oscillating electric field should be measured in three spatial components instead of one. The probe circuitry and signal amplifier should be designed and calibrated for the frequency range in question, up to 10 MHz. Such measurements would help differentiate between the LHDI and MTSI and would also allow for higher confidence in estimating the effects they might have on the electron detachment process. The time dependent magnetic field might also be measured, thereby confirming the assumption that the observed instabilities are electrostatic in nature.

Additional DC measurements could be made as well. The plasma potential and electron temperatures could be measured with probes using RF compensation. Such measurements would enable a more accurate assessment of the theoretical conditions necessary for the LHDI and the MTSI, as carried out in sections III.A and III.B.

D. Particle Simulations of Magnetic Nozzles

Several computational tools were developed to support the PIC model of a magnetic nozzle. This work was the most time-consuming of all the efforts reported here, but this aspect of the dissertation has the broadest applicability. It was shown that two-dimensional PIC simulations of a trans-Alfvénic plasma can be executed quickly, with modest computational resources; most of the runs used a single core of an Intel Core2Duo U7300 processor paired with 4 GB of DDR3 memory.

The simulations achieve a stable plasma jet with particle dynamics that may be useful in understanding the electron detachment processes in physical systems. There is a great deal of additional work to be done on this front. The simulations reported in this dissertation are merely the first successful applications, to the magnetic nozzle plasma, of a versatile tool.

One objective is to simulate the effect of the observed VX-200 plume instabilities on the simulation plasma by artificially oscillating the electric field in the region of interest. One could then determine the amplitude of oscillation which is necessary to significantly affect the diffusion of electrons across the magnetic field. Eventually, the PIC model should be extended to include three dimensions of space, thereby enabling simulation of azimuthal fluting, which is assumed to occur with the theorized drift waves.

VII. APPENDIX A – CMA DIAGRAM GENERATION SCRIPT

This appendix contains a representative example of the script used to generate a CMA diagrams in Gnuplot© Version 4.6.

Table 2 – Example of a Gnuplot© script used to generate the CMA diagrams shown in Figure 25 on page 47.

```
reset; unset multiplot
set term postscript portrait enhanced color
set output "CMAWNS_2.5.eps"
set multiplot
set title "CMA Diagram for (m_i/m_e) = 2.5"
set xlabel "({/Symbol w}@^2_{pe} + {/Symbol w}@^2_{pi}) /
{/Symbol w}^2"
set ylabel "|{/Symbol W}_e|/{/Symbol w}"
mu=2.5;muinv=1/mu #73000 is the mass ratio for singly ionized
argon
set parametric
#set logscale x; set logscale y
#set format x "%T"; set format y "%T"
unset mxtics; unset mytics
set samples 2e6
xmin=0; xmax=2.1
ymin=0; ymax=3.4
tmin=ymin; tmax=(mu)
set xrange [xmin:xmax]; set yrange [ymin:ymax]; set trange
[tmin:tmax]
unset key #set key at graph 0.4,0.9
#set origin 0.15,0.15; set size ratio -1
set bmargin at screen 0.1
set lmargin at screen 0.18
set rmargin at screen 0.9
set tmargin at screen 0.9

set label "R=0" at 0.18,0.7
set label "L=0" at 1.17,0.3
set label "S=0 (LHR)" at 1.5,2.1
set label "S=0 (UHR)" at 0.3,0.93
set label "P=0" at 1.05,2.9
set label "RL=PS" at 1.3,1.26
set label "R={/Symbol \245} (ECR)" at 1.6,1.05
set label "L={/Symbol \245} (ICR)" at 1.6,2.55
set label "{/Symbol w} = |{/Symbol W}_e|" at -0.5,1.0
set label "{/Symbol w} = {/Symbol W}_i" at -0.5,2.5
```

```
set label "Ion Cyclotron Wave" font 'Helvetica,9' at 1.62,2.87
set arrow 1 from 1.62,2.9 to 1.52,3.02

#Region 1
set label 'R' font 'Helvetica,9' at 0.42, 0.57
set label 'L' font 'Helvetica,9' at 0.43, 0.47
set label 'O' font 'Helvetica,9' at 0.46, 0.45
set label 'X' font 'Helvetica,9' at 0.54, 0.45
#Region 2
set label 'L' font 'Helvetica,9' at 0.62, 0.62
set label 'O' font 'Helvetica,9' at 0.71, 0.54
#Region 3
set label 'L' font 'Helvetica,9' at 0.79, 0.92
set label 'X' font 'Helvetica,9' at 0.86, 0.80
set label 'O' font 'Helvetica,9' at 0.92, 0.80
#Region 4
set label 'L' font 'Helvetica,9' at 1.07, 0.92
set label 'X' font 'Helvetica,9' at 1.15, 0.80
#Region 6a
set label 'L' font 'Helvetica,9' at 0.49, 1.67
set label 'R' font 'Helvetica,9' at 0.49, 1.53
set label 'X' font 'Helvetica,9' at 0.56, 1.50
set label 'O' font 'Helvetica,9' at 0.66, 1.50
#Region 6b
set label 'L' font 'Helvetica,8' at 0.17, 2.30
set label 'R' font 'Helvetica,8' at 0.17, 2.21
set label 'O' font 'Helvetica,8' at 0.21, 2.20
set label 'X' font 'Helvetica,8' at 0.27, 2.20
#Region 7
set label 'L' font 'Helvetica,8' at 1.04, 1.27
set label 'R' font 'Helvetica,8' at 1.04, 1.20
set label 'X' font 'Helvetica,9' at 1.15, 1.15
#Region 8a - Whistler (Helicon) Waves (Compressional Alfven
Waves)
set label 'R' font 'Helvetica,9' at 1.23, 1.21
#Region 8b - Whistler (Helicon) Waves (Compressional Alfven
Waves)
set label 'R' font 'Helvetica,9' at 1.68, 1.54
#Region 9
set label 'R' font 'Helvetica,8' at 0.81, 2.18
set label 'O' font 'Helvetica,8' at 0.96, 2.10
#Region 10
set label 'R' font 'Helvetica,8' at 0.81, 2.46
set label 'X' font 'Helvetica,8' at 0.89, 2.37
set label 'O' font 'Helvetica,8' at 0.96, 2.37
#Region 11
set label 'R' font 'Helvetica,8' at 1.38, 2.41
set label 'X' font 'Helvetica,8' at 1.46, 2.30
#Region 12
```

```
set label 'R' font 'Helvetica,8' at 0.48, 3.12
set label 'L' font 'Helvetica,8' at 0.49, 3.03
set label 'X' font 'Helvetica,8' at 0.52, 3.00
set label 'O' font 'Helvetica,8' at 0.65, 3.00
#Region 13 - Ion Cyclotron Waves (Shear Alven Waves)
set label 'R' font 'Helvetica,8' at 1.48, 3.12
set label 'X' font 'Helvetica,8' at 1.59, 3.00

#set label "Note: B is vertical for \nwave normal surface
plots" font 'Helvetica,11' at 10**(3),10**(-2)
#set label 'Note: {/Symbol \255}B' font 'Helvetica,12' at
10**(6.2),10**(-2.5)

mylabels= "1    2    3    4    5a   5b   6a   6b   7    8a   8b
9    10   11   12   13"
xlabels=  "0.60 0.75 0.85 1.07 1.45 1.95 0.75 0.35 1.11 1.30
1.90 0.57 0.57 1.15 0.70 1.20"
ylabels=  "0.25 0.42 0.60 0.50 0.25 0.25 1.20 2.07 1.03 1.08
1.30 2.20 2.40 2.30 2.70 2.70"
do for [i=1:words(mylabels)] {
xoff = (0.015*(strlen(word(mylabels,i))-2))-0.015
set label "{/ZapfDingbats=28 \157}" at
((word(xlabels,i))+xoff),((word(ylabels,i))-0.005)
set label (word(mylabels,i)) at
(word(xlabels,i)),(word(ylabels,i)) font "Times-Roman,12"
}

#set label '15 GHz' at 10**(-0.8),10**(-3)
#set label "5.5 MHz \nradial scan \nat z=3.4m" at
10**(5.0),10**(1.4)
#set label "3 GHz \naxial scan" at 10**(1.5),10**(-1.1)
#set label '140 MHz' at 10**(3.6),10**(-0.6)

freq1 = 2*pi*15e9
freq2 = 2*pi*5.5e6
freq3 = 2*pi*3e9
freq4 = 2*pi*140e6
me = 9.11e-31
ec = 1.6e-19
eps = 8.854e-12

offset_factor=10**(0.35) #for the "z=" labels

plot\
(1+muinv*t)*(1-t),t title "R=0" lw 2,\
(1-muinv*t)*(1+t),t title "L=0" lw 2,\
2/(1/((1+muinv*t)*(1-t))+1/((1-muinv*t)*(1+t))),t title "S=0"
lw 2,\
1,10*t title "P=0" lw 2,\
```

```
muinv+(1/muinv)-1-(muinv*t**2),t title "RL=PS" lw 2,\
1e4*(t-tmin),1 title "R={/Symbol \245}" lw 2 lc rgbcolor
"orange",\
1e4*(t-tmin),(1/muinv) lw 2 title "L={/Symbol \245}"#,\
#\
#'axis.txt' u
(($6*ec**2)/(me*eps*freq1**2)):(($3*ec)/(1e4*me*freq1)) title
'15 GHz axial scan',\
#'339.txt' u
(($6*ec**2)/(me*eps*freq2**2)):(($3*ec)/(1e4*me*freq2)) every
::7 title '5 MHz radial scan at z=3.39m',\
#'axis.txt' u
(($6*ec**2)/(me*eps*freq3**2)):(($3*ec)/(1e4*me*freq3)) title
'3 GHz axial scan',\
#'axis.txt' u
((($6*ec**2)/(me*eps*freq3**2))*offset_factor):(($3*ec)/(1e4*me
*freq3)):(sprintf("z=%3.2fm",$1))\
# every 27::0 with labels font 'Helvetica,10' notitle,\
#'axis.txt' u
(($6*ec**2)/(me*eps*freq4**2)):(($3*ec)/(1e4*me*freq4)) title
'3 GHz axial scan'

unset border; unset xtics; unset ytics; unset xlabel; unset
ylabel; unset title; unset label
set parametric; set samples 2e5; set trange [0:2*pi]

#Stix Regions    1          2     3     4     6a    6b    7     8a
     8b    9     10    11    12    13
xwns=       "0.45 0.65  0.8   1.08  0.5   0.2   1.08  1.25  1.7
     0.83  0.83  1.4   0.5   1.5"
ywns=       "0.45 0.55  0.8   0.80  1.5   2.2   1.15  1.1   1.4   2.1
     2.37  2.3   3.0   3.0"
scaleup=    "0.05 0.03  0.05  0.03  0.1   0.05  0.20  0.25  0.20
     0.05  0.10  0.1   0.1   0.1"
scaleum=    "0.05 0.03  0.05  0.03  0.1   0.05  0.025 0.025 0.025
     0.05  0.05  0.1   0.08  0.1"

do for [i=1:words(xwns)] {

gb2mp1 = (word(xwns,i))     #gb2mp1 = 10**(word(xwns,i))
mubeta = (word(ywns,i))          #mubeta = 10**(word(ywns,i))
scaleupi = (word(scaleup,i))
scaleumi = (word(scaleum,i))

beta = mubeta/mu
gb2 = gb2mp1/(mu+1)

R = 1 - gb2/(beta+1) + gb2/(beta-muinv)
L = 1 + gb2/(beta-1) - gb2/(beta+muinv)
```

```
P = 1 - gb2 - mu*gb2
S = (R+L)/2.

A(t) = S*(sin(t)**2) + P*(cos(t)**2)
B(t) = R*L*(sin(t))**2 + P*S*(1 + (cos(t)**2))
C = P*R*L

up(t) = sqrt((B(t) + sqrt(B(t)**2 - 4*A(t)*C))/(2*C))
um(t) = sqrt((B(t) - sqrt(B(t)**2 - 4*A(t)*C))/(2*C))

plot up(t)*sin(t)*scaleupi+gb2mp1,up(t)*cos(t)*scaleupi+mubeta
lt -1,
um(t)*sin(t)*scaleumi+gb2mp1,um(t)*cos(t)*scaleumi+mubeta lt -1
#plot (0.1*cos(t))+gb2mp1,(0.1*sin(t))+mubeta lt -1
}

reset
unset multiplot
```

VIII. APPENDIX B – XOOPIC INPUT FILES

This appendix contains a sample of the FORTRAN code used to generate the input files, as well as a generated input file, for the trans-Alfvénic XOOPIC simulations described in Chapter V. The XOOPIC .inp files and the background magnetic field text files were programmatically generated simultaneously by a FORTRAN script. In this way, the background magnetic field could be tailored to the plasma parameters stipulated in the code shown below. Also included is the Gnuplot© script used to generate a plot of the ion kinetic beta from XOOPIC outputs of velocity and magnetic field.

Table 3 - Main FORTRAN program used to generate input files for XOOPIC

```
      program XOOPIC
      use XOOPIC_setup
      implicit none
      character(len=1)::new

      call setup

      open(3,file="input.inp")
      new=NEW_LINE('A')
      write(3,*) ' ',new,&
      'Variables',new,&
      '{'
      write(3,*)'pi=',pi
      write(3,*)'dr=',dr
      write(3,*)'Nport=',Nport
      write(3,*)'Rplasma',Rplasma
      write(3,*)'Rloop=',RL1
      write(3,*)'vte=',vte
      write(3,*)'Te=',Te !eV
      write(3,*)'vdez=',vdez
      write(3,*)'ne=',ne!desired maximum electron number
density
      write(3,*)'Bo=',Bo
      write(3,*)'vdiphi=',vdiphi
```

```
      write(3,*)'Ie=',Ie !Amperes
      write(3,*)'Ii=',Ii !Amperes
      write(3,*)'timestep=',timestep !keep dt*fpe < 0.01 ??
      write(3,*)'enp2c=',enp2c
      write(3,*)'Rplasma/dz = ',Rplasma/dz,new,&
      '}',new,&

      'Region',new,&
      '{',new,&
      '',new,&
      'Grid',new,&
      '{',new,&
      '     J =',NJ,new,&
      '     x1s = ',zmin,new,&
      '     x1f = ',zmax,new,&
      '     n1 = 1.0',new,&
      '     K =',NK,new,&
      '     x2s = ',rmin,new,&
      '     x2f =',rmax,new,&
      '     n2 = 1.0',new,&
      '     Geometry=0 //0->cylindrical 1->cartesian',new,&
      '}',new,&
      '',new,&
      'Control',new,&
      '{',new,&
      '     dt = ',timestep,new,&
      '     ElectrostaticFlag = 4 //4=multigrid electrostatic
field solve',new,&
      '     Bf = B_file.txt',new,&
      '}',new,&
      '',new,&
      'Species',new,&
      '{',new,&
      '     name = electrons',new,&
      '     m =',me,new,&
      '     q =',qe,new,&
      '}',new,&
      '',new,&
      'Species',new,&
      '{',new,&
      '         name = ions',new,&
      '         m =',mi,new,&
      '         q =',qi,new,&
      '}',new,&
      '',new,&
      'VarWeightBeamEmitter',new,&
      '{',new,&
      '     units = MKS',new,&
      '     j1 = 0',new,&
```

```
'     k1 = 0',new,&
'     j2 = 0',new,&
'     k2 =',Nport,new,&
'     speciesName = electrons',new,&
'     normal = 1',new,&
'     np2c =',enp2c,new,&
'     I=',Ie,new,&
'     //thetadot = 0.0',new,&
'     v1drift =',vdez,new,&
'     //v2drift = 0.',new,&
'     //v3drift = 0.',new,&
'     v1thermal =',vte,new,&
'     v2thermal =',vte,new,&
'     v3thermal =',vte,new,&
'}',new,&
'',new,&
'VarWeightBeamEmitter',new,&
'{',new,&
'     units = MKS',new,&
'     j1 = 0',new,&
'     k1 = 0',new,&
'     j2 = 0',new,&
'     k2 =',Nport,new,&
'     speciesName = ions',new,&
'     normal = 1',new,&
'     np2c =',inp2c,new,&
'     I =',Ii,new,&
'     //thetadot = 0.0',new,&
'     v1drift =',vdiz,new,&
'     //v2drift = 0.',new,&
'     //v3drift = 0.',new,&
'     v1thermal =',vti,new,&
'     v2thermal =',vti,new,&
'     v3thermal =',vti,new,&
'',new,&
'}',new,&
'',new,&
'Conductor',new,&
'{',new,&
'     name = Conductor1',new,&
'     j1 = 0',new,&
'     k1 = 0',new,&
'     j2 = 0',new,&
'     k2 =',NK,new,&
'     normal = 1',new,&
'}',new,&
'',new,&
'Conductor',new,&
'{',new,&
```

```
'     name = Conductor2',new,&
'     j1 = 0',new,&
'     k1 =',NK,new,&
'     j2 =',NJ,new,&
'     k2 =',NK,new,&
'     normal = -1',new,&
'}',new,&
'',new,&
'Conductor',new,&
'{',new,&
'     name = Conductor3',new,&
'     j1 =',NJ,new,&
'     k1 = 0',new,&
'     j2 =',NJ,new,&
'     k2 =',NK,new,&
'     normal = -1',new,&
'}',new,&
'',new,&
'CylindricalAxis',new,&
'{',new,&
'     j1 = 0',new,&
'     k1 = 0',new,&
'     j2 =',NJ,new,&
'     k2 = 0',new,&
'     normal = 1',new,&
'}',new,&
'',new,&
'Diagnostic',new,&
'{',new,&
'title = E2_45_25',new,&
'j1 = ',nint(((.45-zmin)/Lz)*NJ),new,&
'k1 = ',nint(((.25-rmin)/Lr)*NK),new,&
'j2 = ',nint(((.45-zmin)/Lz)*NJ),new,&
'k2 = ',nint(((.25-rmin)/Lr)*NK),new,&
'VarName = E2',new,&
'save = 1',new,&
'HistMax = 10000',new,&
'}',new,&
'',new,&
'Diagnostic',new,&
'{',new,&
'title = E2_45_10',new,&
'j1 = ',nint(((.45-zmin)/Lz)*NJ),new,&
'k1 = ',nint(((.10-rmin)/Lr)*NK),new,&
'j2 = ',nint(((.45-zmin)/Lz)*NJ),new,&
'k2 = ',nint(((.10-rmin)/Lr)*NK),new,&
'VarName = E2',new,&
'save = 1',new,&
'HistMax = 10000',new,&
```

```
      '}',new,&
      '',new,&
      'Diagnostic',new,&
      '{',new,&
      'title = E2_45_45',new,&
      'j1 = ',nint(((.45-zmin)/Lz)*NJ),new,&
      'k1 = ',nint(((.45-rmin)/Lr)*NK),new,&
      'j2 = ',nint(((.45-zmin)/Lz)*NJ),new,&
      'k2 = ',nint(((.45-rmin)/Lr)*NK),new,&
      'VarName = E2',new,&
      'save = 1',new,&
      'HistMax = 10000',new,&
      '}'
      end program
```

Table 4 - FORTRAN module used to calculate plasma parameters for XOOPIC input files.

```
      module XOOPIC_setup
      use XOOPIC_B_file
      implicit none
      double precision::me,mi,qe,qi,pi,eperm,c0
      real::Rplasma,beta,magnetization,f,vphibyvz,EizbyTe,vte,T
e,vdiz,vdez,ne,vdiphi
      real::Ie,IebyIi,Ii,timestep,Np,inp2c,enp2c,massratio,Lrby
Rplasma,RloopbyRplasma,vti
      integer::Nport
      contains
      subroutine setup

      massratio = 100.
      beta = 0.1
      magnetization = 0.1 !ratio of plasma radius to gyroradius
      f = 10. !cells per Debye length
      vphibyvz = 0.1
      EizbyTe = 45. !ratio of ion axial drift energy to
electron thermal energy
      NJ = 256
      NK = 128
      LrbyRplasma = 3.
      ZL1 = 0.0 !axial location of field-generating current
loop
      RloopbyRplasma = 1.5

      pi = acos(-1.)
      eperm = 8.85419e-12
      magperm = 4.*pi*1e-7
      c0 = sqrt(1./(eperm*magperm))

      Lz = 1.024; zmin = 0.; zmax = zmin+Lz
      dz = Lz/float(NJ)
      dr = dz; rmin = 0.
      Lr = dr*NK; rmax = rmin+Lr

      Nport = nint(NK/LrbyRplasma)
      Rplasma = Nport*dr
      RL1 = Rplasma*RloopbyRplasma !radius of field-generating
current loop

      qi = 1.60218e-19
      qe = qi*(-1.)
      me = 9.10938e-31
         mi = massratio*me !mi = 6.6e-26 !argon
```

```
      vte =
sqrt(2.*mi*f*beta/me)*(c0*vphibyvz*dz/(Rplasma*magnetization))
      !consequence of specifying beta, magnetization, grids per
Debye length & assuming ne=ni
      Te = (me/(-1.*qe))*vte**2 !eV
      vdiz = sqrt(Te*EizbyTe*qi/mi) !m/s
      vdez = vdiz
      ne = eperm*Te/(dr*dz*qi*f) !desired maximum electron
number density
      Bo = sqrt(ne*mi*magperm/beta)*vdiz
      vdiphi = qi*Bo*Rplasma/(mi*magnetization)

      call B_file

      !vti = sqrt(Ti*qi/mi)
      vti = 0.

      Ie = qe*ne*vdiz*pi*Rplasma*Rplasma !Amperes
      IebyIi = 1. !factor multiplying electron current to make
up for escaping electrons
      Ii = Ie*qi/(qe*IebyIi) !Amperes
      timestep = 0.01*2*pi*sqrt(me*eperm/(ne*qi*qi)) !keep
dt*fpe < 0.01 ??

      Np = 1e5 !target number of simulation particles
      inp2c = Ii*Lz/(qi*vdiz*Np)
      enp2c = inp2c

      end subroutine
      end module
```

Table 5 - FOTRAN module used to generate the background magnetic field file used by XOOPIC. This code also includes instructions to generate a file used to plot lines of constant enclosed magnetic flux.

```
      module XOOPIC_B_file
      use two_current_loop
      implicit none
      double precision::magperm
      real,allocatable::z_arr(:),r_arr(:),B_arr(:,:,:),Bzflux(:
,:),fluxradii(:),fluxfracs(:)
      real::dz,dr,zmin,zmax,rmin,rmax,Lz,Lr,refz,refr,refflux,p
i2,Bo
      integer::j2,k2,NJ,NK,refzindex,refrindex,l,m,nfracs
      contains
      subroutine B_file

      IL1=(2*Bo/magperm)*(((zmin-ZL1)**2+RL1**2)**1.5)/(RL1**2)
      print*,IL1,'loop current (A)'
      call mirror_parameters

      allocate(z_arr(NJ+1),r_arr(NK+1),B_arr(NJ+1,NK+1,3),Bzflu
x(NJ+1,NK+1))
      open(1,file='B_file.txt')

      z_arr=(/(j2,j2=0,NJ)/)*dz+zmin
      r_arr=(/(k2,k2=0,NK)/)*dr+rmin

      B_arr(:,:,1)=0.
      pi2=2.*acos(-1.)
      do j2=1,NJ+1
      do k2=1,NK+1
      x=(/0.,r_arr(k2),z_arr(j2)/)
      call fields(x,B_arr(j2,k2,:))
      B_arr(j2,k2,:)=B_arr(j2,k2,:)*1e4 !converting to Gauss
for XOOPIC input
      Bzflux(j2,k2)=pi2*dr*sum(B_arr(j2,1:k2,3)*r_arr(1:k2))
      write(1,*)
x(3),x(2),B_arr(j2,k2,3),B_arr(j2,k2,2),B_arr(j2,k2,1) !write
the B field values in the format required for XOOPIC
!     write(1,*)
x(3),x(2),B_arr(j2,k2,3),B_arr(j2,k2,2),B_arr(j2,k2,1),Bzflux(j
2,k2)
      end do
      end do
      close(1)

      refz=zmin
      refr=rmax*0.3
      !reference fluxes are for creating graph of enclosed flux
```

```
lines similar to that of C. Olsen

      refzindex=minloc(abs(z_arr(:)-refz),1)
!     print*,'refzindex=',refzindex
!     print*,'z_arr(refzindex)=',z_arr(refzindex)
      refrindex=minloc(abs(r_arr(:)-refr),1)
!     print*,'refrindex=',refrindex
!     print*,'r_arr(refrindex)=',r_arr(refrindex)

      refflux=Bzflux(refzindex,refrindex)
!     print*,'refflux=',refflux

      nfracs=5
      allocate(fluxfracs(nfracs),fluxradii(nfracs))
      fluxfracs=(/0.1,0.3,0.5,0.7,0.9/)
      fluxfracs=refflux*fluxfracs

      open(2,file='flux_lines.txt')
      do l=1,NJ+1
      do m=1,nfracs
      fluxradii(m)=r_arr(minloc(abs(Bzflux(l,:)-
fluxfracs(m)),1))
      end do
      write(2,*)z_arr(l),fluxradii(:)
      end do
      close(2)

      end subroutine
      end module
```

Table 6 - FORTRAN module used to calculate the two-dimensional magnetic field at an arbitrary, two-dimensional (z,r) location relative to the center of a loop of current. The current loop has a finite radius but the current path is infinitely narrow. This solution is based on the solutions to Griffith's Electrodynamics.[27] The code uses a numerical integration of the elliptic functions involved in calculating the off-axis field.

```
      module two_current_loop
      implicit none
      real,allocatable::sp(:)
      real::BZS,c1a,c2a,RL1,ZL1,IL1,RL2,ZL2,IL2,pi2on,B(3),x(3)
,c1b,c2b,c1c,c2c,Br,z1,z2,r
      double precision::sumr1,sumr2,sumz1,sumz2
      integer::i1,j1,n

      contains

      subroutine mirror_parameters
!     RL1=0.3
!     RL2=0.3
!     ZL1=1.6
!     ZL2=2.1
!     IL1=1589643.
!     IL2=191058.
!     IL=(2.*0.07*(0.7**2+RL**2)**1.5)/(3.14159*4*1e-7*RL**2)
      BZS=0.0
      n=10001
      pi2on=2*acos(-1.)/(n*1.)
      allocate(sp(n))
      do i1=1,n
      sp(i1)=sin(i1*pi2on)
      end do
      c1a=1e-7*IL1*RL1*pi2on
      c2a=1e-7*IL2*RL2*pi2on
      end subroutine

      subroutine fields(x,B)
      real,intent(in)::x(3)
      real,intent(out)::B(3)
      z1=x(3)-ZL1
      z2=x(3)-ZL2
!     r=sqrt(x(1)**2+x(2)**2)
      r=x(2)
      c1b=RL1**2+r**2+z1**2
      c2b=RL2**2+r**2+z2**2
      c1c=2*RL1*r
      c2c=2*RL2*r
      sumr1=sum(sp(:)/(sqrt(c1b-c1c*sp(:))**3))
      sumr2=sum(sp(:)/(sqrt(c2b-c2c*sp(:))**3))
      sumz1=sum((RL1-r*sp(:))/(sqrt(c1b-c1c*sp(:))**3))
```

```
      sumz2=sum((RL2-r*sp(:))/(sqrt(c2b-c2c*sp(:))**3))
!     Br=c0*z1*sum1
      Br=c1a*z1*sumr1+c2a*z2*sumr2
!     B(1)=(x(1)/r)*Br
!     B(2)=(x(2)/r)*Br
      B(2)=Br
      B(3)=BZS+c1a*sumz1+c2a*sumz2
!     B(3)=BZS+c0*(sum3+sum4)
      do j1=1,3
      if(ISNAN(B(j1))) B(j1)=0.
      end do
      end subroutine

      end module
```

Table 7 - Sample of a generated XOOPIC input file

```
Variables
{
 pi=   3.1415927410125732
 dr=  4.00000019E-03
 Nport=          43
 Rplasma  0.17200001
 Rloop=  0.25800002
 vte=   98597792.
 Te=   55272.852
 vdez=   66141408.
 ne=  1.90910308E+16
 Bo=  0.30919856
 vdiphi=  9.35380672E+08
 Ie=  -18802.730
 Ii=   18802.730
 timestep=  8.06069881E-12
 enp2c=  1.81692150E+10
 Rplasma/dz =    43.000000
}
Region
{

Grid
{
      J =         256
      x1s =    0.0000000
      x1f =    1.0240000
      n1 = 1.0
      K =         128
      x2s =    0.0000000
      x2f =  0.51200002
      n2 = 1.0
      Geometry=0 //0->cylindrical 1->cartesian
}

Control
{
      dt =   8.06069881E-12
      ElectrostaticFlag = 4 //4=multigrid electrostatic field
solve
      Bf = B_file.txt
}

Species
{
      name = electrons
```

```
      m =  9.10937968384415745E-031
      q = -1.60217995787982542E-019
}

Species
{
        name = ions
        m =  9.10937968384415745E-029
        q =  1.60217995787982542E-019
}

VarWeightBeamEmitter
{
      units = MKS
      j1 = 0
      k1 = 0
      j2 = 0
      k2 =          43
      speciesName = electrons
      normal = 1
      np2c =  1.81692150E+10
      I=  -18802.730
      //thetadot = 0.0
      v1drift =   66141408.
      //v2drift = 0.
      //v3drift = 0.
      v1thermal =   98597792.
      v2thermal =   98597792.
      v3thermal =   98597792.
}

VarWeightBeamEmitter
{
      units = MKS
      j1 = 0
      k1 = 0
      j2 = 0
      k2 =          43
      speciesName = ions
      normal = 1
      np2c =  1.81692150E+10
      I =   18802.730
      //thetadot = 0.0
      v1drift =   66141408.
      //v2drift = 0.
      //v3drift = 0.
      v1thermal =   0.0000000
      v2thermal =   0.0000000
      v3thermal =   0.0000000
```

```
}

Conductor
{
      name = Conductor1
      j1 = 0
      k1 = 0
      j2 = 0
      k2 =          128
      normal = 1
}

Conductor
{
      name = Conductor2
      j1 = 0
      k1 =          128
      j2 =          256
      k2 =          128
      normal = -1
}

Conductor
{
      name = Conductor3
      j1 =          256
      k1 = 0
      j2 =          256
      k2 =          128
      normal = -1
}

CylindricalAxis
{
      j1 = 0
      k1 = 0
      j2 =          256
      k2 = 0
      normal = 1
}

Diagnostic
{
title = E2_45_25
j1 =           112
k1 =            62
j2 =           112
k2 =            62
```

```
VarName = E2
save = 1
HistMax = 10000
}

Diagnostic
{
title = E2_45_10
j1 =          112
k1 =           25
j2 =          112
k2 =           25
VarName = E2
save = 1
HistMax = 10000
}

Diagnostic
{
title = E2_45_45
j1 =          112
k1 =          112
j2 =          112
k2 =          112
VarName = E2
save = 1
HistMax = 10000
}
```

Table 8 – Script used for generating the plot of β_{ki} shown in Figure 40. This script was loaded using Gnuplot© version 4.6.1 on a Linux operating system. The files "uzz.txt," "urr.txt," and "B.txt" are outputs produced from the XOOPIC interface, containing the ion velocities and the magnetic field. Note the use of the shell command 'paste' embedded in the some of the data file names.

```
reset

Nz=128; Nr=Nz/2; Lz=1.0; Lr=0.5
mi = 9.1e-29; mu0 = pi*4e-7
set dgrid3d Nz,Nr box (Lz/(real(Nz))),(Lr/(real(Nr)))
vnorm(a,b) = sqrt((a**2)+(b**2))
betak(n,v,B) = 2*mi*mu0*n*(v**2)/(B**2)
chkdef(a,b,c) = (stringcolumn(a))eq('i') &&
(stringcolumn(b))eq('i') && (stringcolumn(c))eq('i')
set xrange [0:Lz]; set yrange [0:Lr]; set view map; set size ratio
0.5

#set term wxt 0; set title 'vi (m/s)'
#splot '<paste uzz.txt urr.txt' using 1:3:(vnorm(($2),($4))) every
:::1 with pm3d notitle
set table 'vi_tbl.dat'; splot '<paste -d " " uzz.txt urr.txt'
using 1:3:(vnorm(($2),($4))) every :::1
set table 'B_tbl.dat'; splot 'B.txt' using 1:2:(vnorm(($3),($4)))
set table 'ni_tbl.dat'; splot 'ni.txt' using 1:2:3
unset table; unset dgrid3d

#set term wxt 1
#splot 'vi_tbl.dat' using
1:2:(((stringcolumn(4))eq('i'))?($3):(1/0)) with pm3d notitle


set pm3d; set logscale cb; set cbrange [0.1:100]
set cntrparam levels discrete 1.0; set contour surface
set term wxt 2; set title "Color Map of Ion Kinetic Beta - Black
Line showing Super Alfvenic Transition"; #set table 'Beta_tbl.dat'
set xlabel 'z axis (m)'; set ylabel 'radius (m)'; set cblabel "Ion
Kinetic Beta {/Symbol b}_k = {/Symbol m}_0n_im_iv_i^2/B^2" offset
1
splot '<paste -d " " ni_tbl.dat vi_tbl.dat B_tbl.dat' using
1:2:(chkdef(4,8,12)?(betak($3,$7,$11)):1/0) every :::1 with pm3d
lt -2 lw 2 title ''
unset table
```

IX. REFERENCES

[1] C. S. Olsen, "Experimental Characterization of Plasma Detachment from Magnetic Nozzles," Ph.D. Thesis, Rice University, 2013.

[2] C. A. Henderson, "Particle-in-Cell Model of Plasma Behavior in the Exhaust Region of VASIMR using OOPIC Pro," Undergraduate Thesis, University of Houston, 2010.

[3] J. P. Squire, et al., "VASIMR® VX-200 Operation at 200 kW and Plume Measurements: Future Plans and an ISS EP Test Platform," in the *32nd International Electric Propulsion Conference* (Wiesbaden, Germany, 2011), **IEPC-2011-154**.

[4] B. W. Longmier, et al., "VX-200 Magnetoplasma Thruster Performance Results Exceeding Fifty-Percent Thruster Efficiency," Journal of Propulsion and Power **27,** 915 (2011).

[5] C. S. Olsen, et al., "Investigation of Plasma Detachment from a Magnetic Nozzle in the Plume of the VX-200 Magnetoplasma Thruster," IEEE Transactions on Plasma Science **43,** 252 (2015).

[6] N. A. Krall, and P. C. Liewer, "Low-Frequency Instabilities in Magnetic Pulses," Physical Review A **4,** 2094 (1971).

[7] E. Choueiri, A. Kelly, and R. Jahn, "The Manifestation of Alfven's Hypothesis of Critical Ionization Velocity in the Performance of MPD Thrusters," in the *AIAA/DGLR/JSASS 18th International Electric Propulsion Conference* (Alexandria, VA, 1985).

[8] E. Y. Choueiri, "Electron-Ion Streaming Instabilities of an Electromagnetically Accelerated Plasma," Ph.D. Thesis, Princeton University, 1991.

[9] T. Hurtig, N. Brenning, and M. A. Raadu, "The Penetration of Plasma Clouds Across Magnetic Boundaries: The Role of High Frequency Oscillations," Physics of Plasmas **11,** L33 (2004).

[10] C. K. Birdsall, and A. B. Langdon, *Plasma Physics via Computer Simulation* (IOP Publishing, Bristol, 1991).

[11] F. F. Chen, *Introduction to Plasma Physics and Controlled Fusion* (Springer, 1984).

[12] E. A. Bering III, et al., "Observations of Single-Pass Ion Cyclotron Heating in a Trans-Sonic Flowing Plasma," Physics of Plasmas **17,** (2010).

[13] T. H. Stix, *Waves in Plasmas* (Springer-Verlag, New York, 1992).

[14] M. Giambusso, E. A. Bering, G. A. Edeen, M. D. Carter, C. S. Olsen, and J. P. Squire, "A Plan to Study the Radiated Emissions from a VASIMR Engine Exhaust Plume," in the *33rd International Electric Propulsion Conference* (Washington, D.C., 2013), **IEPC-2013-199**.

[15] NASA Technology Roadmaps, TA 2: In-Space Propulsion Technologies, National Aeronautics and Space Administration, July 2015, https://www.nasa.gov/sites/default/files/atoms/files/2015_nasa_technology_roadmaps_ta_2_in-space_propulsion_final.pdf.

[16] J. C. Adam, A. Heron, and G. Laval, "Study of Stationary Plasma Thrusters using Two-Dimensional Fully Kinetic Simulations," Physics of Plasmas **11,** 295 (2003).

[17] A. Heron, Adam, J.C., "Anomalous Conductivity in Hall Thrusters: Effects of the Non-Linear Coupling of the Electron-Cyclotron Drift Instability with Secondary Electron Emission of the Walls," Physics of Plasmas **20,** (2013).

[18] F. Taccogna, S. Longo, M. Capitelli, and R. Schneider, "Plasma Flow in a Hall Thruster," Physics of Plasmas **12,** 043502 (2005).

[19] F. Taccogna, P. Minelli, and N. Oudini, "Physics of Hall-Effect Discharge by Particle," in the *33rd International Electric Propulsion Conference* (Washington, D.C., 2013), **IEPC-2013-148**.

[20] M. Hirakawa, Arakawa, Y., "Numerical Simulation of Plasma Particle Behavior in a Hall Thruster," in the *32nd Joint Propulsion Conference and Exhibit* (Lake Buena Vista, FL, 1996).

[21] J. Szabo, N. Warner, M. Martinez-Sanchez, and O. Batishchev, "Full Particle-In-Cell Simulation Methodology for Axisymmetric Hall Effect Thrusters," Journal of Propulsion and Power **30,** 197 (2014).

[22] P. Coche, and L. Garrigues, "A Two-Dimensional (Azimuthal-Axial) Particle-in-Cell Model of a Hall Thruster," Physics of Plasmas **21,** (2014).

[23] F. H. Ebersohn, "Kinetic Method for Quasi-One-Dimensional Simulation of Magnetic Nozzle Plasmadynamics," Ph.D. Thesis, University of Michigan, 2016.

[24] K. F. Luskow, J. Duras, O. Kalentev, K. Matyash, J. Geiser, R. Schneiderk, and D. Tskhakaya, "Non-Equidistant Particle-In-Cell for Ion Thruster Plumes," in the *33rd International Electric Propulsion Conference* (Washington, D.C., 2013).

[25] J. P. Verboncoeur, A. B. Langdon, and N. Gladd, "An Object-Oriented Electromagnetic PIC Code," Computer Physics Communications **87,** 199 (1995).

[26] J. D. Jackson, *Classical Electrodynamics* (Wiley, Hoboken, 1999).

[27] D. J. Griffiths, *Introduction to Electrodynamics* (Prentice Hall, Upper Saddle River, 1999).

[28] M. Merino, and E. Ahedo, "Plasma Detachment in a Propulsive Magnetic Nozzle via Ion Demagnetization," Plasma Sources Science and Technology **23,** 032001 (2014).

[29] E. Ahedo, and M. Merino, "Two-Dimensional Supersonic Plasma Acceleration in a Magnetic Nozzle," Physics of Plasmas **17,** 073501 (2010).

[30] E. Ahedo, and M. Merino, "Two-Dimensional Plasma Acceleration in a Divergent Magnetic Nozzle," in the *45th AIAA/ASME/SAE/ASEE Joint Propulsion Conference & Exhibit* (Denver, Colorado, 2009), **AIAA 2009-5361**.